Table of contents

1. General considerations

If not stated otherwise, all reactions and manipulations were carried out under an atmosphere of dry nitrogen using Schlenk techniques or in an inert-atmosphere glovebox. *n*-Pentane, *n*-hexane, and THF were distilled from Na/benzophenone. CH_2Cl_2 as well as Me_3SiCl were distilled from CaH_2. *n*-Pentane, *n*-hexane, CH_2Cl_2, CD_2Cl_2, $CHCl_3$, and $CDCl_3$ were stored over molecular sieves (3 Å) at least overnight prior use.

The starting material $[Li(thf)]_2[1,1'\text{-fc}(BH_3)_2]$ was prepared according to a literature procedure (modification: $LiAlH_4$ was added in THF solution rather than Et_2O solution).[ES1] The following chemicals were purchased from commercial suppliers and used as received: $[Ph_3C][B(C_6F_5)_4]$ (ABCR), $B(C_6F_5)_3$ (ABCR), $LiAlH_4$ (1 M in dry THF; Sigma-Aldrich), $[n\text{Bu}_4N][BH_4]$ (Fluka), Et_3PO (Sigma-Aldrich), pyrazole (Acros Organics), 3,5-dimethylpyrazole (Sigma-Aldrich).

NMR spectra were recorded at 298 K using the following spectrometers: Bruker Avance-300 or Avance-500. Chemical shift values are referenced to (residual) solvent signals ($^1H/^{13}C\{^1H\}$; CD_2Cl_2: $\delta = 5.32/54.0$[ES2], $CDCl_3$: $\delta = 7.26/77.2$)[ES3] or external $BF_3{\cdot}OEt_2$ (^{11}B; $\delta = 0.00$). Abbreviations: s = singlet, d = doublet, t = triplet, vtr = virtual triplet, q = quartet, m = multiplet, b = broad, vb = very broad, n.r. = not resolved, n.o. = not observed. Resonances of carbon atoms attached to boron atoms were typically broadened and sometimes not observed due to the quadrupolar relaxation of boron. Resonance assignments were aided by ^1H-^1H-COSY, ^1H-^{13}C-HSQC, ^1H-^{13}C-HMBC, and ^1H-^1H-NOESY spectra.

Cyclic voltammetry (CV) measurements were performed in an inert-atmosphere glovebox at room temperature in a one-chamber, three-electrode cell using an *EG&G* Princeton Applied Research 263A potentiostat. A platinum disk electrode (2.00 mm diameter) was used as the working electrode with a platinum wire counter electrode and a silver wire reference electrode, which was coated with AgCl by immersion into HCl/HNO_3 (3:1). Prior to measurements, CH_2Cl_2 was dried over CaH_2 and degassed by three freeze-pump-thaw cycles. $[n\text{Bu}_4N][PF_6]$ (Sigma Aldrich; used as received) was employed as the supporting electrolyte (0.1 M). All potential values were referenced against the FcH/FcH^+ redox couple (FcH = ferrocene; $E_{1/2} = 0$ V). Scan rates were varied between 100 and 400 mV s^{-1}.

UV-vis absorption spectra were obtained using an *Agilent Technologies Cary* 60 UV-vis spectrometer at RT. The CH_2Cl_2 used was stored for one week over molecular sieves (3 Å) prior to measurement. The measured samples were filled in an inert-atmosphere glovebox into a sealable cuvette.

High-resolution mass spectra were measured in positive mode using a *Thermo Fisher Scientific* MALDI LTQ Orbitrap XL spectrometer and α-cyano-4-hydroxycinnamic acid as the matrix.

A spectrometer operated in constant acceleration mode in conjunction with a 512-channel analyzer (*WissEl GmbH*) was used to obtain ^{57}Fe Mössbauer spectra in transmission geometry. The source contained ^{57}Co diffused in Rh. The spectrometer was calibrated against α-iron at room temperature. The experiments were performed at 77 K in a continuous flow cryostat (*OptistatDN, Oxford Instruments*). For further analysis, spectroscopic data were transferred from the multi-channel analyzer to a PC. The spectra were analyzed employing the public domain program *Vinda*[ES4] running on an *Excel 2003®* platform. The Mössbauer parameters isomer shift δ, quadrupole splitting ΔE_Q and the line width at half maximum Γ were determined by least-squares fits using Lorentzian line shapes.

2. Synthetic details

Synthesis of compound 1

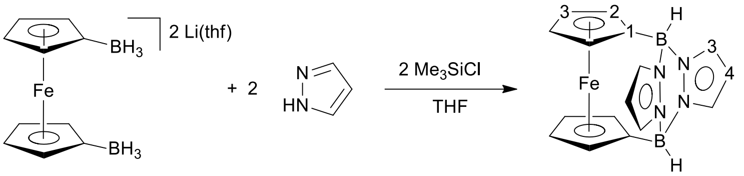

1

Note: For practical reasons, the actually employed stoichiometries deviate from the ideal stoichiometries.

[Li(thf)]$_2$[1,1'-fc(BH$_3$)$_2$] (2.0 g, 5.4 mmol, 1 eq) and pyrazole (1.8 g, 26 mmol, 5 eq) were mixed in THF (40 mL) and the resulting yellow emulsion was cooled to −78 °C. Me$_3$SiCl (2.2 mL, 1.9 g, 17 mmol, 3 eq) was diluted with THF (20 mL) and added with stirring through a dropping funnel. The reaction mixture was stirred for 30 min while still remaining in the dry-ice bath. It was then allowed to warm to room temperature and subsequently heated to 70 °C for 6 h. After removal of all volatiles under reduced pressure, the crude product was purified by short-column chromatography on silica gel (*c*-hexane:ethyl acetate, 20:1, $R_F = 0.4$) and washed with *n*-hexane (3 × 30 mL) to furnish **1** as a yellow powder. Yield: 0.71 g (39%). Single crystals of **1** suitable for X-ray analysis were grown by slow evaporation of a CH$_2$Cl$_2$ solution.

Note: The product **1** is poorly soluble (approx. 10 mg/mL in CH$_2$Cl$_2$); product that precipitates on the column can only be re-dissolved in CH$_2$Cl$_2$.

^{1}H NMR (500.2 MHz, CD$_2$Cl$_2$) δ 7.81 (d, $^3J = 2.3$ Hz, 4H; pzH-3), 6.49 (t, $^3J = 2.3$ Hz, 2H; pzH-4), 3.99* (n.r., 4H; CpH-3), 3.27* (n.r., 4H; CpH-2).

^{1}H{^{11}B} NMR (500.2 MHz, CD$_2$Cl$_2$) δ 7.81 (d, $^3J = 2.3$ Hz, 4H; pzH-3), 6.49 (n.r., 2H; pzH-4), 4.37 (s, 2H; BH), 3.99 (n.r., 4H; CpH-3), 3.27 (n.r., 4H; CpH-2).

^{11}B NMR (160.5 MHz, CD$_2$Cl$_2$) δ –3.9 (d, $^1J = 99$ Hz).

^{11}B{^{1}H} NMR (160.5 MHz, CD$_2$Cl$_2$) δ –3.9 (s).

^{13}C{^{1}H} NMR (125.8 MHz, CD$_2$Cl$_2$) δ 136.3 (pzC-3), 106.0 (pzC-4), 83** (CpC-1), 70.9 (CpC-2), 70.1 (CpC-3).

*This assignment is based on a cross-peak between the two signals at 7.81/3.27 ppm in the ^{1}H-^{1}H-NOESY experiment.

**This resonance was detected through a cross-peak in the ^{1}H-^{13}C-HMBC NMR experiment.

HRMS: Calculated m/z for [C$_{16}$H$_{16}$B$_2$N$_4$Fe]$^+$: 342.09050, found 342.09055.

Cyclic voltammetry (CH$_2$Cl$_2$, [*n*Bu$_4$N][PF$_6$] 0.1 M, 200 mV s^{-1}, vs. FcH/FcH$^+$): $E_{1/2} = -0.23$ V.

Synthesis of 1Me

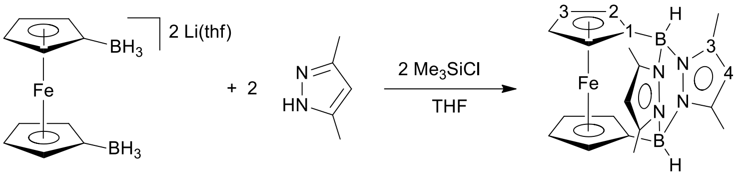

1Me

[Li(thf)]$_2$[1,1'-fc(BH$_3$)$_2$] (0.38 g, 1.0 mmol, 1 eq) and 3,5-dimethylpyrazole (0.21 g, 2.2 mmol, 2 eq) were dissolved in THF (15 mL) and stirred overnight. Me$_3$SiCl (0.26 mL, 0.22 g, 2.0 mmol, 2 eq) in THF (6 mL) was added with stirring at room temperature through a dropping funnel. After complete addition, the reaction mixture was heated to 70 °C for 3 h. After removal of all volatiles under reduced pressure, the crude product was purified by column chromatography on silica gel (*c*-hexane:ethyl acetate, 20:1, $R_F = 0.3$) to furnish **1Me** as a yellow microcrystalline solid. Yield: 0.22 g (55%).
Single crystals of **1Me** suitable for X-ray analysis were grown by slow evaporation of a CH$_2$Cl$_2$ solution.

^{1}H NMR (500.2 MHz, CDCl$_3$) δ 6.02 (s, 2H; pzH-4), 4.02* (n.r., 4H; CpH-3), 3.33* (n.r., 4H; CpH-2), 2.44 (s, 12H; pzCH$_3$).
^{1}H{^{11}B} NMR (500.2 MHz, CDCl$_3$) δ 6.02 (s, 2H; pzH-4), 4.42 (s, 2H; BH), 4.02 (n.r., 4H; CpH-3), 3.33 (n.r., 4H; CpH-2), 2.44 (s, 12H; pzCH$_3$).
^{11}B NMR (160.5 MHz, CDCl$_3$) δ –7.6 (n.r., $h_{1/2} \approx 270$ Hz)
^{11}B{^{1}H} NMR (160.5 MHz, CDCl$_3$) δ –7.6 (s, $h_{1/2} \approx 180$ Hz)
^{13}C{^{1}H} NMR (125.8 MHz, CDCl$_3$) δ 144.6 (pzC-3), 106.1 (pzC-4), 80.6 (b; CpC-1), 70.1 (CpC-2), 69.5 (CpC-3), 12.2 (pzCH$_3$).
*This assignment is based on a cross-peak between the two signals at 3.33/2.44 ppm in the ^{1}H-^{1}H-NOESY experiment.
HRMS: Calculated *m/z* for [C$_{20}$H$_{24}$B$_2$N$_4$Fe]$^+$: 398.15310, found: 398.15344.
Cyclic voltammetry (CH$_2$Cl$_2$, [*n*Bu$_4$N][PF$_6$] 0.1 M, 200 mV s^{-1}, vs. FcH/FcH$^+$): $E_{1/2}$ = –0.32 V.

Synthesis of [2][B(C_6F_5)$_4$]

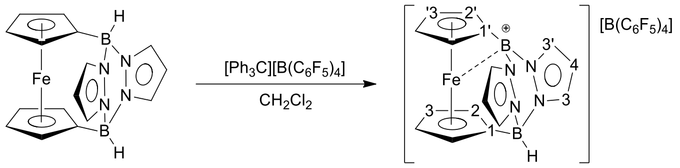

1 [2][B(C_6F_5)$_4$]

The reaction was performed in a glovebox. A snap-cap vial was charged with [Ph_3C][B(C_6F_5)$_4$] (0.27 g, 0.29 mmol, 1 eq) and CH_2Cl_2 (2 mL). The solution was added dropwise with swirling at room temperature to a second snap-cap vial containing a solution of **1** (0.10 g, 0.29 mmol, 1 eq) in CH_2Cl_2 (4 mL). The vial in which the solution of [Ph_3C][B(C_6F_5)$_4$] had been prepared was rinsed with CH_2Cl_2 (2 × 2 mL) and the rinsing liquid was added to the reaction mixture to ensure quantitative transfer of the hydride-abstracting reagent (see note below). After the color of the reaction mixture had changed from yellow-green (blended color of the trityl cation and **1**) to dark orange-brown, *n*-pentane (6 mL) was added until a beige-brown precipitate formed. The supernatant was decanted and the precipitate washed with *n*-pentane (2 × 1 mL). To remove final impurities, the solid was dissolved in $CHCl_3$ (5 mL), filtered over glass wool, and precipitated again with *n*-pentane (approx. 4 mL). Compound [**2**][B(C_6F_5)$_4$] was obtained as an orange-brown microcrystalline solid. Yield: 0.21 g (72%).

Orange-colored single crystals suitable for X-ray analysis were grown by layering a concentrated solution of [**2**][B(C_6F_5)$_4$] in CH_2Cl_2 with *n*-hexane.

Note: If less than 1 eq of [Ph_3C][B(C_6F_5)$_4$] is used, the NMR signals of the crude product are severely broadened due to dynamic hydride transfer between **1** and [**2**][B(C_6F_5)$_4$] (cf. Figures S36-S39).

^{1}H NMR (500.2 MHz, CD_2Cl_2) δ 8.29* (d, ^3J = 2.3 Hz, 2H; pzH-3), 8.13* (d, ^3J = 2.6 Hz, 2H; pzH-3'), 6.68 (vtr, 2H; pzH-4), 5.49* (vtr, 2H; CpH-3'), 4.83^a (vtr, 2H; CpH-3), 4.16* (vtr; 2H; CpH-2'), 3.23^a (vtr, 2H; CpH-2).

^{1}H{^{11}B} NMR (500.2 MHz, CD_2Cl_2) δ 8.29 (d, ^3J = 2.3 Hz, 2H; pzH-3), 8.13 (d, ^3J = 2.6 Hz, 2H; pzH-3'), 6.68 (vtr, 2H; pzH-4), 5.49 (vtr, 2H; CpH-3'), 4.83 (vtr, 2H; CpH-3), 4.36 (s, 1H; BH), 4.16 (vtr, 2H; CpH-2'), 3.23 (vtr, 2H; CpH-2).

^{11}B NMR (160.5 MHz, CD_2Cl_2) δ 23.5 (s; B^+), –5.2 (d, ^1J = 115 Hz; BH), –16.8 (s; B(C_6F_5)$_4$).

^{11}B{^{1}H} NMR (160.5 MHz, CD_2Cl_2) δ 23.5 (s; B^+), –5.2 (s; BH), –16.8 (s; B(C_6F_5)$_4$).

^{13}C{^{1}H} NMR (125.8 MHz, CD_2Cl_2) δ 148.7 (dm, $^1J_{CF}$ = 245 Hz; *o*-CF), 140.4 (pzC-3), 138.8 (dm, $^1J_{CF}$ = 245 Hz; *p*-CF), 136.8 (dm, $^1J_{CF}$ = 250 Hz; *m*-CF) 136.2 (pzC-3'), 109.6 (pzC-4), 104** (CpC-1), 85.8 (CpC-3'), 80.3 (CpC-2'), 79.5^a (CpC-3), 75.5^a (CpC-2), n.o. (CpC-1').

^{19}F NMR (470.6 MHz, CD_2Cl_2) δ –133.1 (m; *o*-CF), –163.6 (m; *p*-CF), –167.5 (m; *m*-CF).

*This assignment is based on a cross-peak between the two signals at 8.13/4.16 ppm in the ^{1}H-^{1}H-NOESY experiment (distance between pzH-3'and CpH-2' is shorter than between pzH-3 and CpH-2).

** This resonance was detected through a cross-peak in the ^{1}H-^{13}C-HMBC NMR experiment.

^{a} CpH/C-2 and CpH/C-3 could not be assigned through 2D NMR experiments and have thus been assigned by analogy to CpH/C-2' and CpH/C-3' and to the corresponding signals of [**2Me**][B(C_6F_5)$_4$].

Note: The resonances of the [B(C_6F_5)$_4$]$^-$ anion are in agreement with literature values.[ES5]

HRMS: Calculated *m/z* for [$C_{16}H_{15}B_2N_4Fe$]$^+$: 341.08268, found 341.08297.

Synthesis of [**2Me**][B(C_6F_5)$_4$]

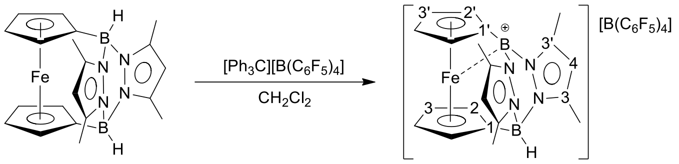

1Me

[2Me][B(C_6F_5)$_4$]

The reaction was performed in a glovebox. A snap-cap vial was charged with [Ph_3C][B(C_6F_5)$_4$] (92 mg, 0.10 mmol, 1 eq) and CH_2Cl_2 (4 mL). The solution was added dropwise with swirling at room temperature to a second snap-cap vial containing a solution of **1Me** (40 mg, 0.10 mmol, 1 eq) in CH_2Cl_2 (1 mL). The vial in which the solution of [Ph_3C][B(C_6F_5)$_4$] had been prepared was rinsed with CH_2Cl_2 (3 × 1 mL) and the rinsing liquid was added to the reaction mixture to ensure quantitative transfer of the hydride-abstracting reagent. After the color of the reaction mixture had changed from green to dark orange-brown, *n*-pentane (6 mL) was added until a yellow precipitate formed. The supernatant was decanted, the precipitate washed with *n*-pentane (2 × 1 mL) and dried under vacuum. Compound [**2Me**][B(C_6F_5)$_4$] was obtained as a yellow microcrystalline solid. Yield: 83 mg (77%).
Yellow crystals suitable for X-ray analysis were grown by layering a concentrated solution of [**2Me**][B(C_6F_5)$_4$] in CH_2Cl_2 with *n*-hexane.

^{1}H NMR (500.2 MHz, CD_2Cl_2) δ 6.18 (s, 2H; pzH-4), 5.42 (vtr, 2H; CpH-3'), 4.80 (vtr, 2H; CpH-3), 4.11* (vtr, 2H; CpH-2'), 3.31* (vtr, 2H; CpH-2), 2.56* (s, 6H; pzCH_3-3'), 2.48* (s, 6H; pzCH_3-3).
^{1}H{^{11}B} NMR (500.2 MHz, CD_2Cl_2) δ 6.18 (s, 2H; pzH-4), 5.41 (vtr, 2H; CpH-3'), 4.80 (vtr, 2H; CpH-3), 4.26 (s, 1H; BH), 4.11 (vtr, 2H; CpH-2'), 3.30 (vtr, 2H; CpH-2), 2.56 (s, 6H; pzCH_3-3'), 2.48 (s, 6H; pzCH_3-3).
^{11}B NMR (160.5 MHz, CD_2Cl_2) δ 23.4 (s; B^+), –9.0 (d, J = 100 Hz; BH), –16.7 (s; B(C_6F_5)$_4$).
^{11}B{^{1}H} NMR (160.5 MHz, CD_2Cl_2) δ 23.4 (s; B^+), –9.0 (s; BH), –16.7 (s; B(C_6F_5)$_4$).
^{13}C{^{1}H} NMR (125.8 MHz, CD_2Cl_2) δ 151.3 (pzC-3 or 3'), 148.7 (dm, $^{1}J_{CF}$ =245 Hz; *o*-CF), 147.1 (pzC-3 or 3'), 138.8 (dm, $^{1}J_{CF}$ = 245 Hz, *p*-CF), 136.8 (dm, $^{1}J_{CF}$ = 250 Hz, *m*-CF), 109.4 (pzC-4), 100** (CpC-1) 85.0 (CpC-3'), 79.4 (CpC-3), 79.4 (CpC-2'), 75.1 (CpC-2), 13.2 (pzCH_3-3'), 12.6 (pzCH_3-3), n.o. (CpC-1').
*This assignment is based on cross-peaks between the signals at 3.31/2.48 ppm and 4.11/2.56 ppm (much higher intensity => shorter distance => CpH-2'/pzCH_3-3') in the ^{1}H-^{1}H-NOESY experiment.
**This resonance was detected through a cross-peak in the ^{1}H-^{13}C-HMBC NMR experiment.
Note: The resonances of the [B(C_6F_5)$_4$]$^-$ anion are in agreement with literature values.[ES5]
HRMS: Calculated *m/z* for [$C_{20}H_{23}B_2N_4Fe$]$^+$: 397.14528, found 397.14574.

Synthesis of [2·py][B(C_6F_5)$_4$])

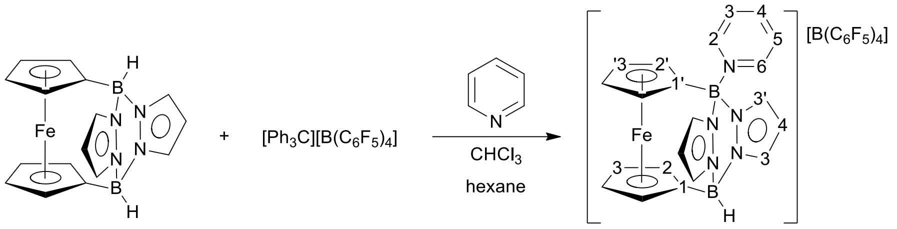

1

[**2**py][B(C_6F_5)$_4$]

The reaction was performed in a glovebox. A snap-cap vial was charged with **1** (20 mg, 0.058 mmol, 1eq), [Ph$_3$C][B(C_6F_5)$_4$] (54 mg, 0.059 mmol, 1 eq), and CHCl$_3$ (4 mL). After the color of the mixture had changed to deep brown, pyridine (0.1 M in *n*-hexane, 0.6 mL, 0.06 mmol, 1 eq) was added dropwise with swirling at room temperature. A pale yellow precipitate formed, which was isolated by filtration, washed with CHCl$_3$ and *n*-hexane, and dried under reduced pressure ([**2**·py][B(C_6F_5)$_4$]). Yield: 21 mg (33%).

^{1}H NMR (500.2 MHz, CD$_2$Cl$_2$) δ 9.09* (d, ^3J = 5.9 Hz, 1H; pyH-2), 8.56 (vtrvtr, 1H; pyH-4), 8.30* (d, ^3J = 6.0 Hz, 1H; pyH-6), 8.13* (d, ^3J = 2.4, 2H; pzH-3), 8.03 (vtr, 1H; pyH-3), 7.93 (vtr, 1H; pyH-5), 7.12* (d, ^3J = 2.6 Hz, 2H; pzH-3'), 6.68 (vtr, 2H; pzH-4), 4.36 (vtr, 2H; CpH-3'), 4.15 (vtr, 2H; CpH-3), 3.53* (vtr, 2H; CpH-2'), 3.34* (vtr, 2H; CpH-2).
^{1}H{^{11}B} NMR (500.2 MHz, CD$_2$Cl$_2$) δ 9.09 (d, ^3J = 5.9 Hz, 1H; pyH-2), 8.56 (vtr, 1H; pyH-4), 8.30 (d, ^3J = 6.0 Hz, 1H; pyH-6), 8.13 (d, ^3J = 2.3 Hz, 2H; pzH-3), 8.03 (vtr, 1H; pyH-3), 7.93 (vtr, 1H; pyH-5), 7.12 (d, ^3J = 2.5 Hz, 2H; pzH-3'), 6.68 (vtr, 2H; pzH-4), 4.54 (s, 1H; BH), 4.36 (n.r., 2H; CpH-3'), 4.15 (n.r., 2H; CpH-3), 3.53 (n.r., 2H; CpH-2'), 3.34 (n.r., 2H; CpH-2).
^{11}B NMR (160.5 MHz, CD$_2$Cl$_2$) δ 5.3 (s; B$^+$-py), –3.7 (n.r., $h_{1/2} \approx$ 240 Hz; B-H), –16.7 (s; B(C_6F_5)$_4$).
^{11}B{^{1}H} NMR (160.5 MHz, CD$_2$Cl$_2$) δ 5.3 (s; B$^+$-py), –3.7 (s, $h_{1/2} \approx$ 140 Hz; B-H), –16.7 (s; B(C_6F_5)$_4$).
^{13}C NMR (125.8 MHz, CD$_2$Cl$_2$) δ 149.4 (pyC-2), 148.7 (dm, $^1J_{CF}$ = 250 Hz, *o*-CF), 147.8 (pyC-4), 145.5 (pyC-6), 139.0 (pzC-3), 138.9 (dm, $^1J_{CF}$ = 250 Hz, *p*-CF), 136.9 (dm, $^1J_{CF}$ = 245 Hz, *m*-CF), 134.9 (pzC-3'), 128.7 (pyC-3), 128.6 (pyC-5), 109.0 (pzC-4), 73.5 (CpC-3'), 72.9 (CpC-2'), 71.7 (CpC-3), 71.6 (CpC-2), n.o. (CpC-1,1').
^{19}F NMR (470.6 MHz, CD$_2$Cl$_2$) δ –133.0 (m, *o*-CF; C_6F_5), –163.4 (m, *p*-CF; C_6F_5), –167.3 (m, *m*-CF; C_6F_5).
*This assignment is based on cross-peaks between the signals at 9.09/7.12, 9.09/3.53, 8.30/7.12, 8.13/3.34, and 7.12/3.53 ppm in the ^{1}H-^{1}H-NOESY experiment.
Note: The resonances of the [B(C_6F_5)$_4$]$^-$ anion are in agreement with literature values.[ES5]
HRMS: Calculated *m/z* for [$C_{21}H_{20}B_2N_5Fe$]$^+$: 420.12488, found 420.12476

Investigation of the dynamic hydride-transfer equilibrium between 1/[2][B(C_6F_5)$_4$] or 1Me/[2Me][B(C_6F_5)$_4$]

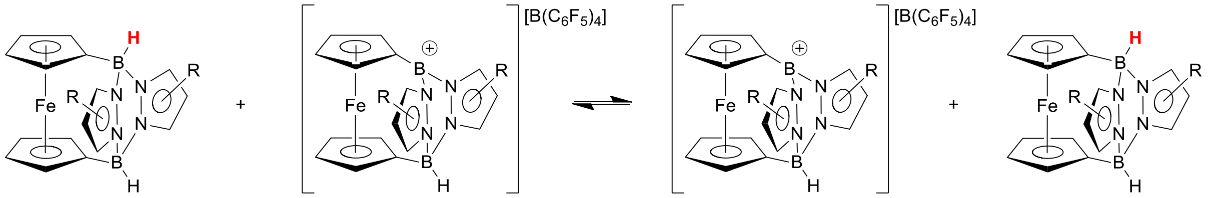

1 or **1Me**

[**2**][B(C_6F_5)$_4$] or [**2Me**][B(C_6F_5)$_4$]

[**2**][B(C_6F_5)$_4$] or [**2Me**][B(C_6F_5)$_4$]

1 or **1Me**

The NMR samples were prepared in a glove box at room temperature in three different ways:

a) An NMR tube was charged with **1** (5.0 mg, 0.014 mmol, 1 eq), [Ph_3C][B(C_6F_5)$_4$] (11 mg, 0.012, 0.8 eq), and CD_2Cl_2 (0.5 mL).

b) An NMR tube was charged with **1** (10 mg, 0.029 mmol, 1 eq) and CD_2Cl_2 (0.5 mL). After NMR measurement, [Ph_3C][B(C_6F_5)$_4$] (24 mg, 0.026, 0.9 eq) was added to the NMR tube. The sample was measured again and subsequently, [*n*Bu_4N][BH_4] (7.0 mg, 0.027 mmol, 1.0 eq of [BH_4]$^-$) was added to the NMR tube and the sample was measured a third time.

c) An NMR tube was charged with [**2**][B(C_6F_5)$_4$] (10 mg, 0.0098 mmol, 1 eq) or [**2Me**][B(C_6F_5)$_4$] (10 mg, 0.0093 mmol, 1 eq) and CD_2Cl_2 (0.5 mL). After NMR measurement, equimolar amounts of **1** (3.0 mg, 0.0087 mmol, 1 eq) or **1Me** (4.0 mg, 0.010 mmol, 1 eq) were added to the respective NMR tube and the samples were measured again.

Determination of the Lewis acidity of [2][$B(C_6F_5)_4$] by applying the Gutmann-Beckett method

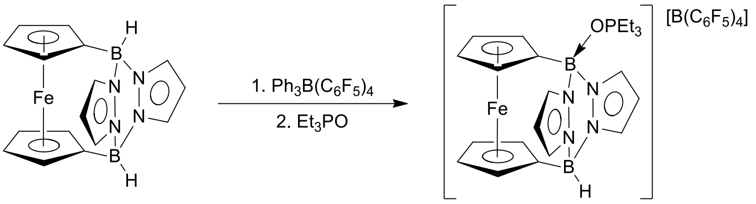

1

[**2**$OPEt_3$][$B(C_6F_5)_4$]

The NMR samples were prepared in a glove box at room temperature in three different ways:

a) Use of less than stoichiometric amounts of Et_3PO in order to ensure quantitative complexation of the base.

An NMR tube was charged with **1** (5.0 mg, 0.015 mmol, 1.0 eq), [Ph_3C][$B(C_6F_5)_4$] (12 mg, 0.013 mmol, 0.9 eq), and CD_2Cl_2 (0.5 mL). Neat Et_3PO (1.0 mg, 0.007 mmol, 0.5 eq) was added to the brown solution after the consumption of **1** and the occurrence of severely broadened signals had been confirmed by ^1H NMR spectroscopy.

b) Use of equimolar amounts of Et_3PO.

In an NMR tube, [**2**][$B(C_6F_5)_4$] (11 mg, 0.011 mmol, 1.0 eq) was dissolved in CD_2Cl_2 (0.5 mL) and a calibrated solution of Et_3PO (0.1 mL, 0.11 M in CH_2Cl_2, 0.011 mmol 1.0 eq) was added.

c) Use of excess Et_3PO in order to ensure quantitative complexation of the borenium cation.

In an NMR tube, a solid mixture of [**2**][$B(C_6F_5)_4$] (10 mg, 0.0098 mmol, 1.0 eq) and Et_3PO (2.0 mg, 0.015 mmol, 1.5 eq) was dissolved in CD_2Cl_2 (0.5 mL).

In all cases, the same chemical shift value of $\delta(^{31}P) = 91.0$ ppm was recorded for the coordinated Et_3PO.

Acceptor Number (AN) = 2.21 ($\delta(^{31}$P; B–O adduct) – $\delta(^{31}$P; Et_3PO in *n*-hexane) = 2.21 (91.0 – 41.0) = **111 (CD_2Cl_2)**.[ES6]

Assessment of the Lewis acidity of [**2**][$B(C_6F_5)_4$] relative to that of $B(C_6F_5)_3$ by competition experiments

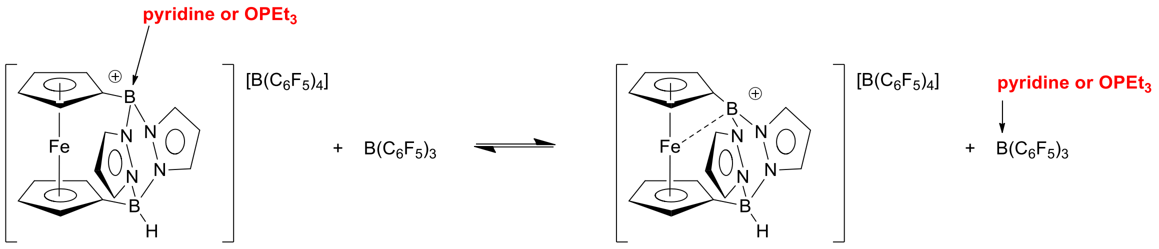

[**2**py][$B(C_6F_5)_4$] or
[**2**$OPEt_3$][$B(C_6F_5)_4$]

[**2**][$B(C_6F_5)_4$]

Note: Since the ferrocene-containing compounds are not long-term stable against $B(C_6F_5)_3$, some decomposition was observed in all cases. Thus, no quantitative values of equilibrium constants could be determined.

The experiments were performed in two different ways: (i) The pyridine or Et_3PO adduct of [**2**][$B(C_6F_5)_4$] was prepared and subsequently treated with free $B(C_6F_5)_3$. (ii) The pyridine or Et_3PO adduct of $B(C_6F_5)_3$ was prepared and subsequently treated with free [**2**][$B(C_6F_5)_4$]. The transfer of pyridine or Et_3PO between both Lewis acids occurred in all experiments. However, the transfer of pyridine/Et_3PO *from* $B(C_6F_5)_3$ *to* [**2**][$B(C_6F_5)_4$] was much faster and took place to a higher degree, which qualitatively indicates that [**2**][$B(C_6F_5)_4$] is the stronger Lewis acid.

a) Treatment of [**2**·py][$B(C_6F_5)_4$] with $B(C_6F_5)_3$

In an NMR tube, [**2**·py][$B(C_6F_5)_4$] (10 mg, 0.0091 mmol, 1.0 eq) was dissolved in CD_2Cl_2 (0.5 ml). A ^1H NMR spectrum was recorded. Then $B(C_6F_5)_3$ (5.0 mg, 0.0098 mmol, 1.1 eq) was added. ^1H NMR spectra were recorded after 30 min, 1d, and 3d.

b) Treatment of $B(C_6F_5)_3$·py with [**2**][$B(C_6F_5)_4$]

In an NMR tube, $B(C_6F_5)_3$ (5.0 mg, 0.0098 mmol, 1.0 eq) was dissolved in $CDCl_3$ (0.5 mL) and pyridine (0.1 mL, 0.1 M in *n*-hexane, 0.01 mmol, 1.0 eq) was added. ^1H and ^{11}B NMR spectra were recorded. After all volatiles had been removed under reduced pressure, CD_2Cl_2 (0.5 mL) and [**2**][$B(C_6F_5)_4$] (10 mg, 0.0098 mmol, 1.0 eq) were added, and ^1H and ^{11}B NMR spectra were recorded again.

c) Treatment of [**2**·$OPEt_3$][$B(C_6F_5)_4$] with $B(C_6F_5)_3$

In an NMR tube, [**2**][$B(C_6F_5)_4$] (11 mg, 0.011 mmol, 1.0 eq) was dissolved in CD_2Cl_2 (0.5 mL) and Et_3PO (0.1 mL, 0.11 M in CH_2Cl_2, 0.011 mmol, 1.0 eq) was added. ^1H, ^{11}B, and $^{31}P\{^1H\}$ NMR spectra were recorded. Then, a solution of $B(C_6F_5)_3$ (0.05 mL, 0.22 M in CH_2Cl_2, 0.011 mmol, 1.0 eq) was added via syringe.

d) Treatment of $B(C_6F_5)_3$·$OPEt_3$ with [**2**][$B(C_6F_5)_4$]

In an NMR tube, $B(C_6F_5)_3$ (5.0 mg, 0.0098 mmol, 1.0 eq) was dissolved in $CDCl_3$ (0.5 mL) and Et_3PO (1.3 mg, 0.0097 mmol, 1.0 eq) was added. ^1H, ^{11}B, and ^{19}F NMR spectra were recorded. Then [**2**][$B(C_6F_5)_4$] (10 mg, 0.0098 mmol, 1.0 eq) was added. ^1H, ^{11}B and ^{19}F NMR spectra were recorded after 30 min and 16 h.

3. Plots of ^{1}H, ^{13}C{^{1}H} and ^{11}B NMR spectra

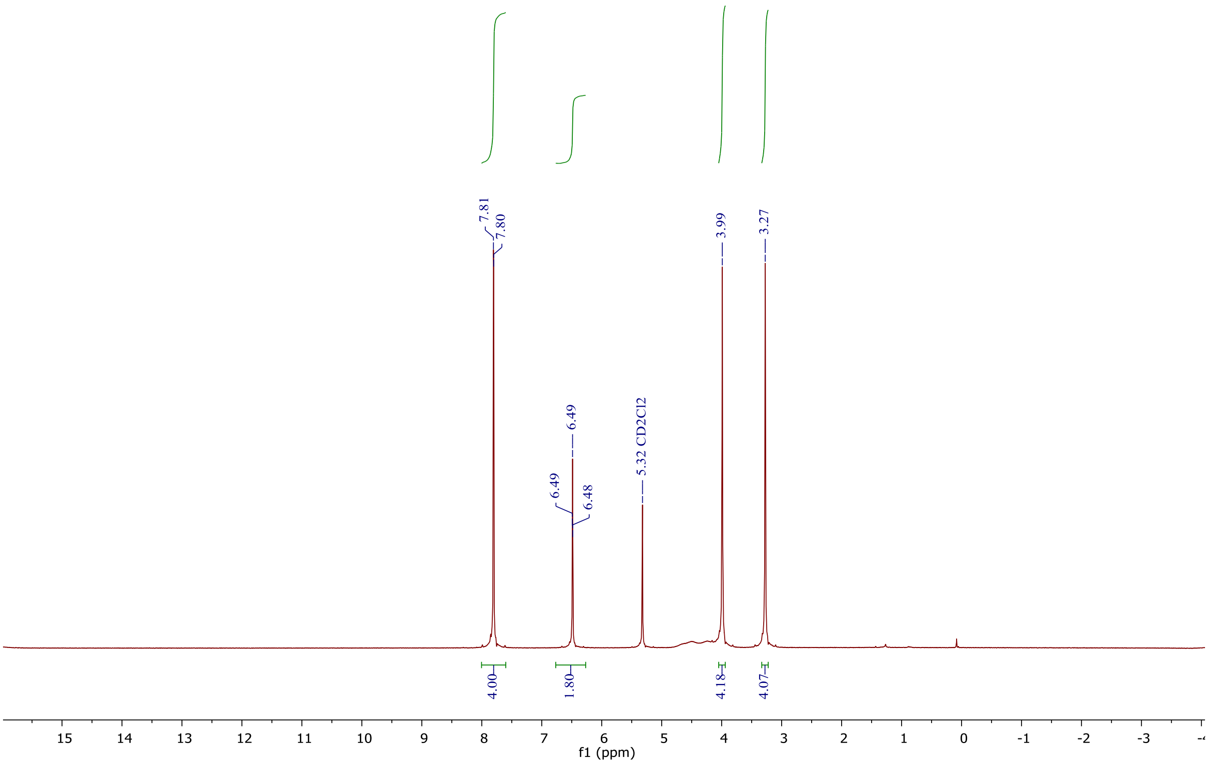

Figure S1: ^{1}H NMR spectrum of **1** (CD_2Cl_2, 500.2 MHz).

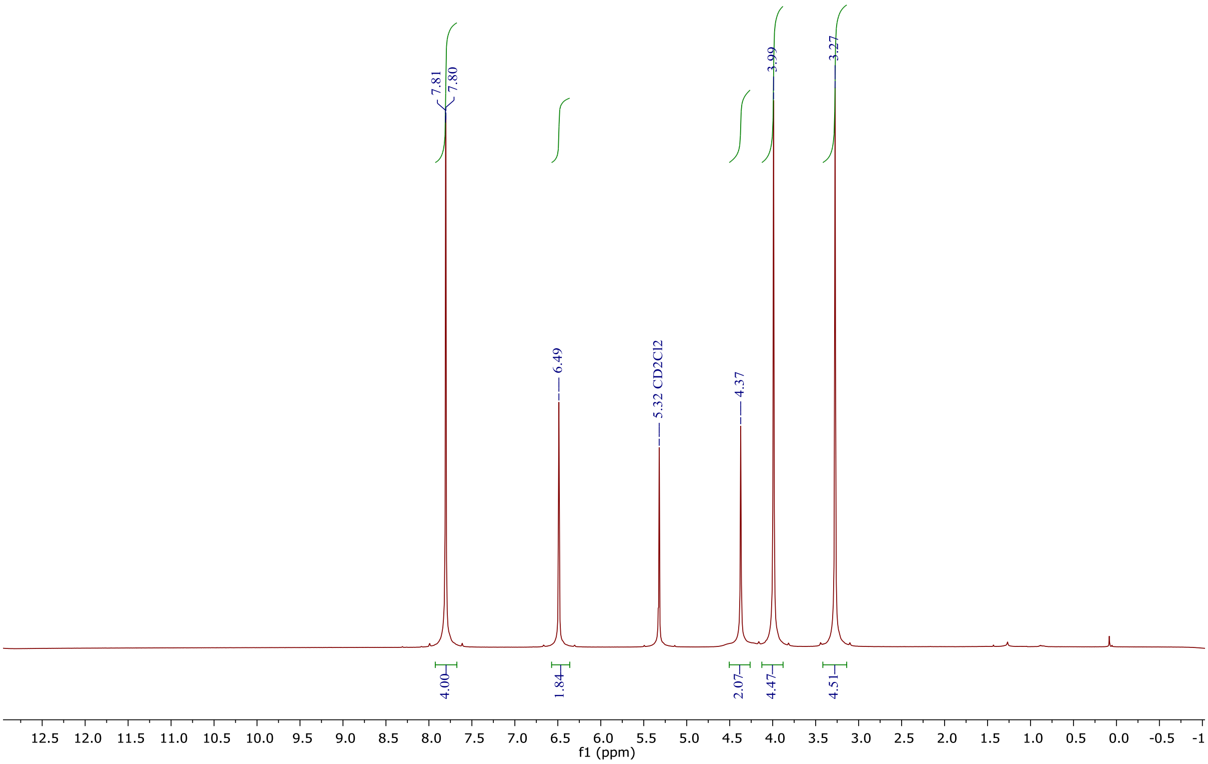

Figure S2: ^{1}H{^{11}B} NMR spectrum of **1** (CD_2Cl_2, 500.2 MHz).

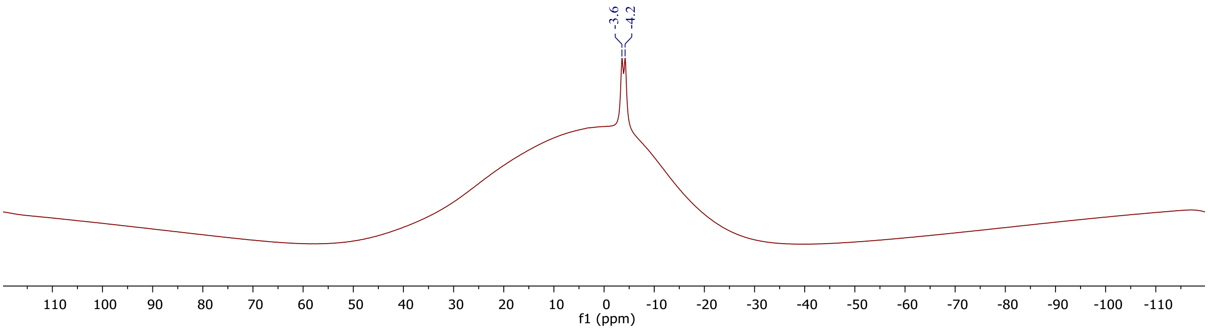

Figure S3: ^{11}B NMR spectrum of **1** (CD_2Cl_2, 160.5MHz).

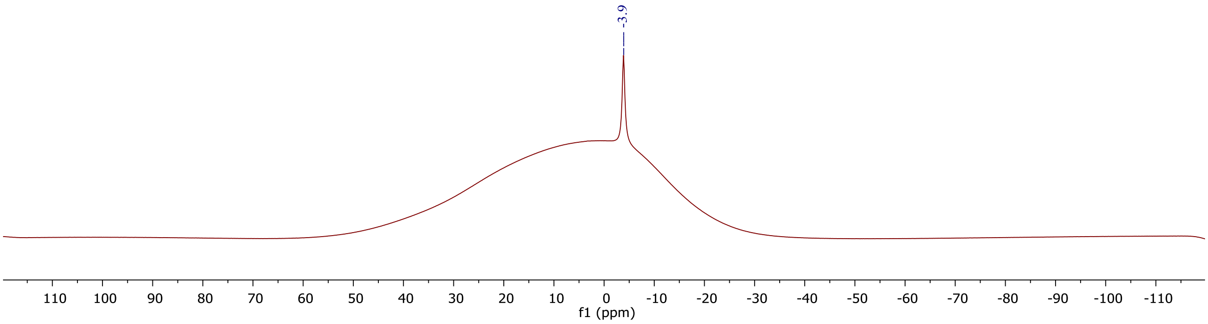

Figure S4: ^{11}B{^{1}H} NMR spectrum of **1** (CD_2Cl_2, 160.5 MHz).

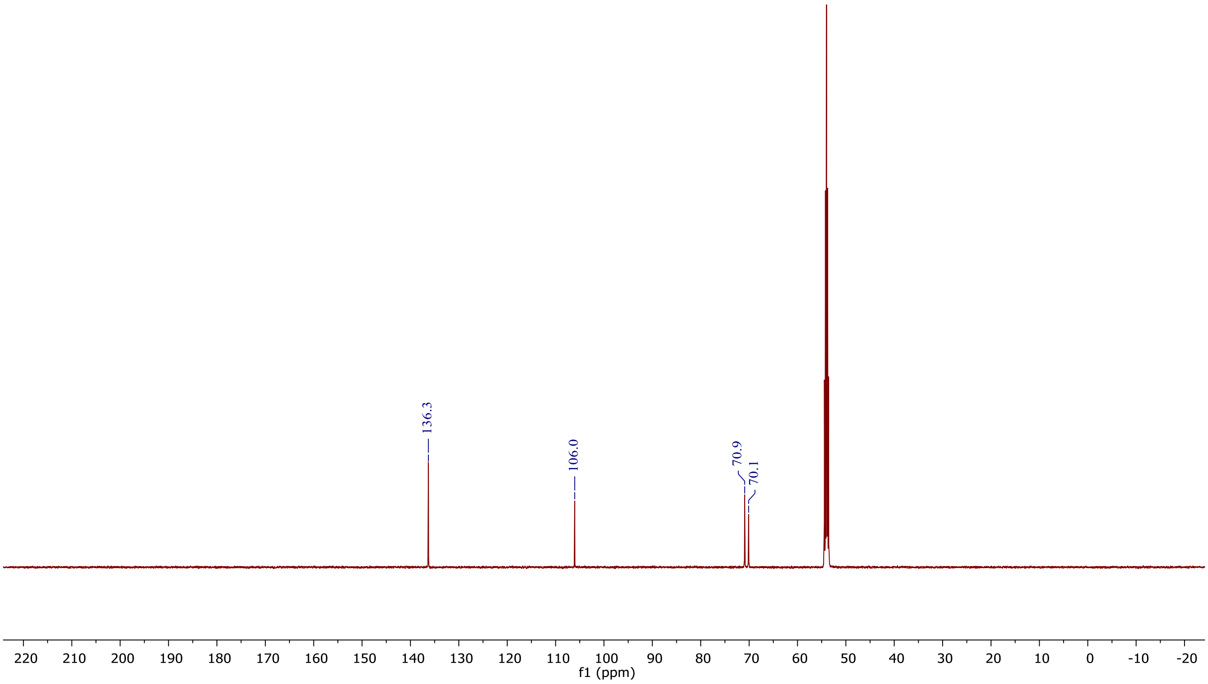

Figure S5: ^{13}C{^{1}H} NMR spectrum of **1** (CD_2Cl_2, 125.8 MHz).

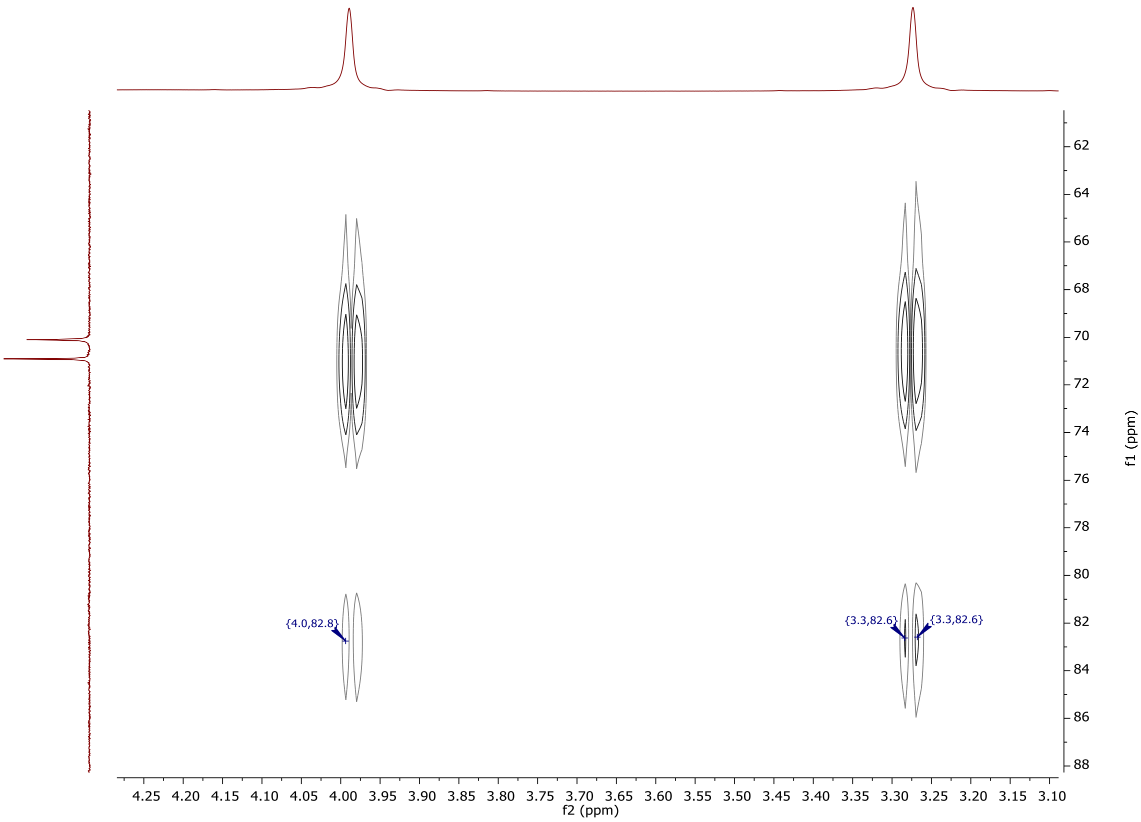

Figure S6: Section of the ^{1}H-^{13}C-HMBC NMR spectrum of **1** showing the position of the extremely broadened CpC-1 resonance (CD_2Cl_2, 500.2, 125.8 MHz).

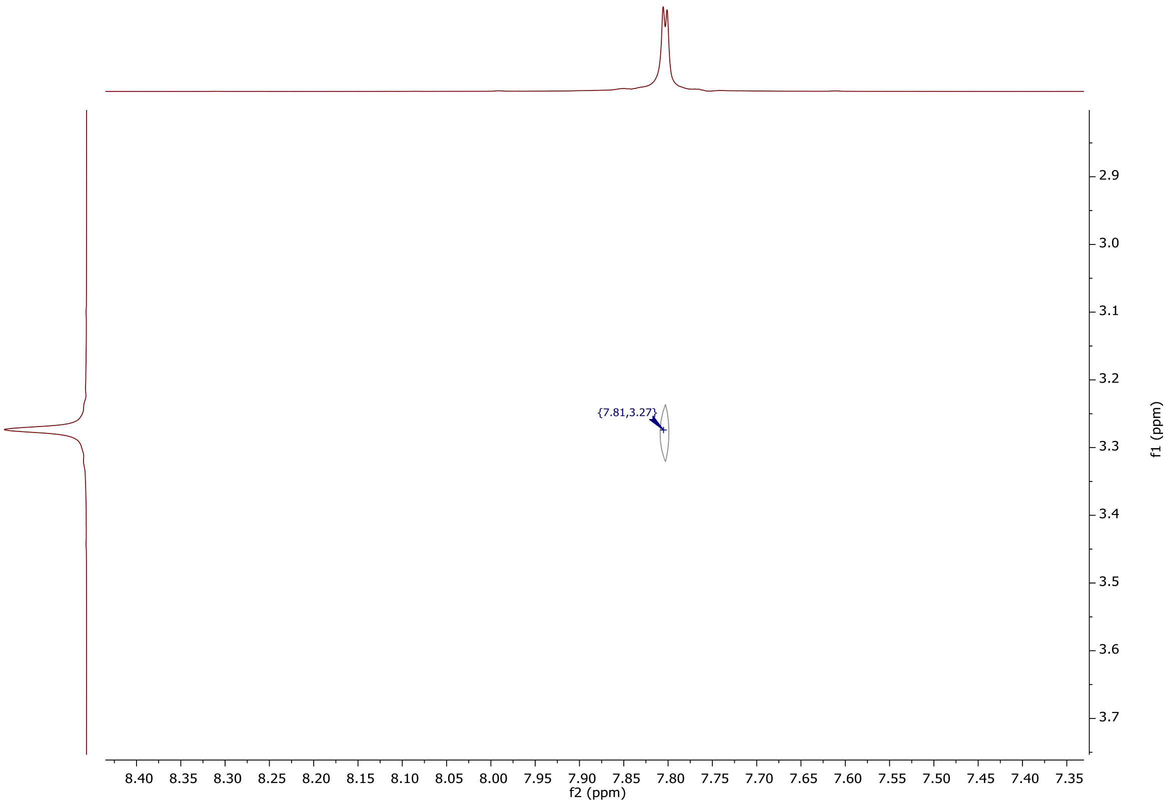

Figure S7: Section of the ^{1}H-^{1}H-NOESY NMR spectrum of **1** showing the cross-peak between the signals of pzH-3 and CpH-2 (CD_2Cl_2, 500.2, 500.2 MHz).

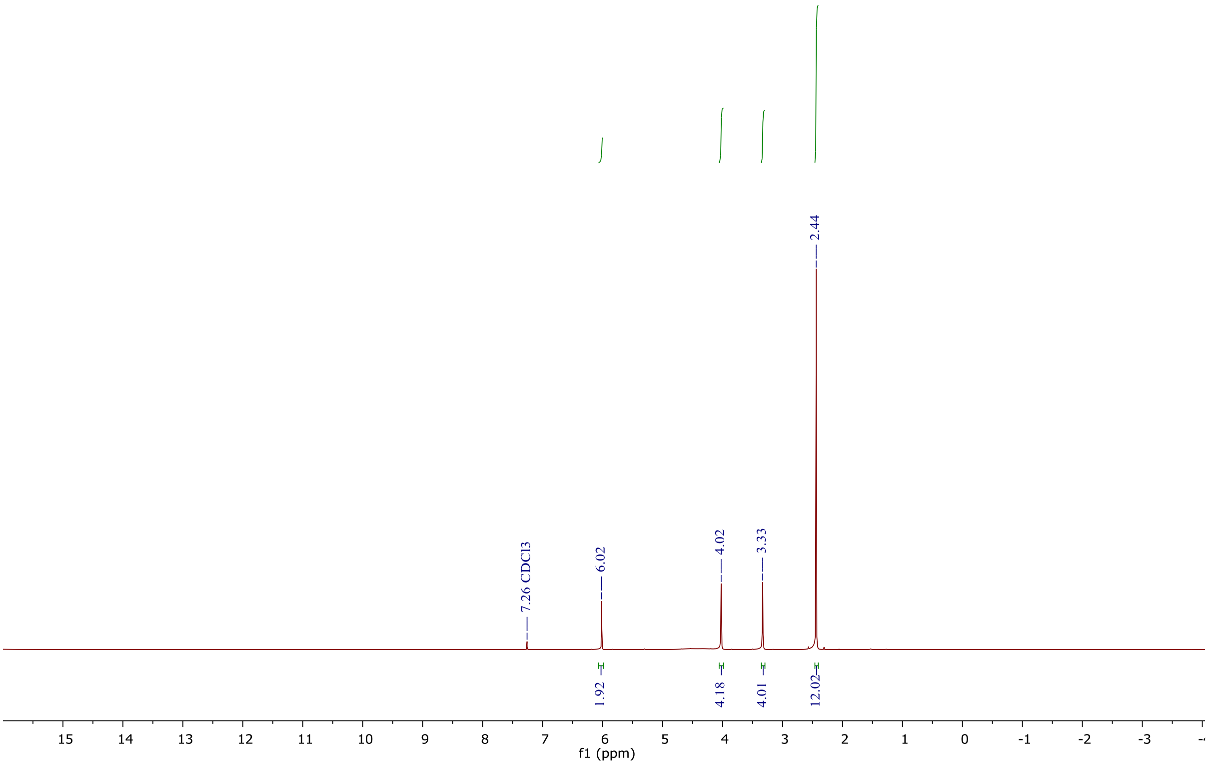

Figure S8: ^{1}H NMR spectrum of **1Me** ($CDCl_3$, 500.2 MHz).

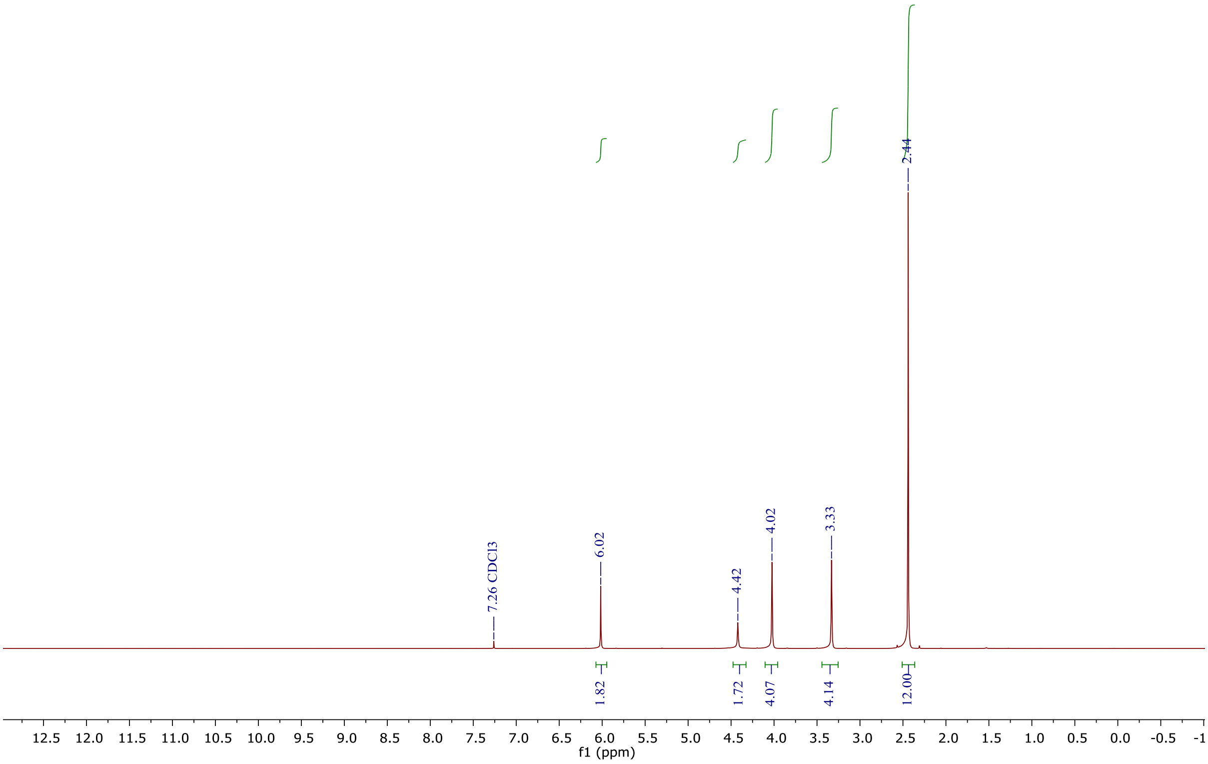

Figure S9: ^{1}H{^{11}B} NMR spectrum of **1Me** ($CDCl_3$, 500.2 MHz).

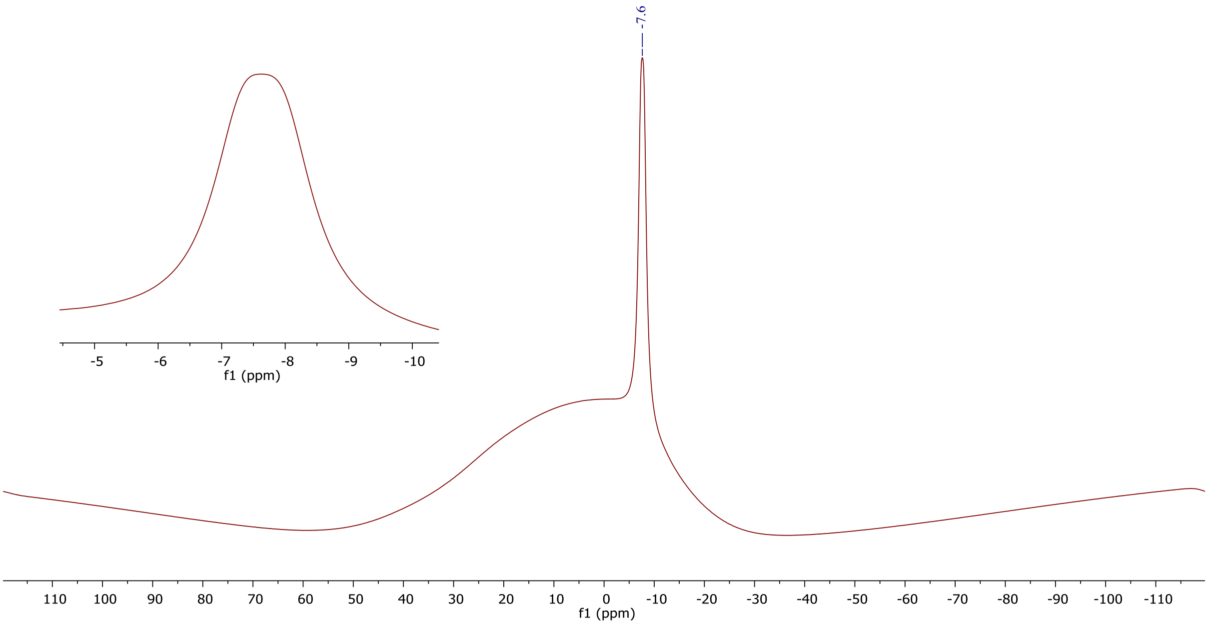

Figure S10: ^{11}B NMR spectrum of **1Me** ($CDCl_3$, 160.5 MHz).

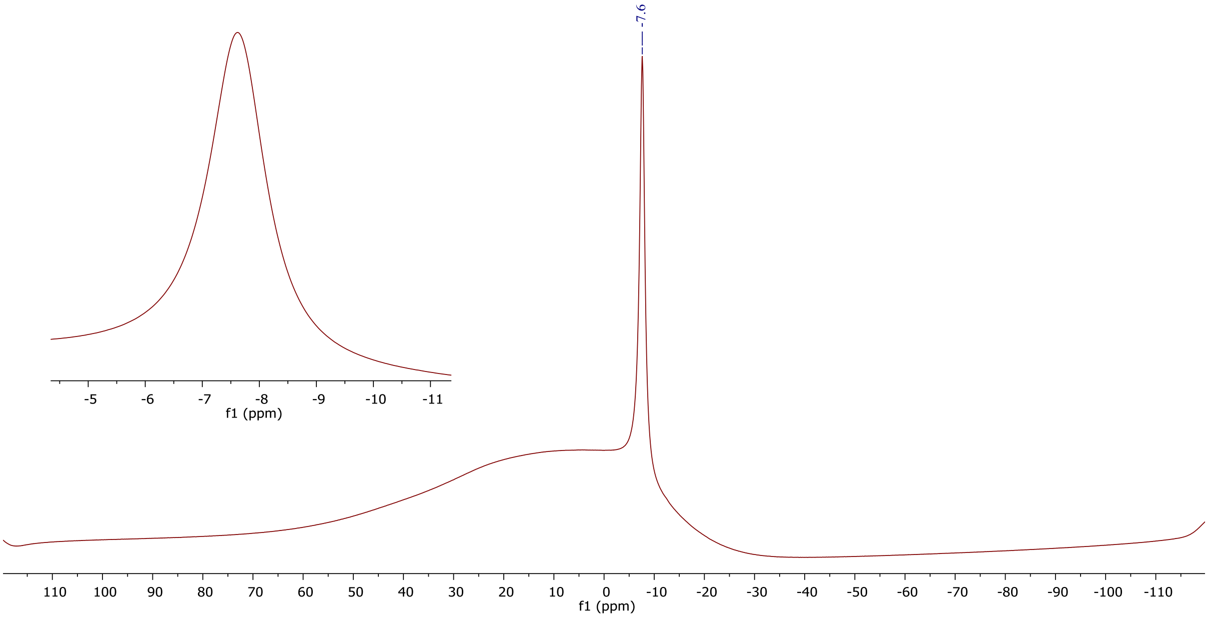

Figure S11: ^{11}B{^{1}H} NMR spectrum of **1Me** ($CDCl_3$, 160.5 MHz).

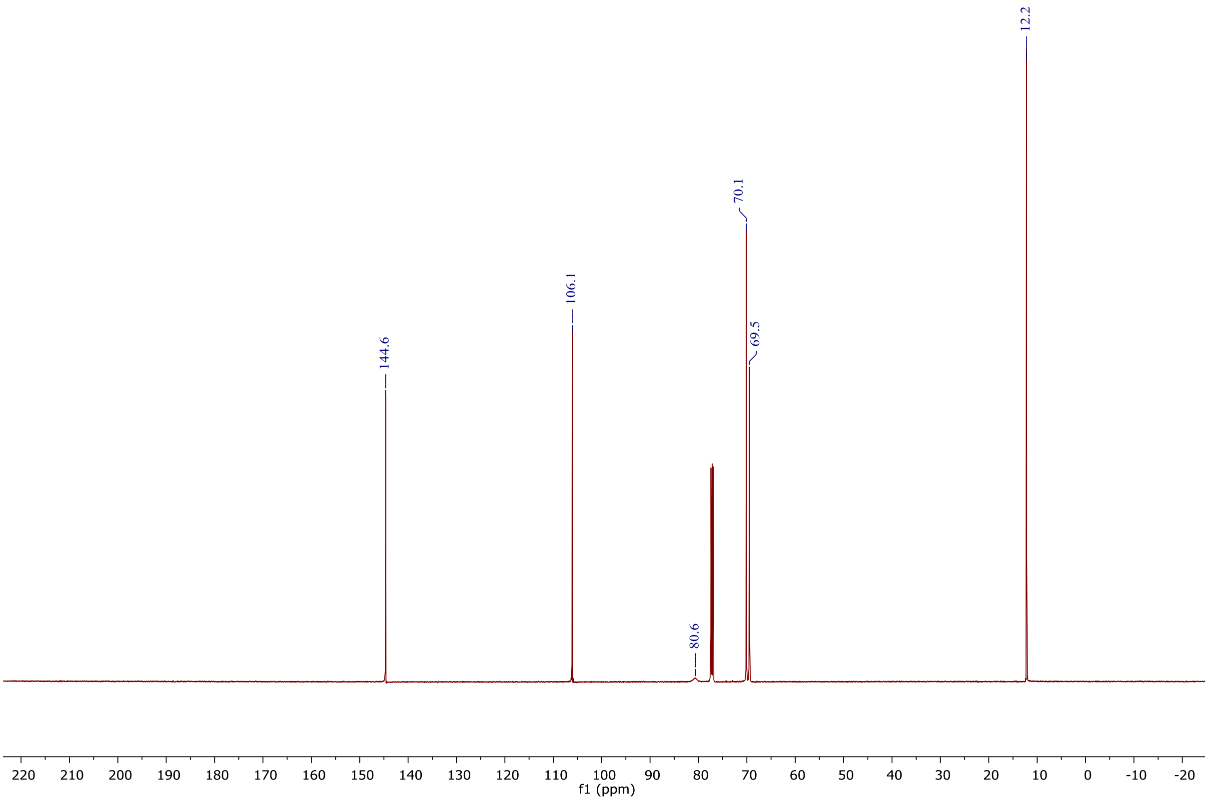

Figure S12: $^{13}C\{^1H\}$ NMR spectrum of **1Me** ($CDCl_3$, 125.8 MHz).

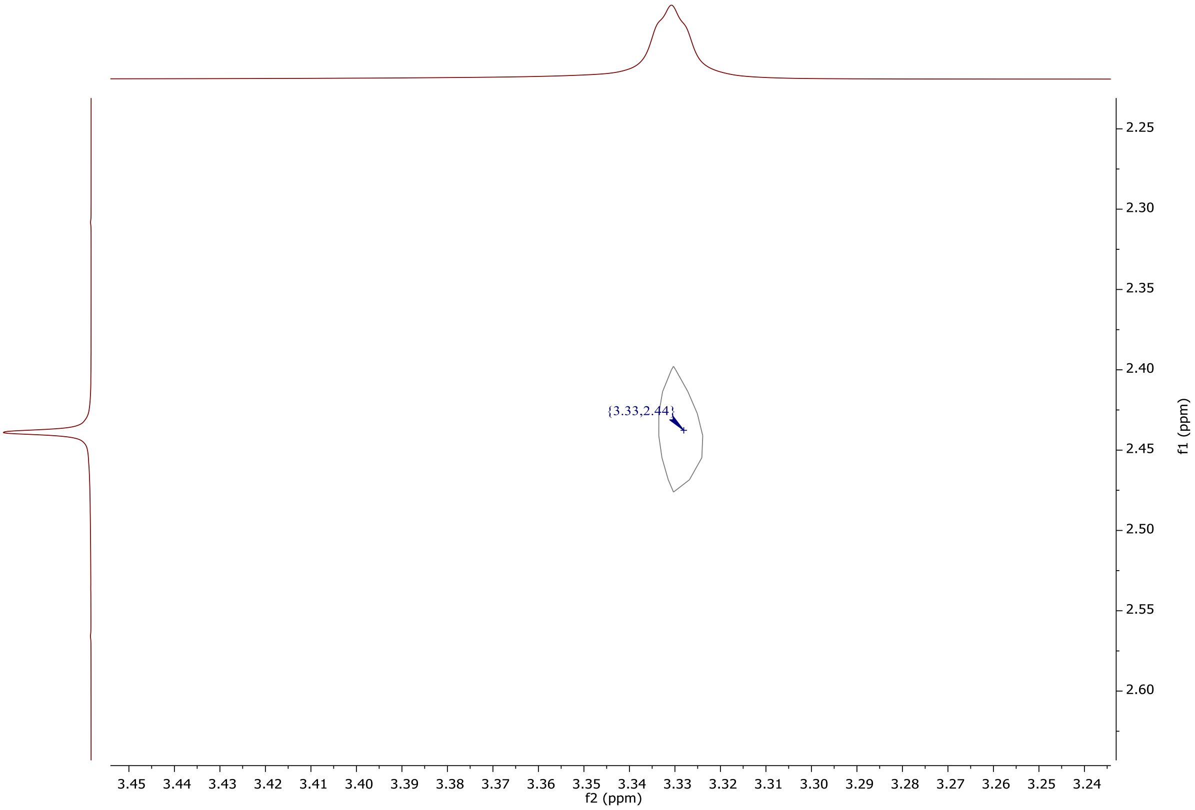

Figure S13: Section of the ^1H-^1H-NOESY NMR spectrum of **1Me** showing the cross-peak between the signals of $pzCH_3$ and CpH-2 ($CDCl_3$, 400.1, 400.1MHz).

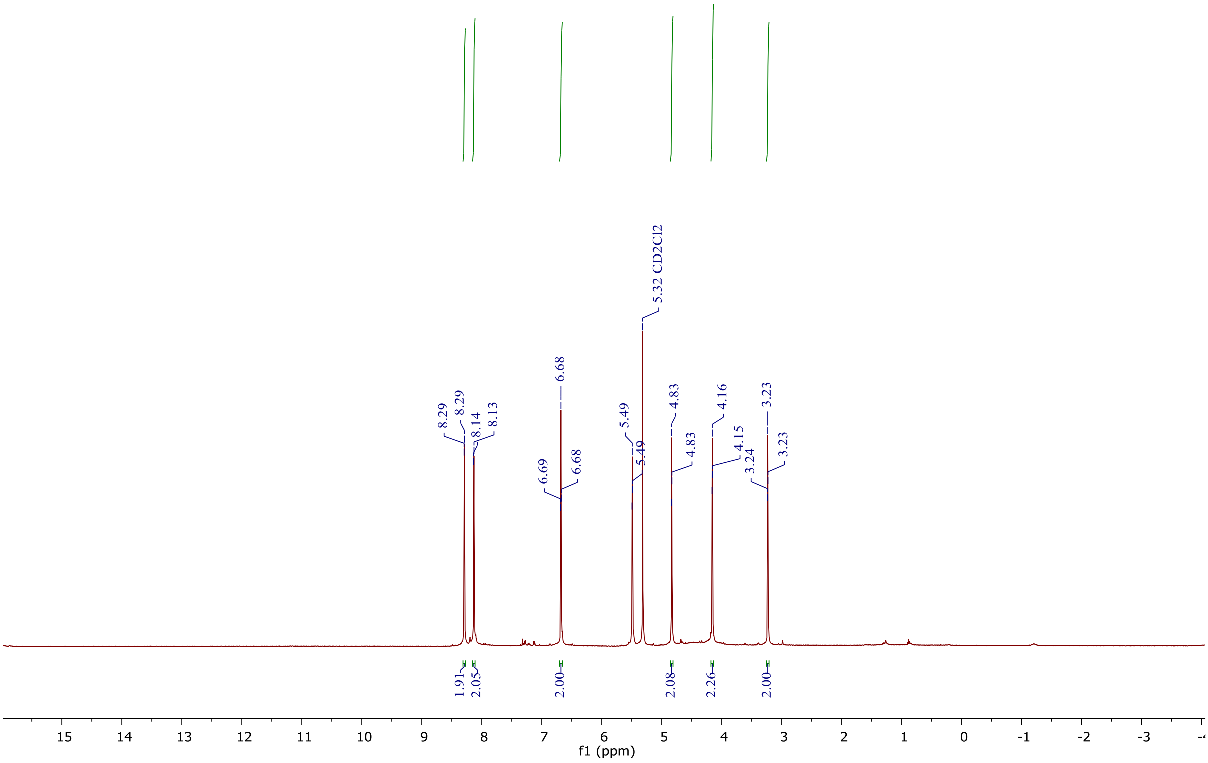

Figure S14: ^{1}H NMR spectrum of [**2**][B(C_6F_5)$_4$] (CD_2Cl_2, 500.2 MHz).

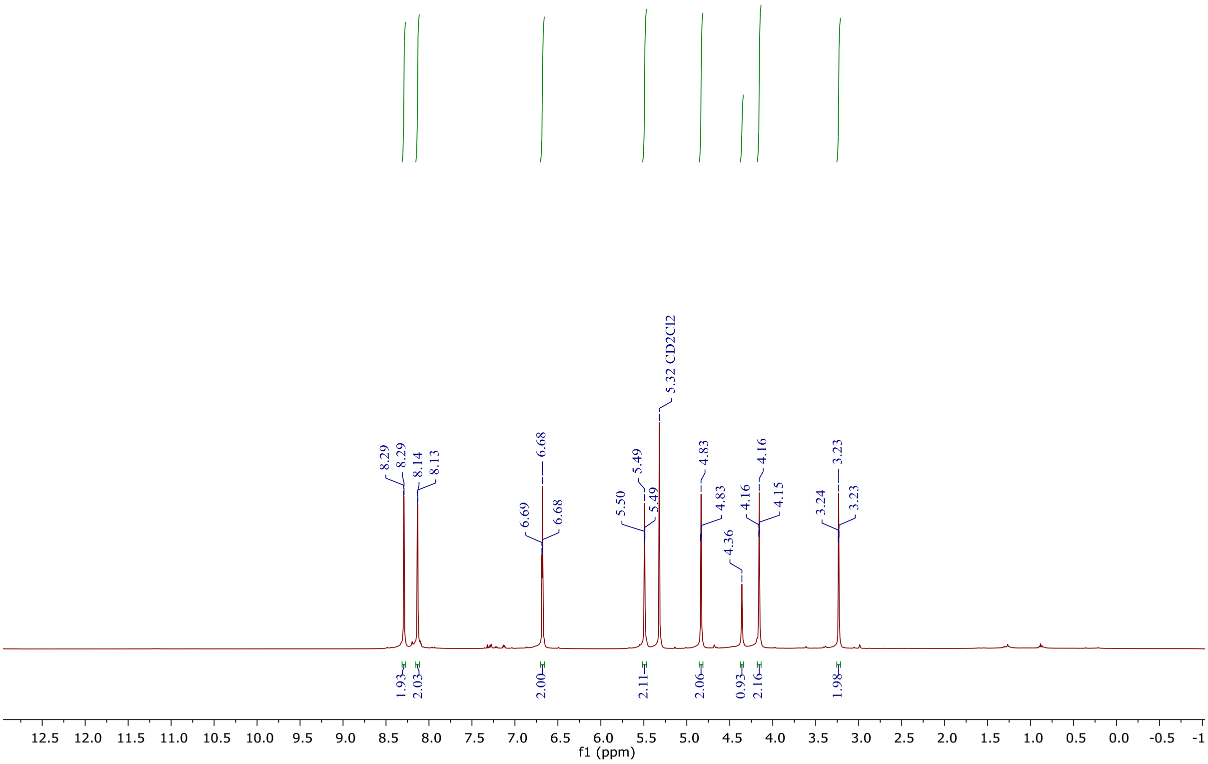

Figure S15: ^{1}H{^{11}B} NMR spectrum of [**2**][B(C_6F_5)$_4$] (CD_2Cl_2, 500.2 MHz).

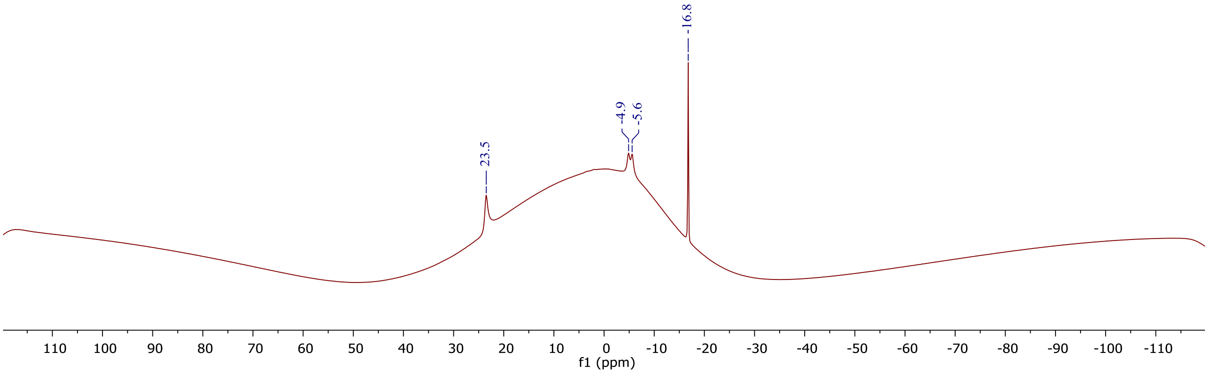

Figure S16: ^{11}B NMR spectrum of [**2**][B(C_6F_5)$_4$] (CD_2Cl_2, 160.5 MHz).

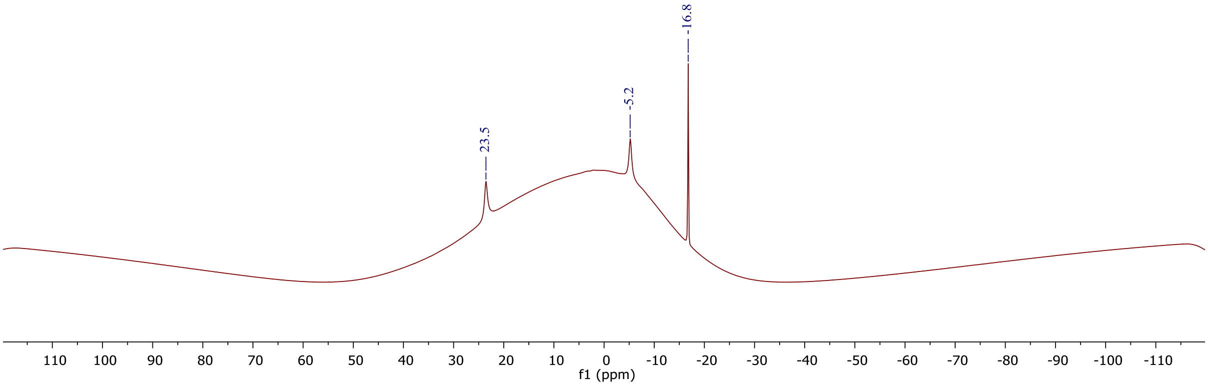

Figure S17: ^{11}B{^{1}H} NMR spectrum of [**2**][B(C_6F_5)$_4$] (CD_2Cl_2, 160.5 MHz).

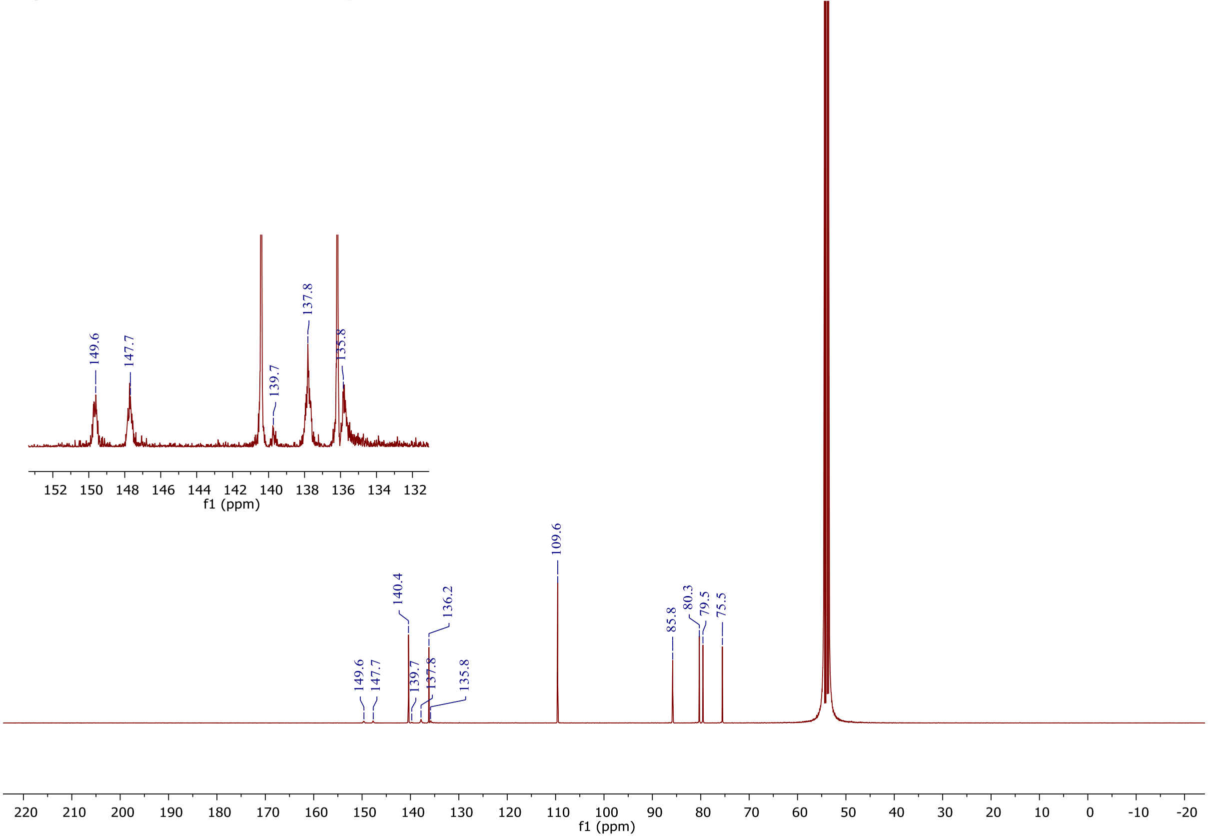

Figure S18: ^{13}C{^{1}H} NMR spectrum of [**2**][B(C_6F_5)$_4$] (CD_2Cl_2, 125.8 MHz).

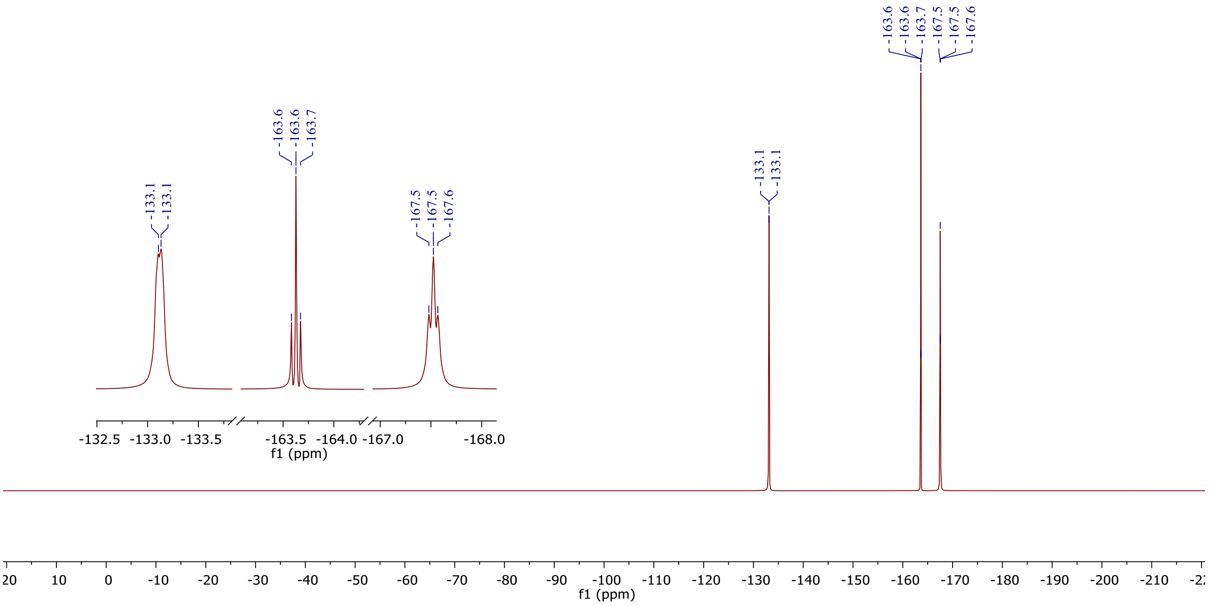

Figure S19: ^{19}F NMR spectrum of [**2**][B(C_6F_5)$_4$] (CD_2Cl_2, 470.6 MHz).

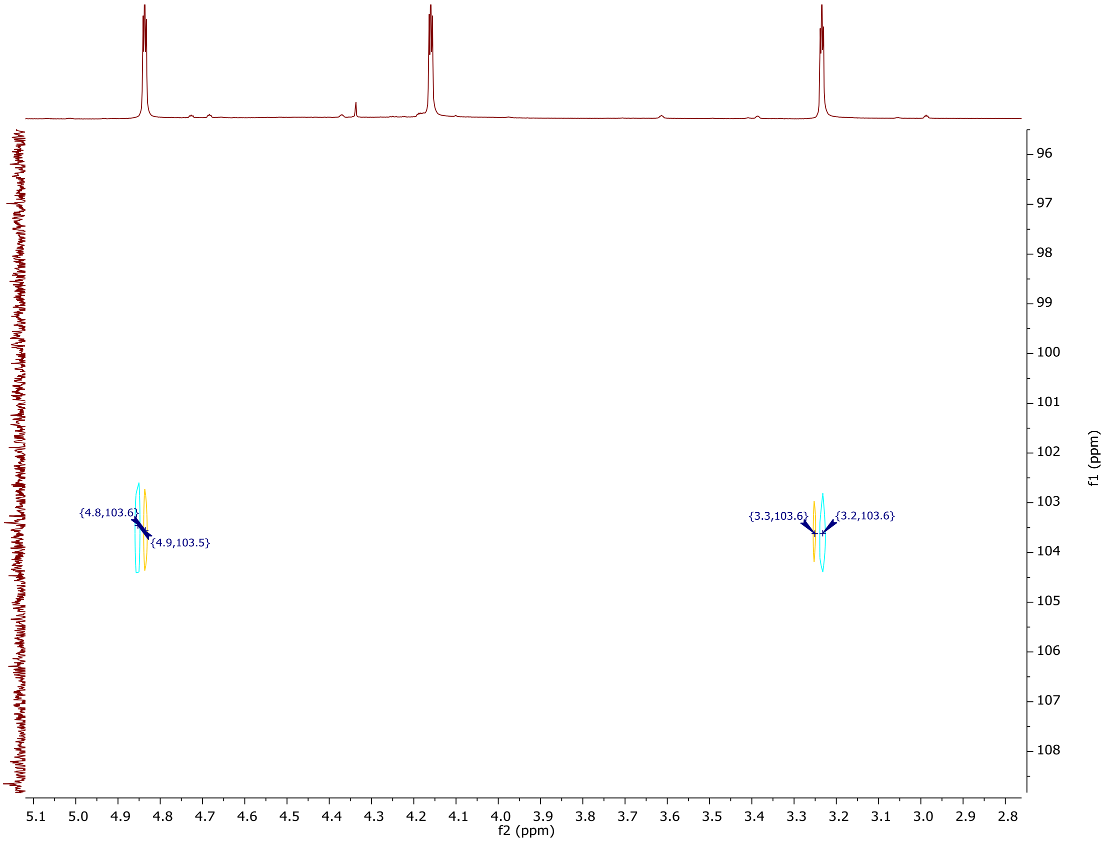

Figure S20: Section of the ^{1}H-^{13}C-HMBC NMR spectrum of [**2**][B(C_6F_5)$_4$] showing the position of the extremely broadened CpC-1 resonance (CD_2Cl_2, 400.1, 100.6 MHz).

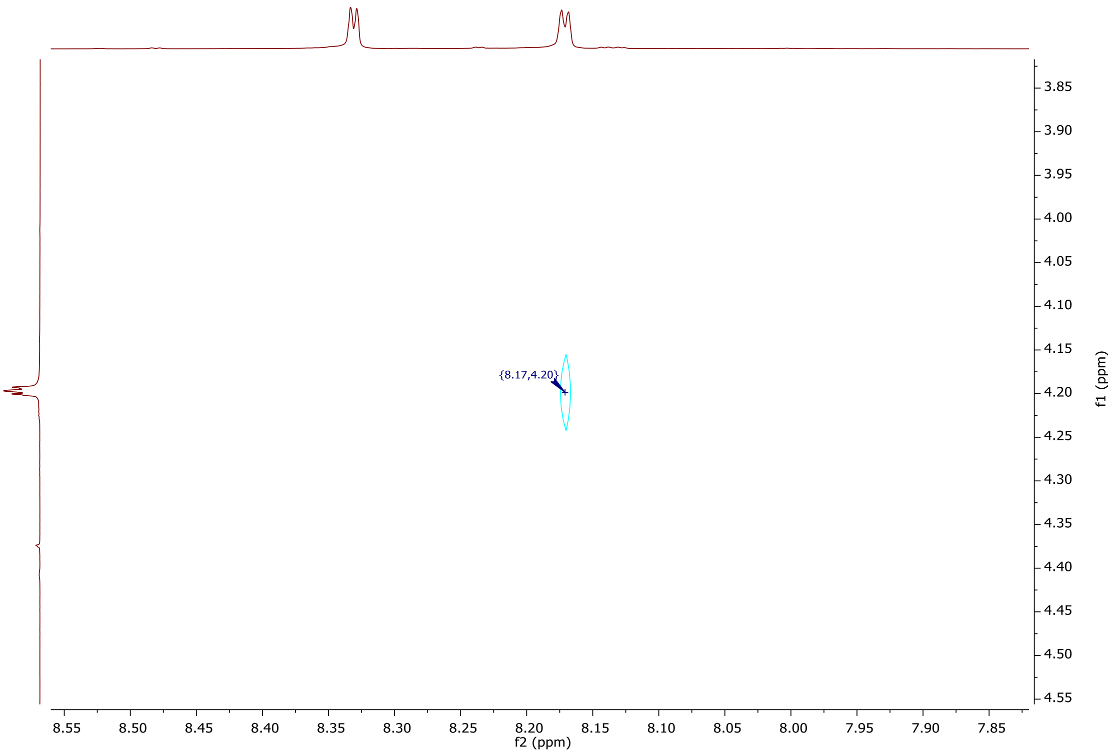

Figure S21: Section of the ^{1}H-^{1}H-NOESY NMR spectrum of [**2**][B(C_6F_5)$_4$] showing the cross-peak between the signals of pzH-3' and CpH-2' (CD_2Cl_2, 400.1, 400.1 MHz).

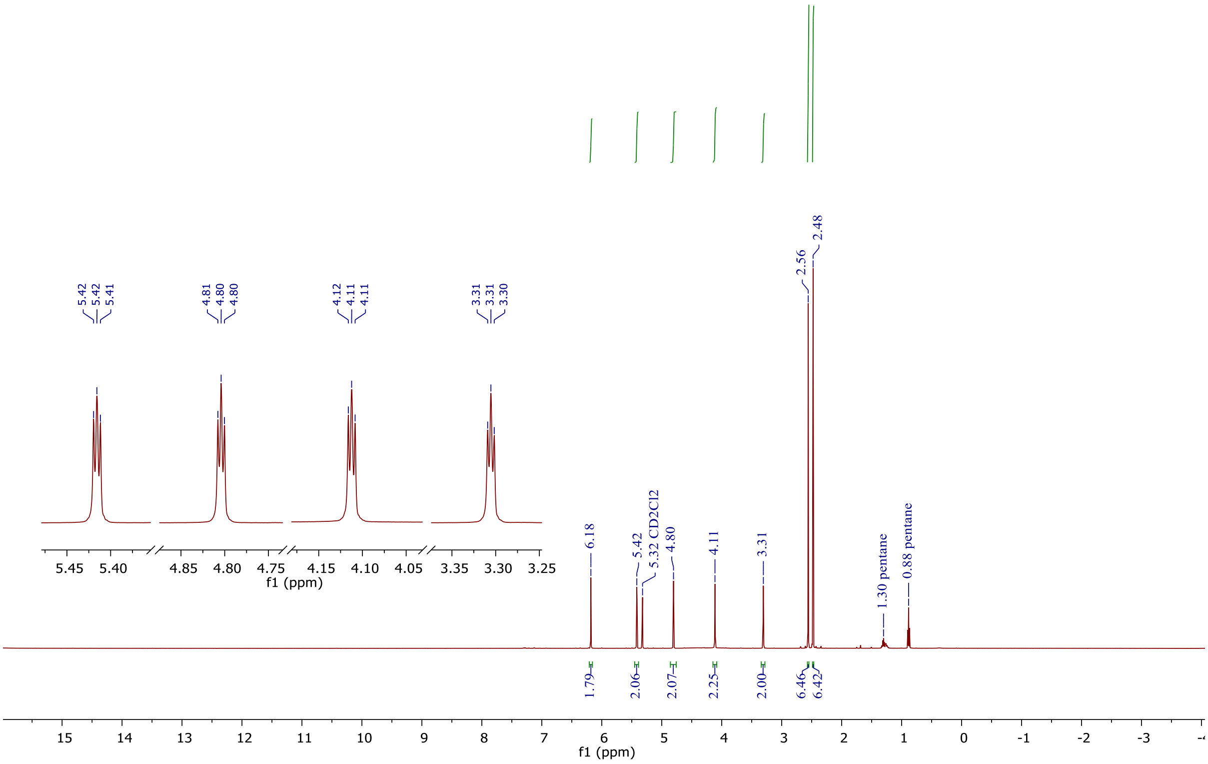

Figure S22: ^{1}H NMR spectrum of [**2Me**][B(C_6F_5)$_4$] (CD_2Cl_2, 500.2 MHz).

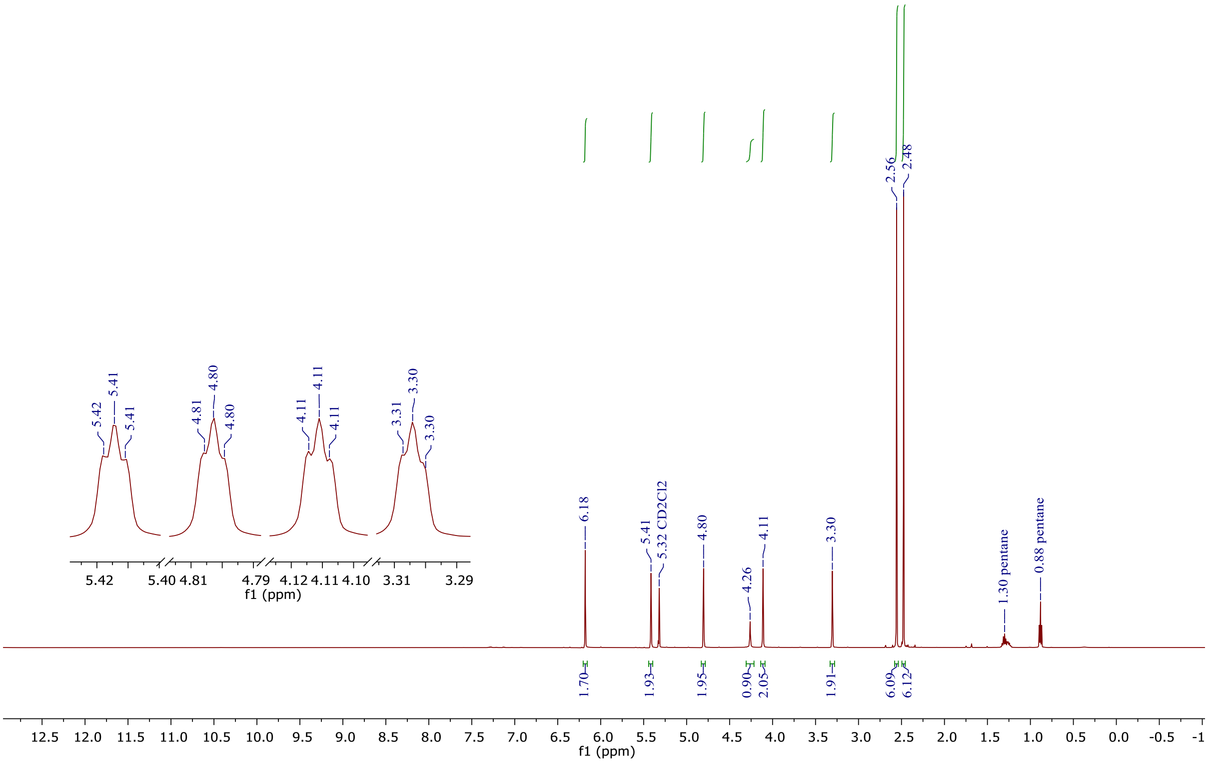

Figure S23: $^1H\{^{11}B\}$ NMR spectrum of [**2Me**][B(C_6F_5)$_4$] (CD_2Cl_2, 500.2 MHz).

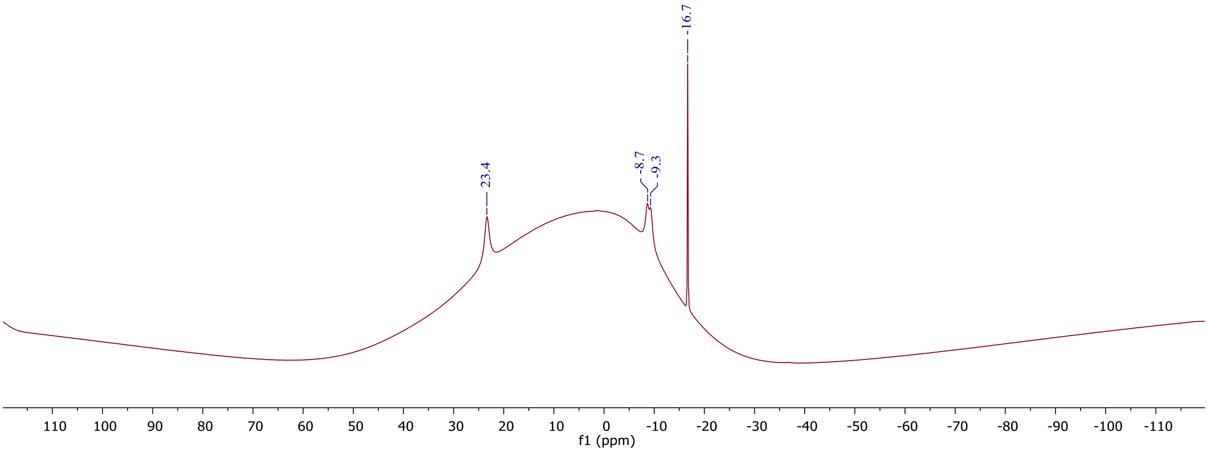

Figure S24: ^{11}B NMR spectrum of [**2Me**][B(C_6F_5)$_4$] (CD_2Cl_2, 160.5 MHz)

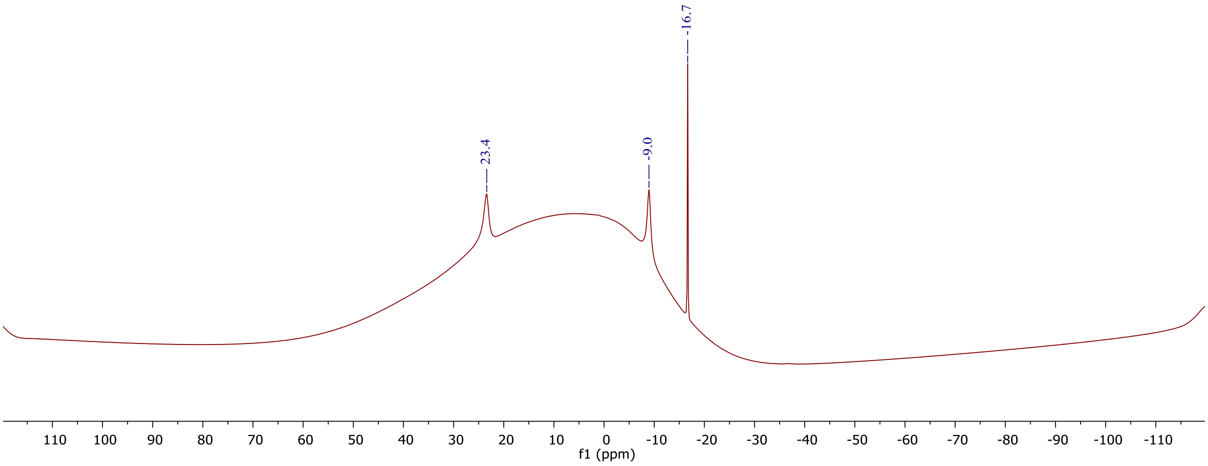

Figure S25: $^{11}B\{^1H\}$ NMR spectrum of [**2Me**][$B(C_6F_5)_4$] (CD_2Cl_2, 160.5 MHz)

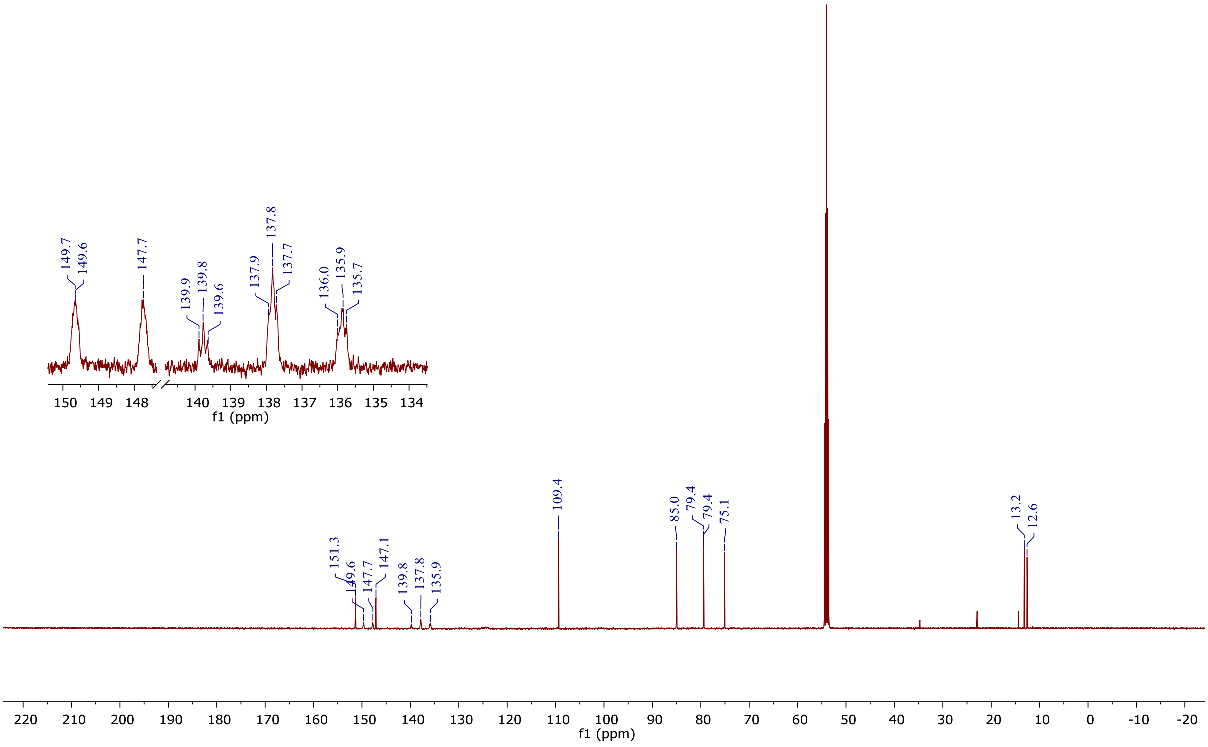

Figure S26: $^{13}C\{^1H\}$ NMR spectrum of [**2Me**][$B(C_6F_5)_4$] (CD_2Cl_2, 125.8 MHz).

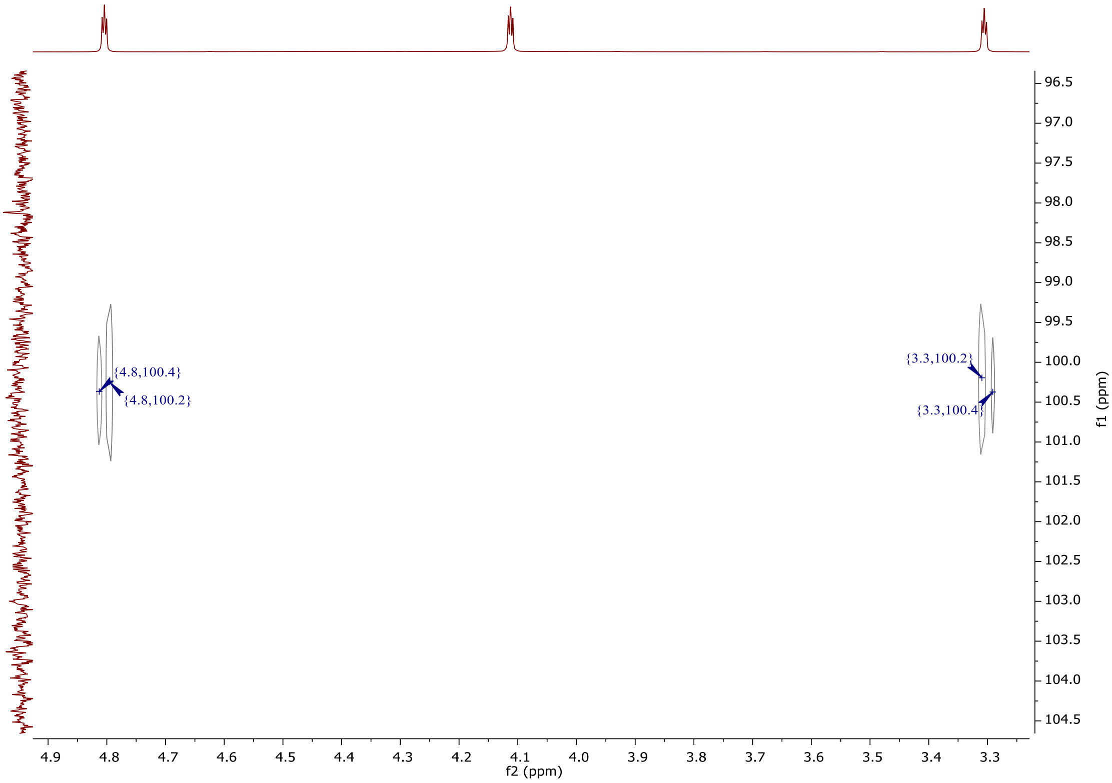

Figure S27: Section of the ^{1}H-^{13}C-HMBC NMR spectrum of [**2Me**][B(C_6F_5)$_4$] showing the position of the extremely broadened CpC-1 resonance (CD_2Cl_2, 400.1, 100.6 MHz).

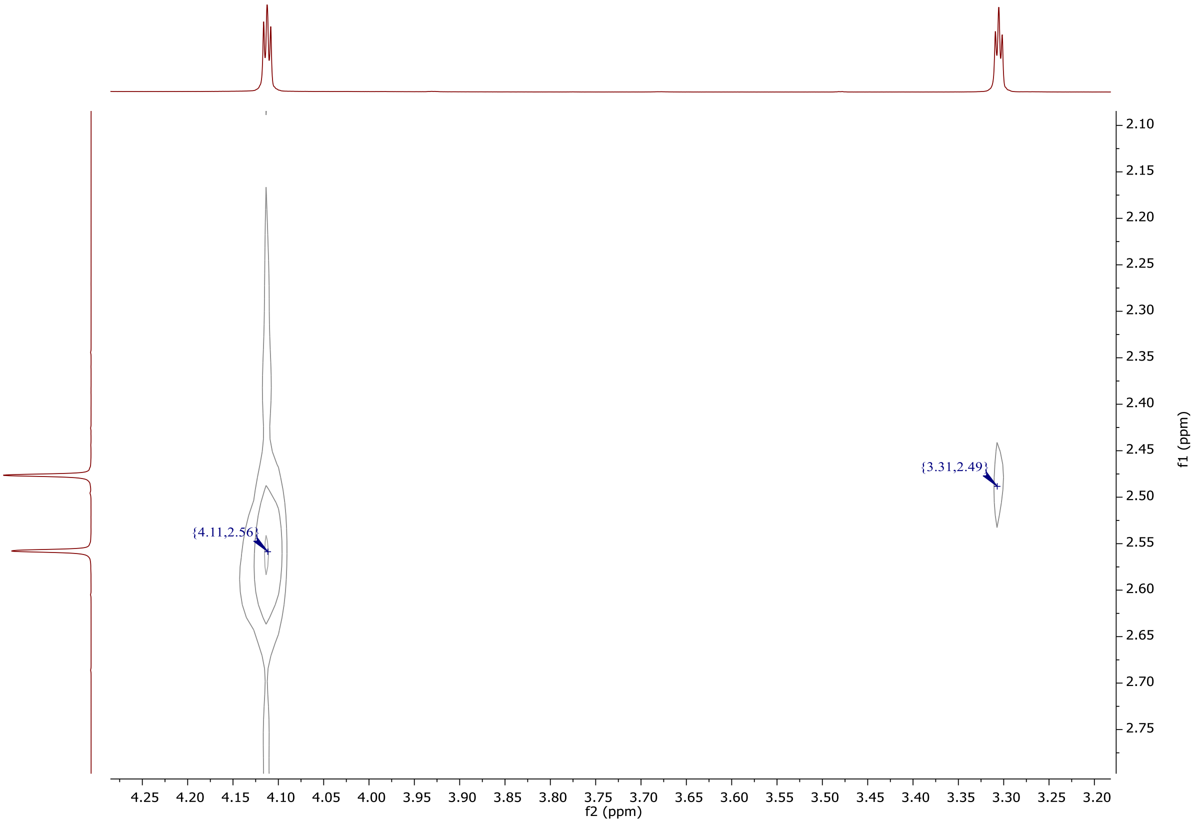

Figure S28: Section of the ^{1}H-^{1}H-NOESY NMR spectrum of [**2Me**][B(C_6F_5)$_4$] showing the cross-peaks between the resonances of CpH-2'/pzCH$_3$-3' (higher intensity => shorter distance) and CpH-2/pzCH$_3$-3 (CD_2Cl_2, 400.1, 400.1 MHz).

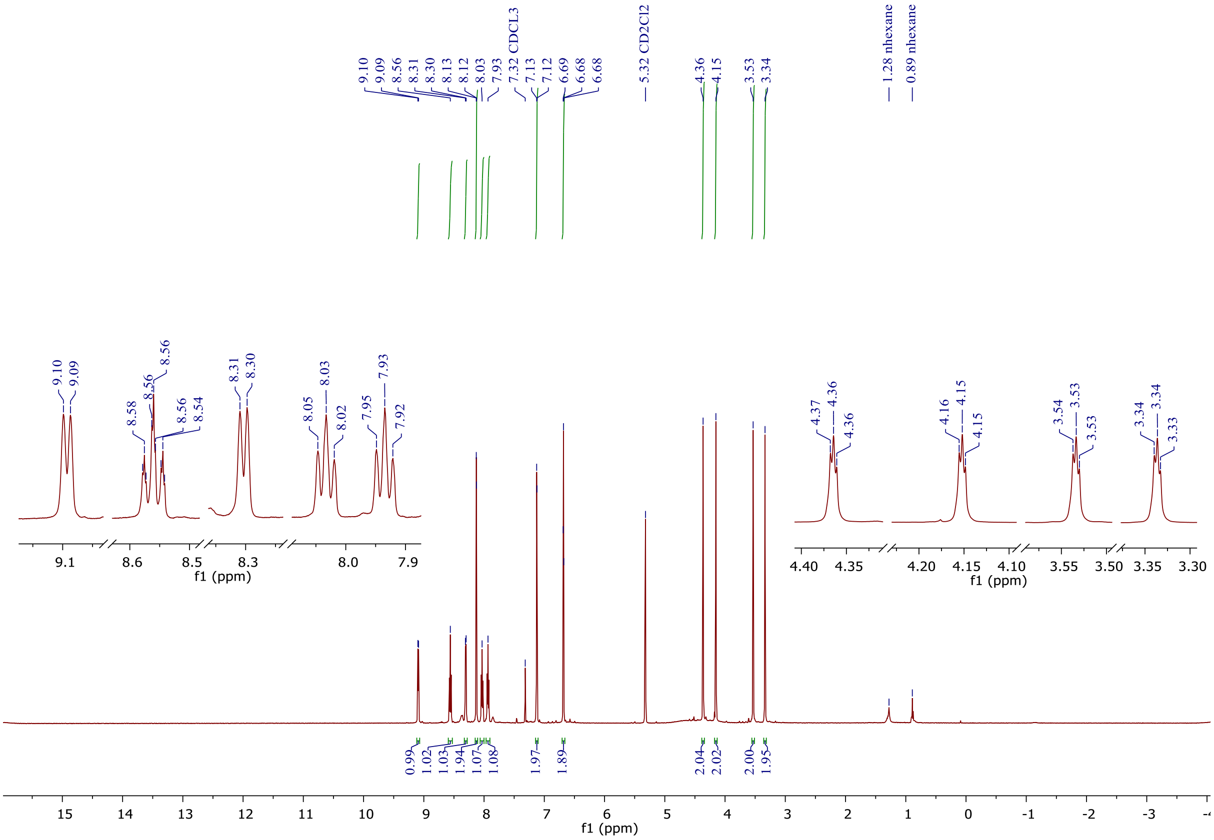

Figure S29: ^{1}H NMR spectrum of [**2**·py][B(C$_6$F$_5$)$_4$] (CD$_2$Cl$_2$, 500.2 MHz).

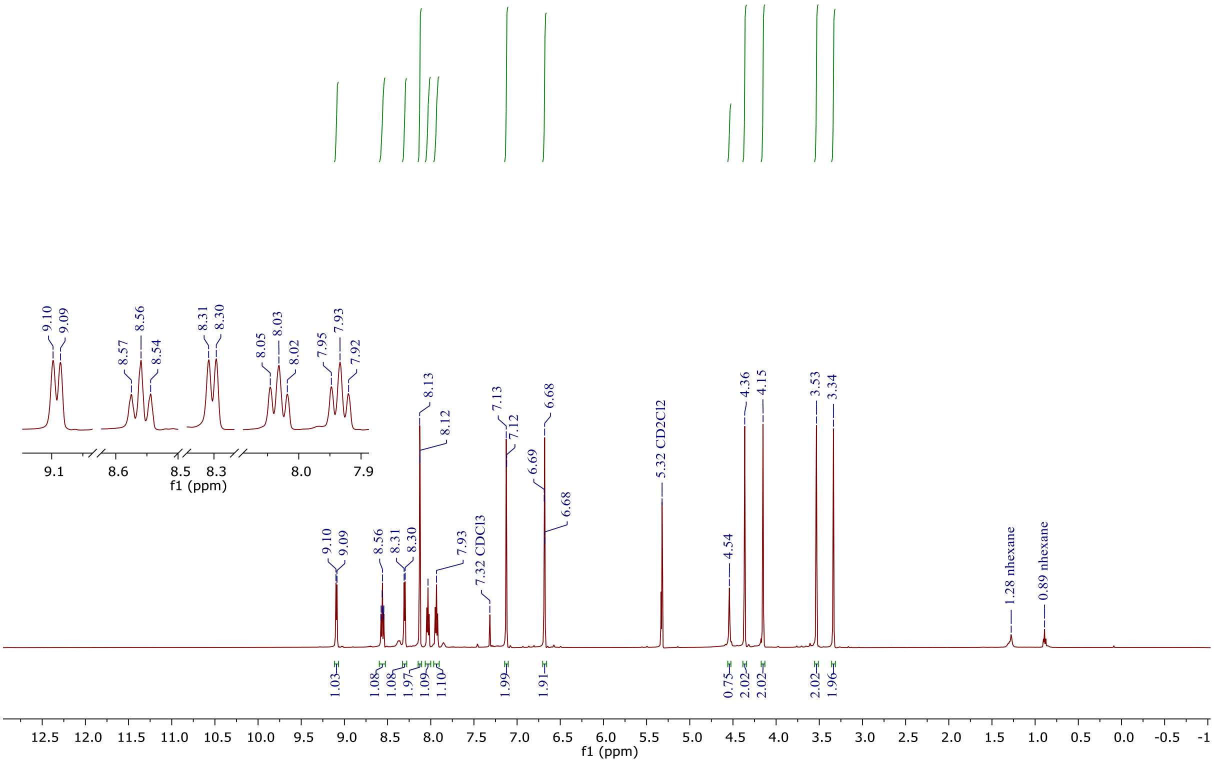

Figure S30: ^{1}H{^{11}B} NMR spectrum of [**2**·py][B(C$_6$F$_5$)$_4$] (CD$_2$Cl$_2$, 500.2 MHz).

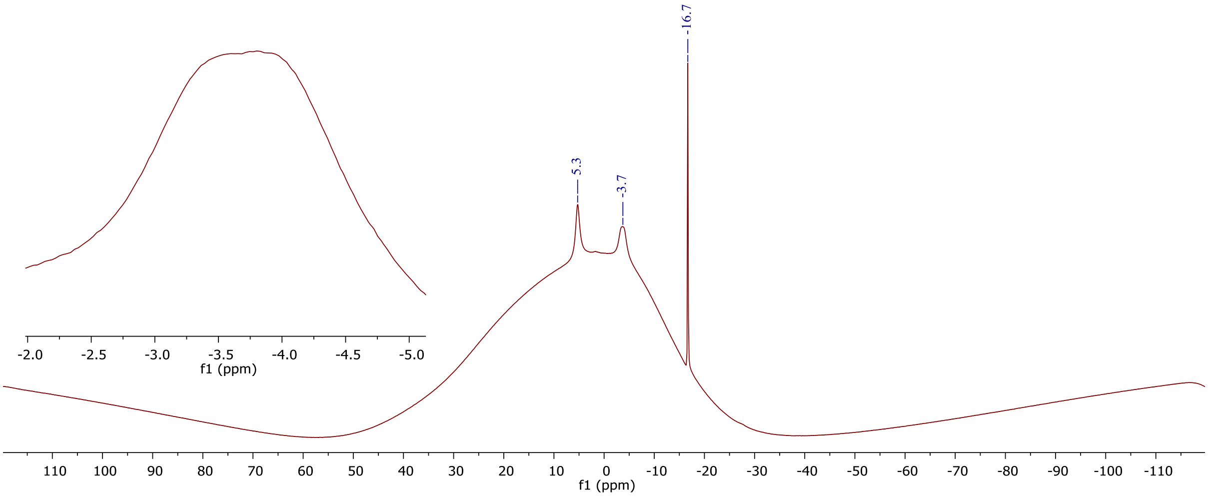

Figure S31: ^{11}B NMR spectrum of [**2**·py][B(C_6F_5)$_4$] (CD_2Cl_2, 160.5 MHz).

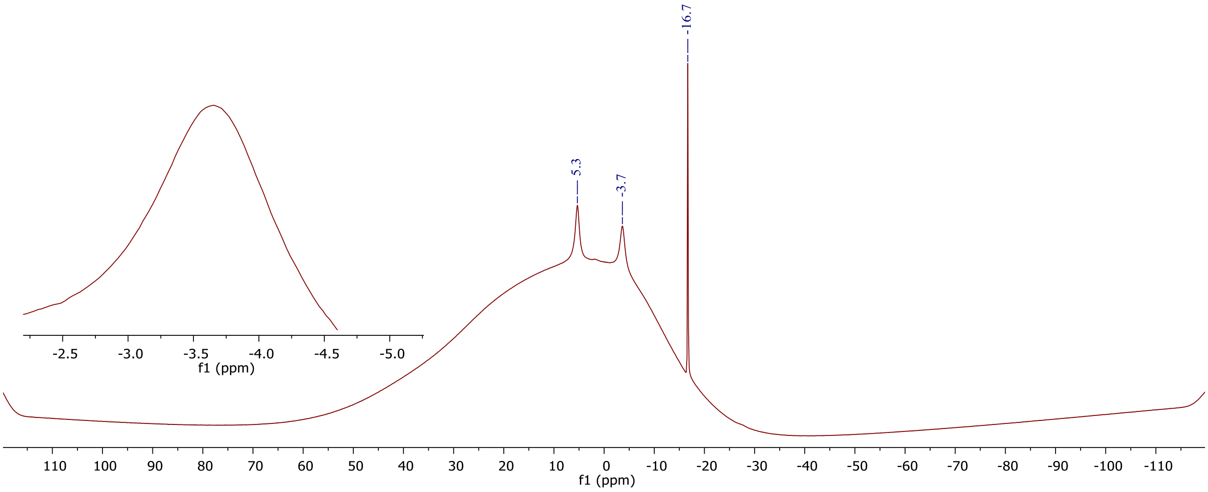

Figure S32: ^{11}B{^{1}H} NMR spectrum of [**2**·py][B(C_6F_5)$_4$] (CD_2Cl_2, 160.5 MHz).

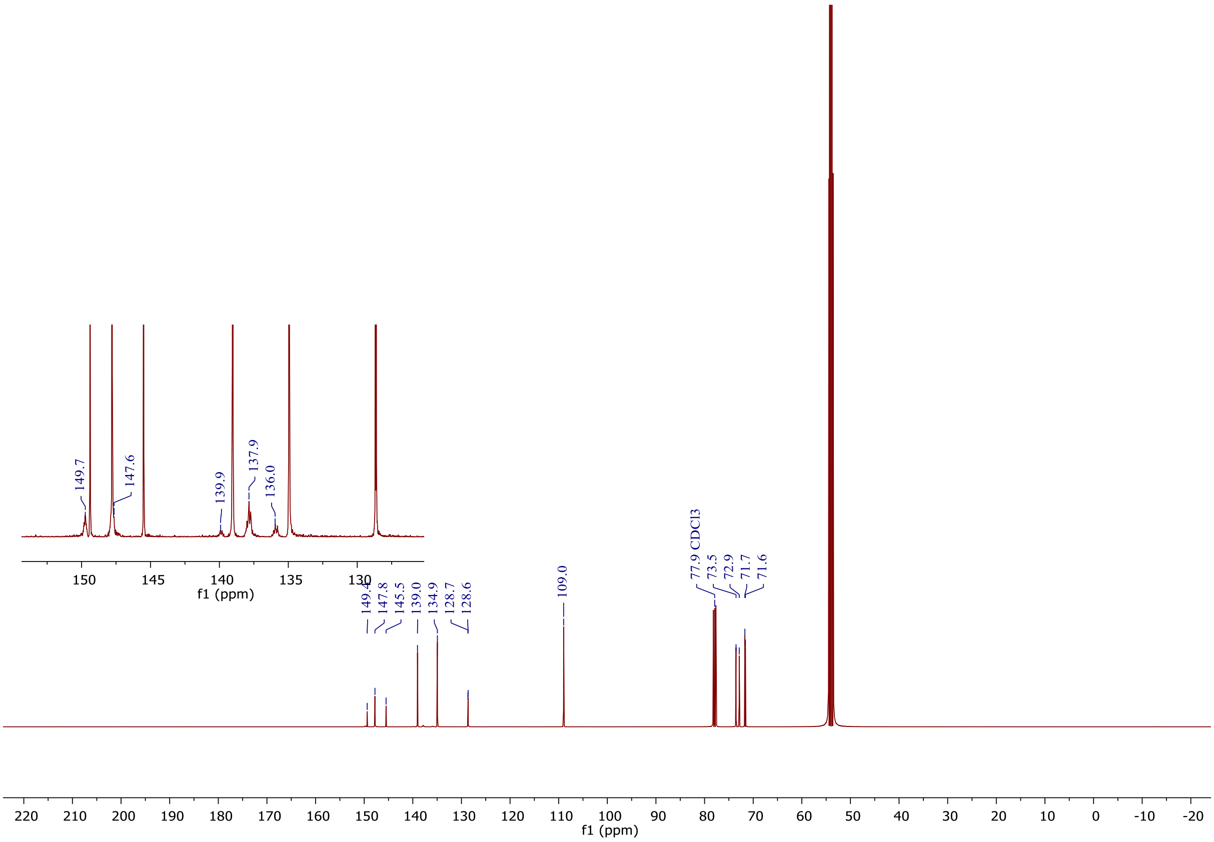

Figure S33: ^{13}C NMR spectrum of [**2**·py][B(C_6F_5)$_4$] (CD_2Cl_2, 125.8 MHz).

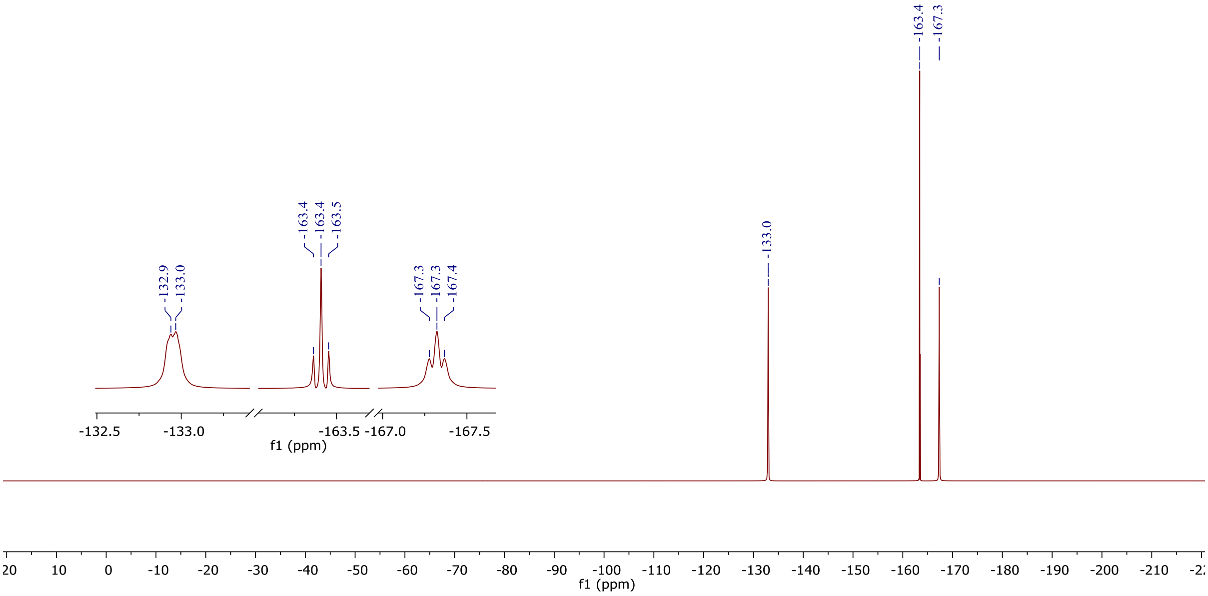

Figure S34: ^{19}F NMR spectrum of [**2**·py][B(C_6F_5)$_4$] (CD_2Cl_2, 470.6 MHz).

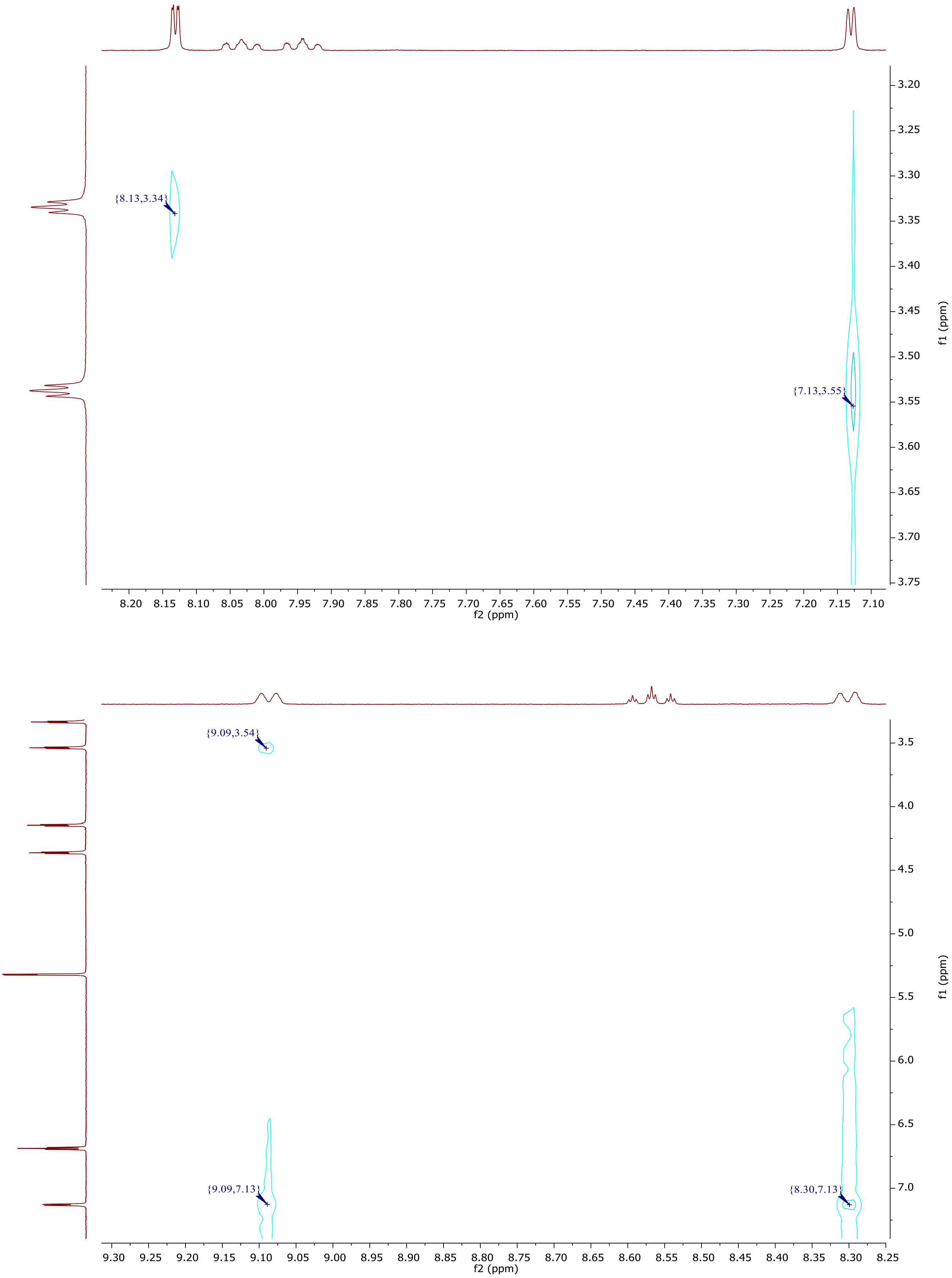

Figure S35: Sections of the ^{1}H-^{1}H-NOESY NMR spectrum of [**2**·py][B(C_6F_5)$_4$] (CD_2Cl_2, 400.1, 400.1 MHz).

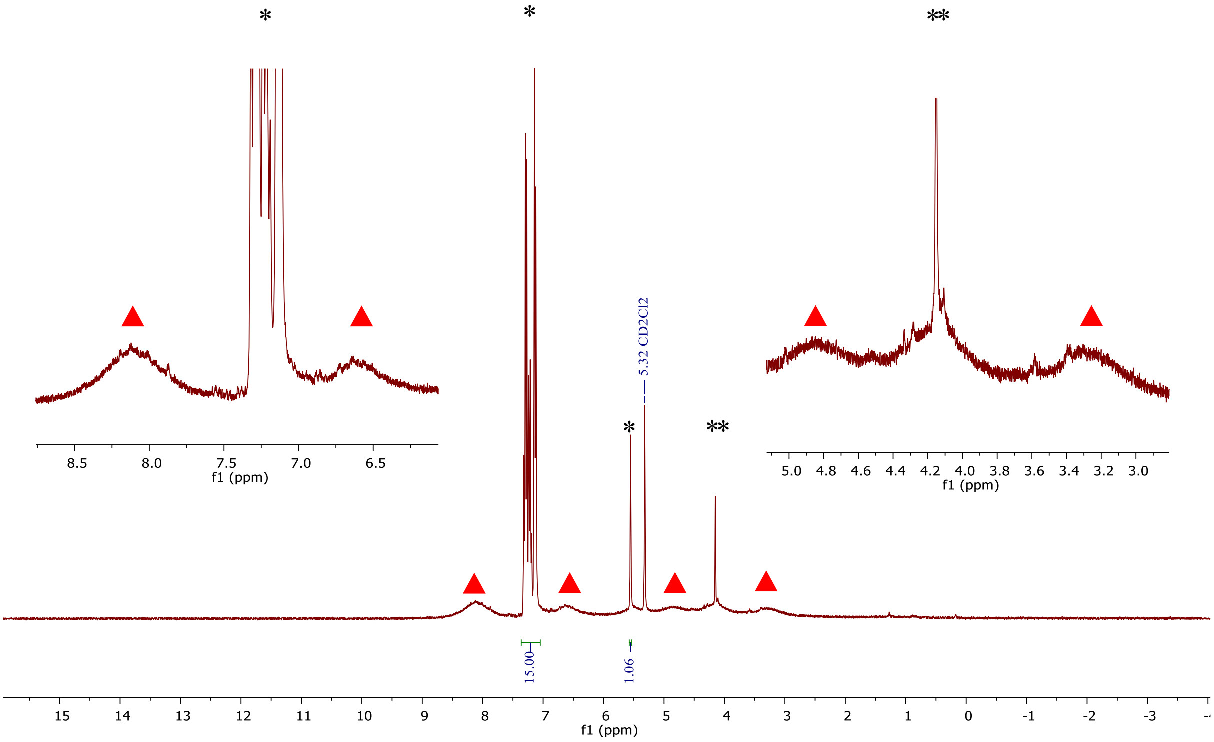

Figure S36: ^{1}H NMR spectrum (300.0 MHz) recorded on a mixture of **1** (1.0 eq) and [Ph$_3$C][B(C$_6$F$_5$)$_4$] (0.8 eq) in CD$_2$Cl$_2$. ▲ : Signals of residual **1** and the product [**2**][B(C$_6$F$_5$)$_4$], which are broadened due to a dynamic H$^-$-transfer equilibrium between both species. *) Ph$_3$CH, **) ferrocene.

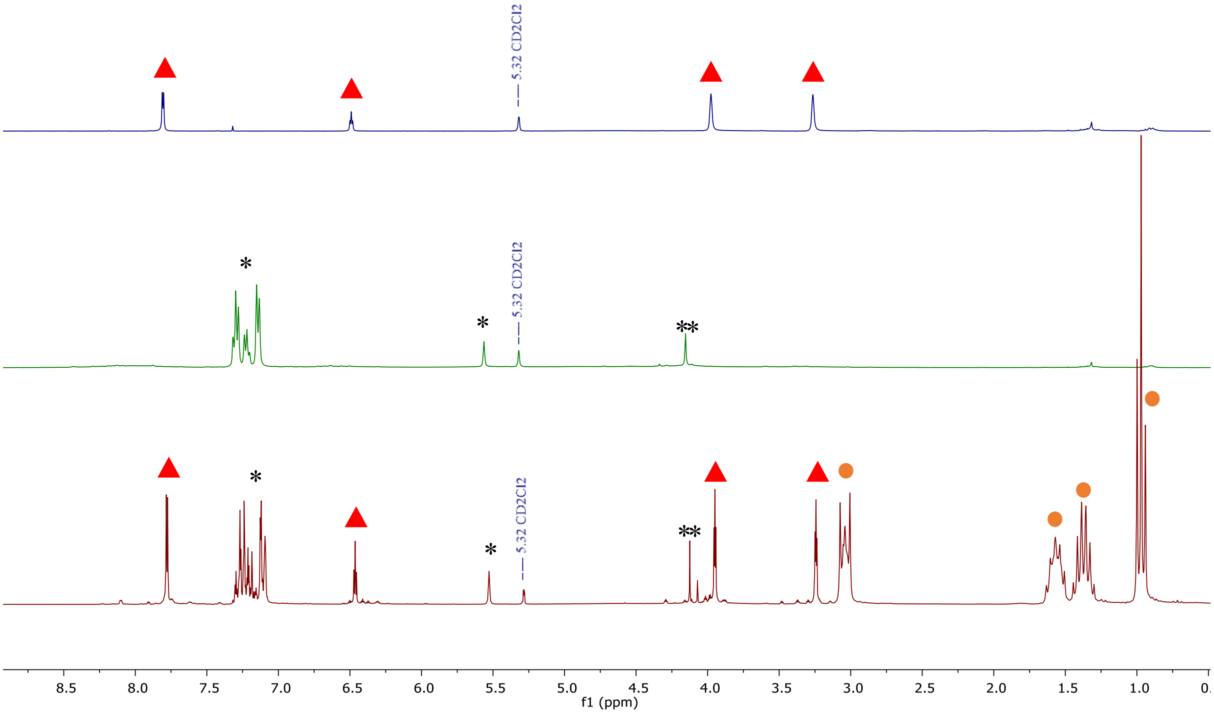

Figure S37: Top: ^{1}H NMR spectrum (CD_2Cl_2, 250.2 MHz) recorded on a sample of **1** (1.0 eq); middle: ^{1}H NMR spectrum (400.2 MHz) recorded on the same sample after the addition of $[Ph_3C][B(C_6F_5)_4]$ (0.9 eq); bottom: ^{1}H NMR spectrum (250.2 MHz) recorded on the previous sample after the addition of [*n*Bu$_4$N][BH$_4$] (1.0 eq of $[BH_4]^-$). ▲ : **1**, ●: [*n*Bu$_4$N]$^+$, *) Ph_3CH, **) ferrocene.

Note: Microcrystalline **1** is only sparingly soluble in CD_2Cl_2; the solubility of the in situ re-generated **1** is significantly better, which explains the different signal-to-noise ratios in the top and bottom spectra.

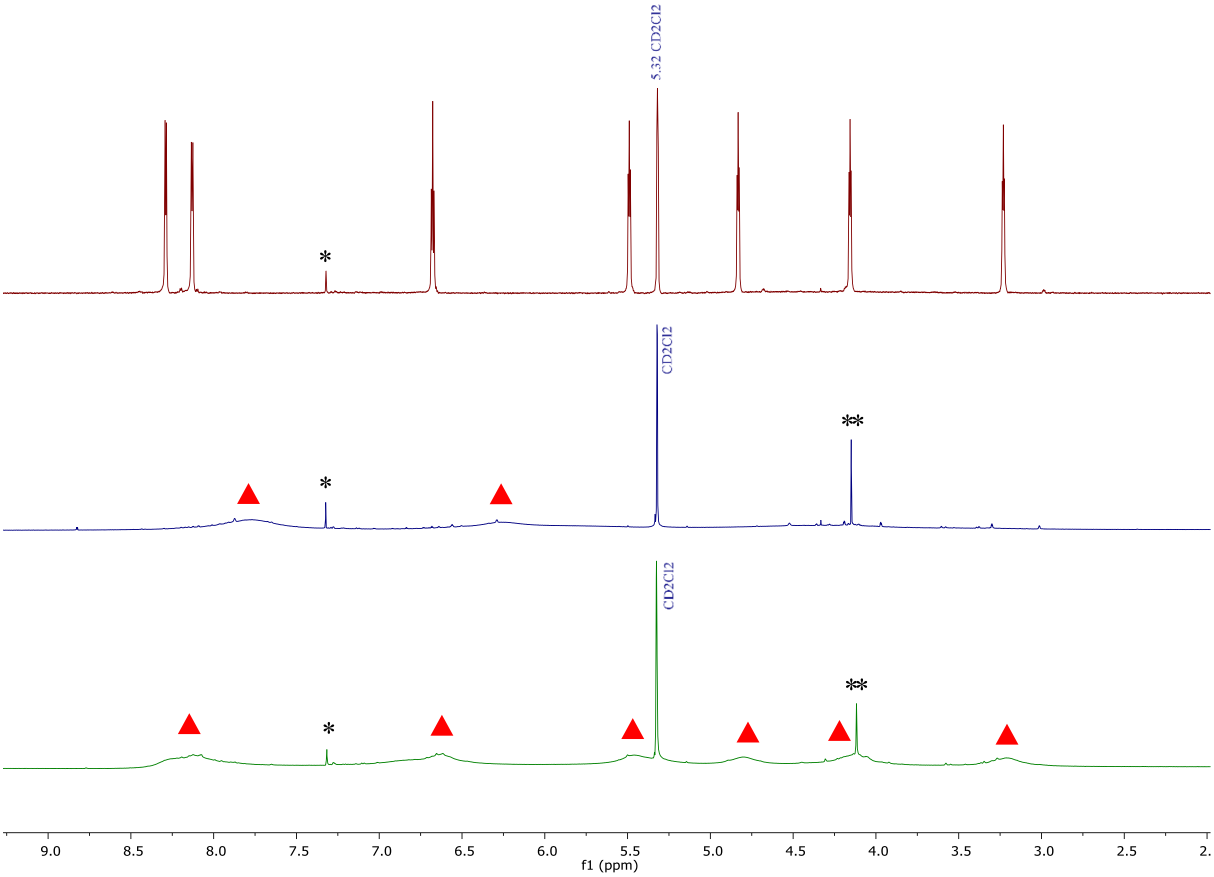

Figure S38: Top: ^{1}H NMR spectrum (CD_2Cl_2, 500.2 MHz) of a purified sample of [**2**][$B(C_6F_5)_4$] (1 eq); middle/bottom: ^{1}H NMR spectra recorded at RT/243 K on the same sample after the addition of **1** (1 eq). ▲ : Broadened signals of ferrocene-containing species. *) Trace of $CHCl_3$, **) ferrocene.

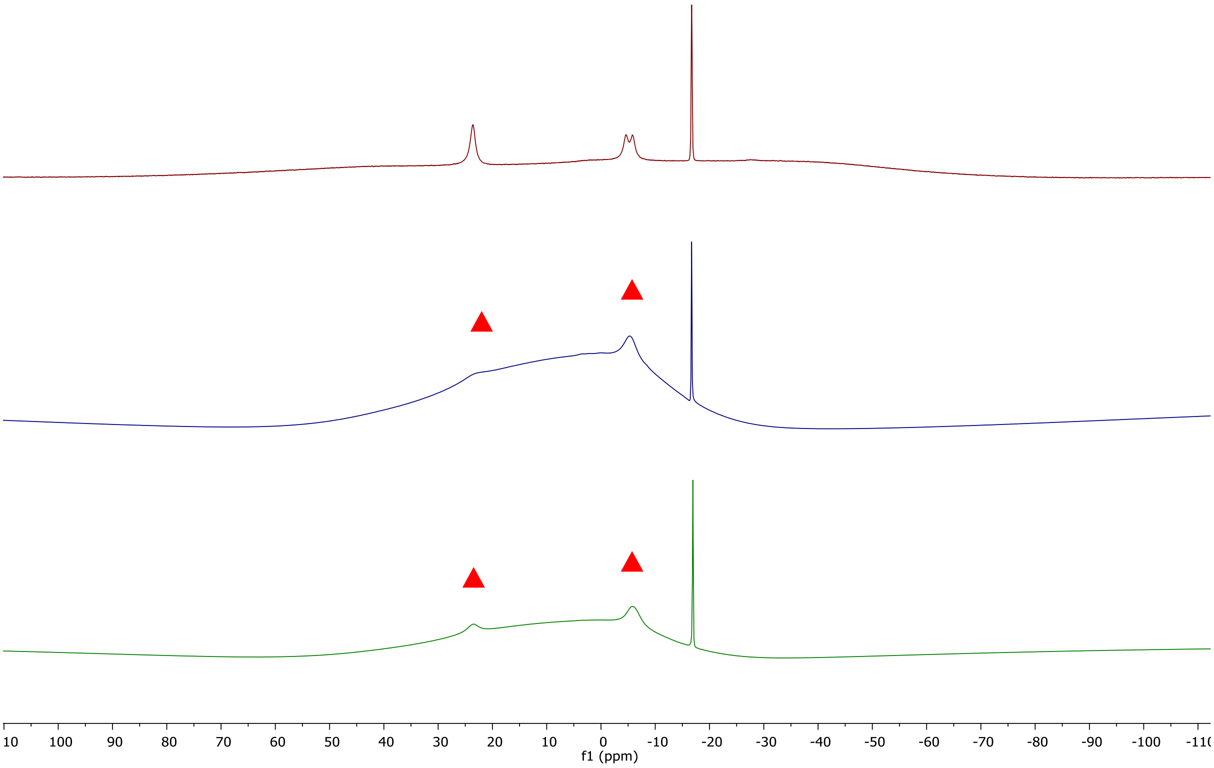

Figure S39: Top: ^{11}B NMR spectrum (CD_2Cl_2, 96.3 MHz) of a purified sample of [**2**][$B(C_6F_5)_4$] (1 eq); middle/bottom: ^{11}B NMR spectra (160.5 MHz) recorded at RT/243K on the same sample after the addition of **1** (1 eq). ▲ : Broadened signals of ferrocene-containing species.

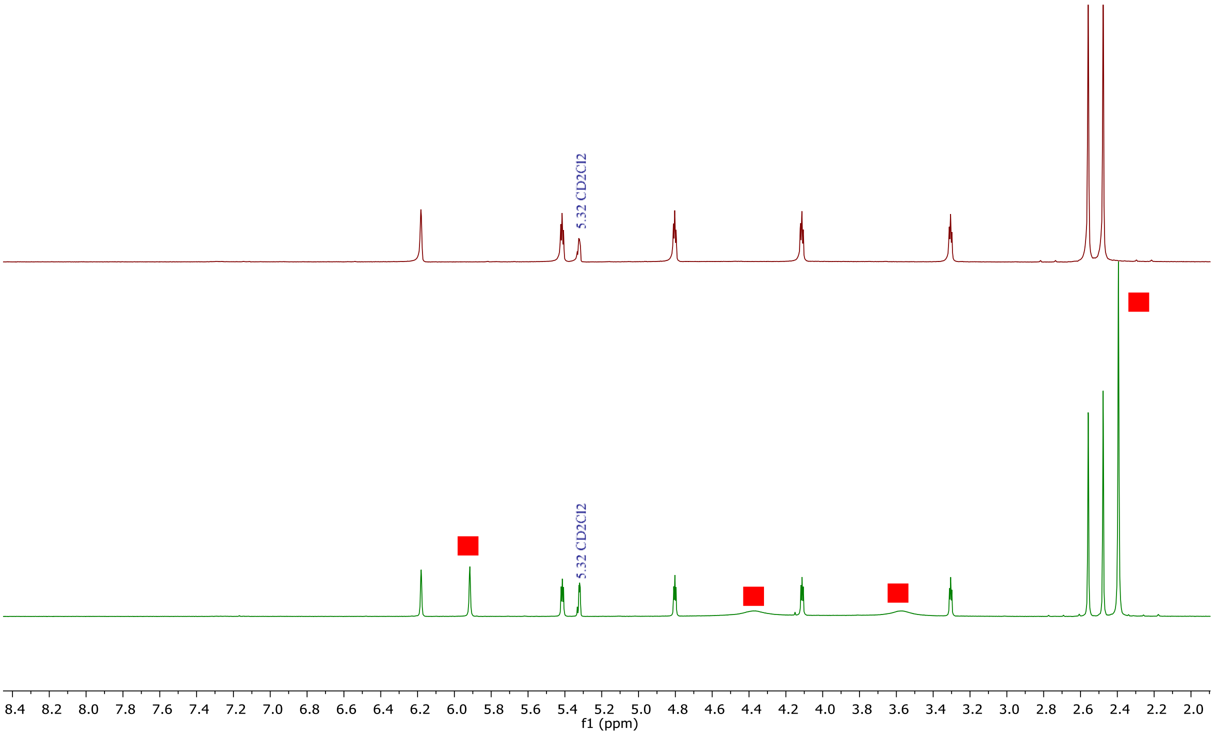

Figure S40: Top: ^{1}H NMR spectrum (CD_2Cl_2, 250.2 MHz) of a purified sample of [**2Me**][$B(C_6F_5)_4$] (1 eq); bottom: ^{1}H NMR spectrum (300.0 MHz) recorded on the same sample after the addition of **1Me** (1 eq). 🟥: Partially broadened and shifted signals of **1Me**.

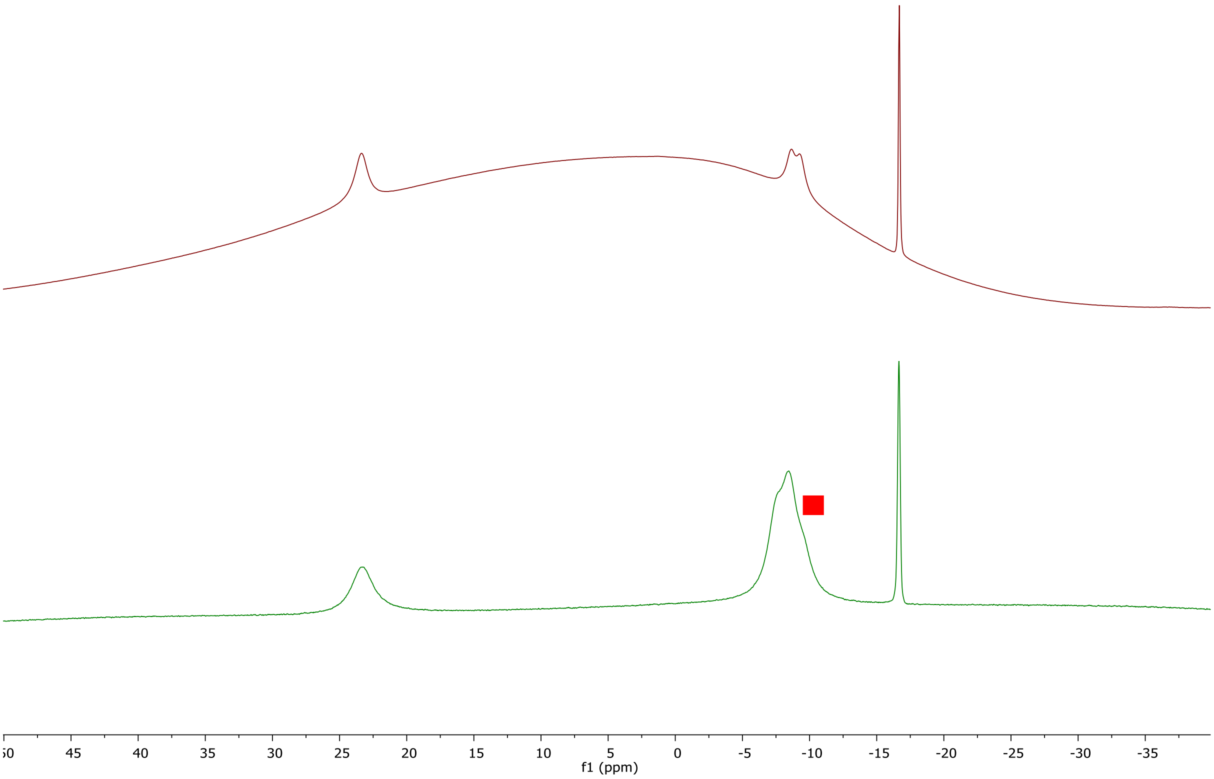

Figure S41: Top: ^{11}B NMR spectrum (CD_2Cl_2, 160.5 MHz) of a purified sample of [**2Me**][$B(C_6F_5)_4$] (1 eq); bottom: ^{11}B NMR spectrum (96.3 MHz) recorded on the same sample after the addition of **1Me** (1 eq). 🟥: Signal of **1Me**.

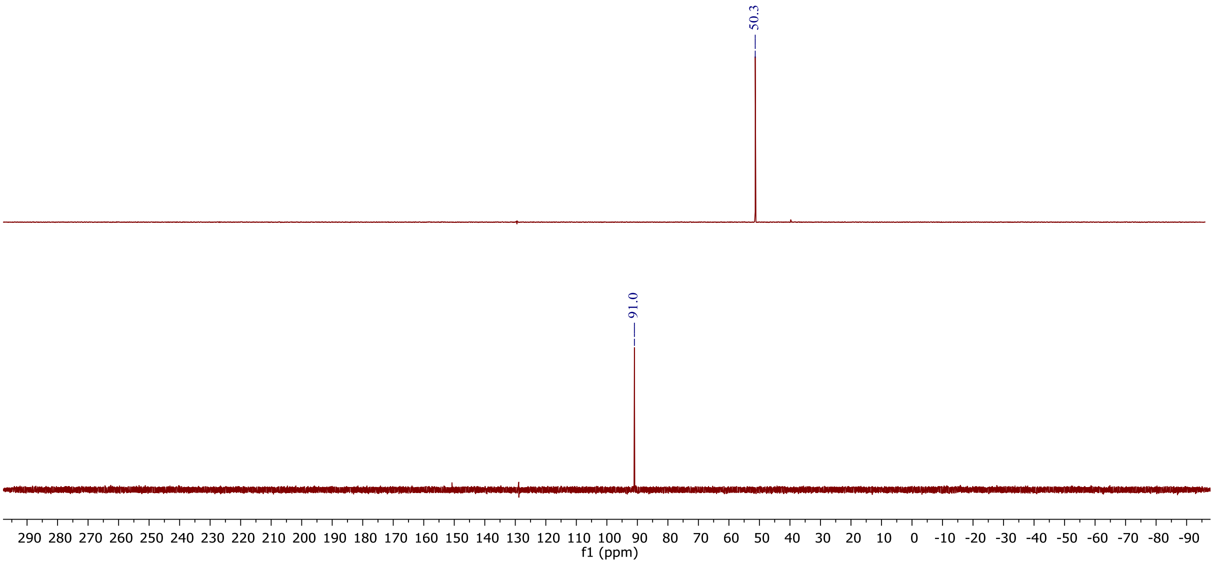

Figure S42: Gutmann-Beckett measurement according to method a): Top: $^{31}P\{^{1}H\}$ NMR spectrum (CD_2Cl_2; 162.0 MHz) of pure Et_3PO; bottom: $^{31}P\{^{1}H\}$ NMR spectrum (CD_2Cl_2; 162.0 MHz) of the reaction mixture of **1** (1 eq) / $[Ph_3C][B(C_6F_5)_4]$ (0.9 eq) / Et_3PO (0.5 eq).

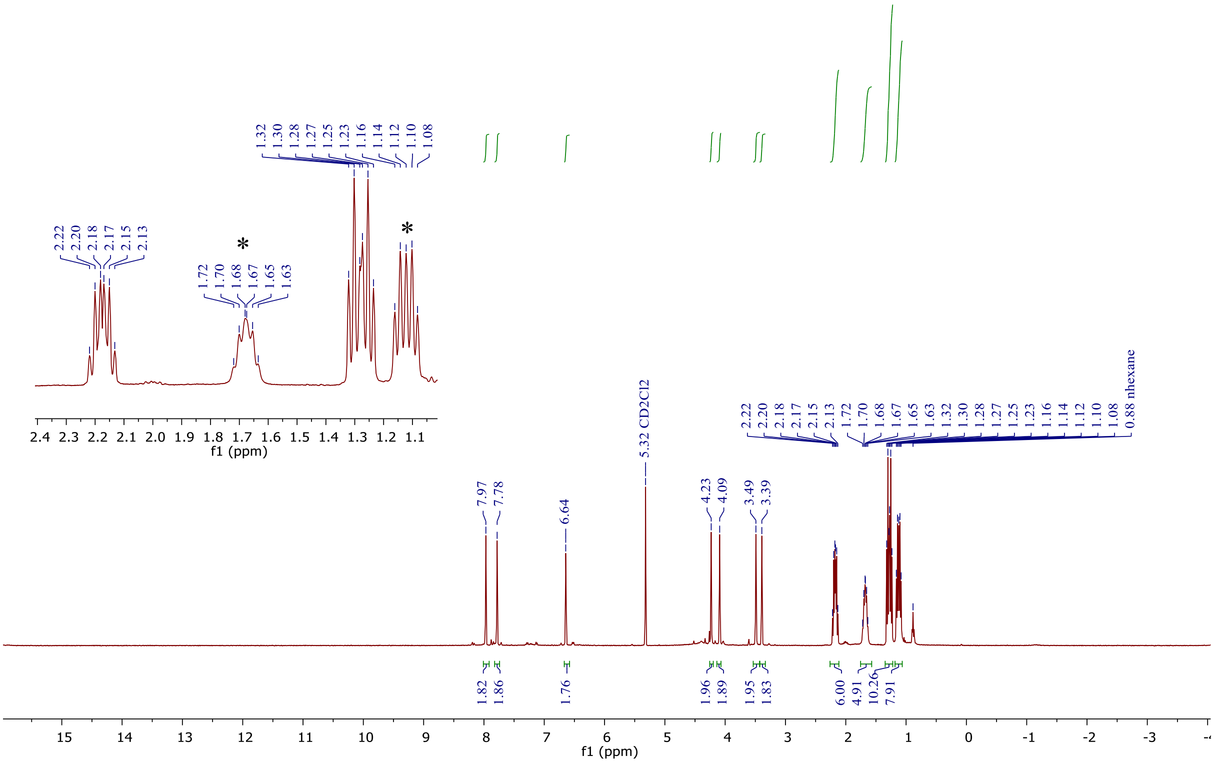

Figure S43: Gutmann-Beckett measurement according to method c): ^{1}H NMR spectrum (CD_2Cl_2; 400.1 MHz) recorded on the reaction mixture $[\mathbf{2}][B(C_6F_5)_4]$ (1 eq) / Et_3PO (1.5 eq). *) excess free Et_3PO.

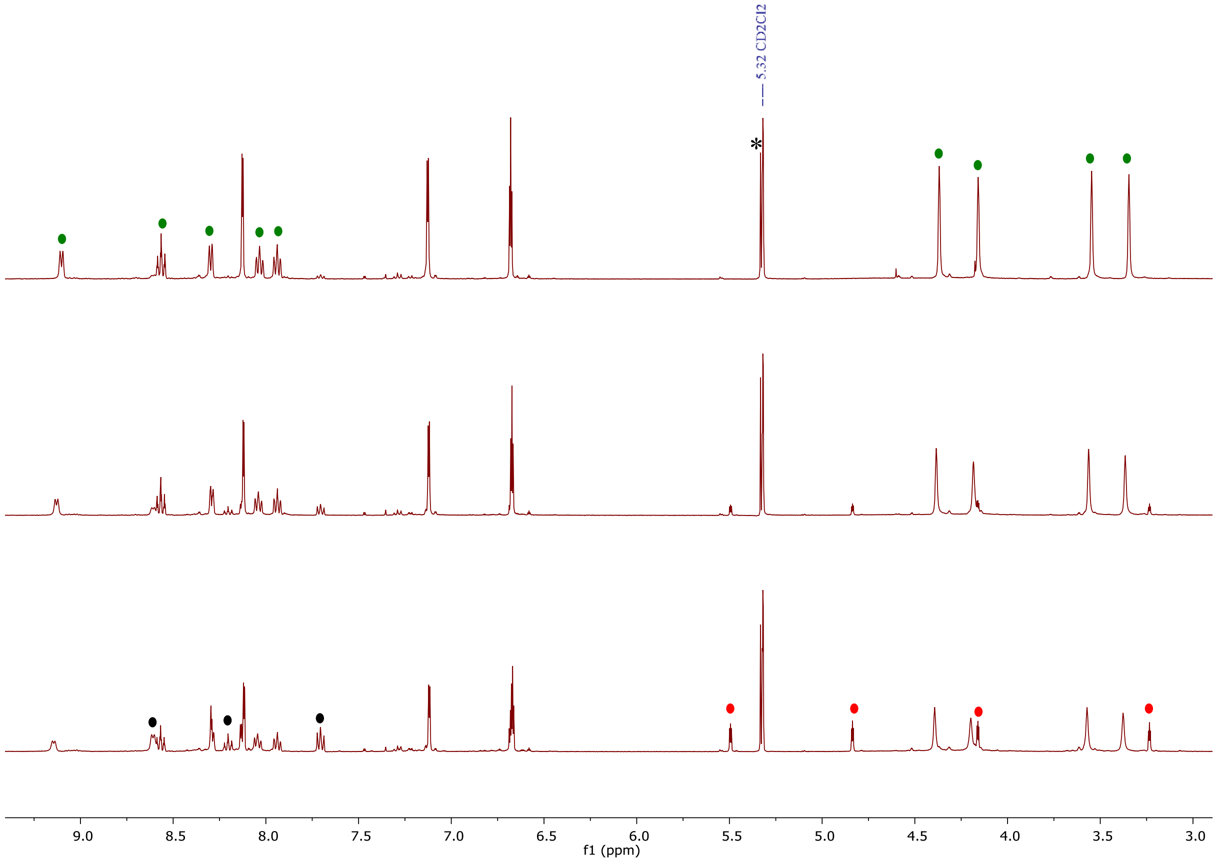

Figure S44: Competition experiment between [**2**·py][$B(C_6F_5)_4$] and free $B(C_6F_5)_3$. Top to bottom: ^{1}H NMR spectrum (CD_2Cl_2, 400.1 MHz) of an equimolar mixture of [**2**·py][$B(C_6F_5)_4$] and $B(C_6F_5)_3$ recorded 30 min / 1 d / 3 d after sample preparation (the sample was always kept at room temperature). Selected characteristic signals of the observable compounds are marked in the following way: 🟢: [**2**·py][$B(C_6F_5)_4$]; ●: $B(C_6F_5)_3$·py; 🔴: [**2**][$B(C_6F_5)_4$]. *) CH_2Cl_2.

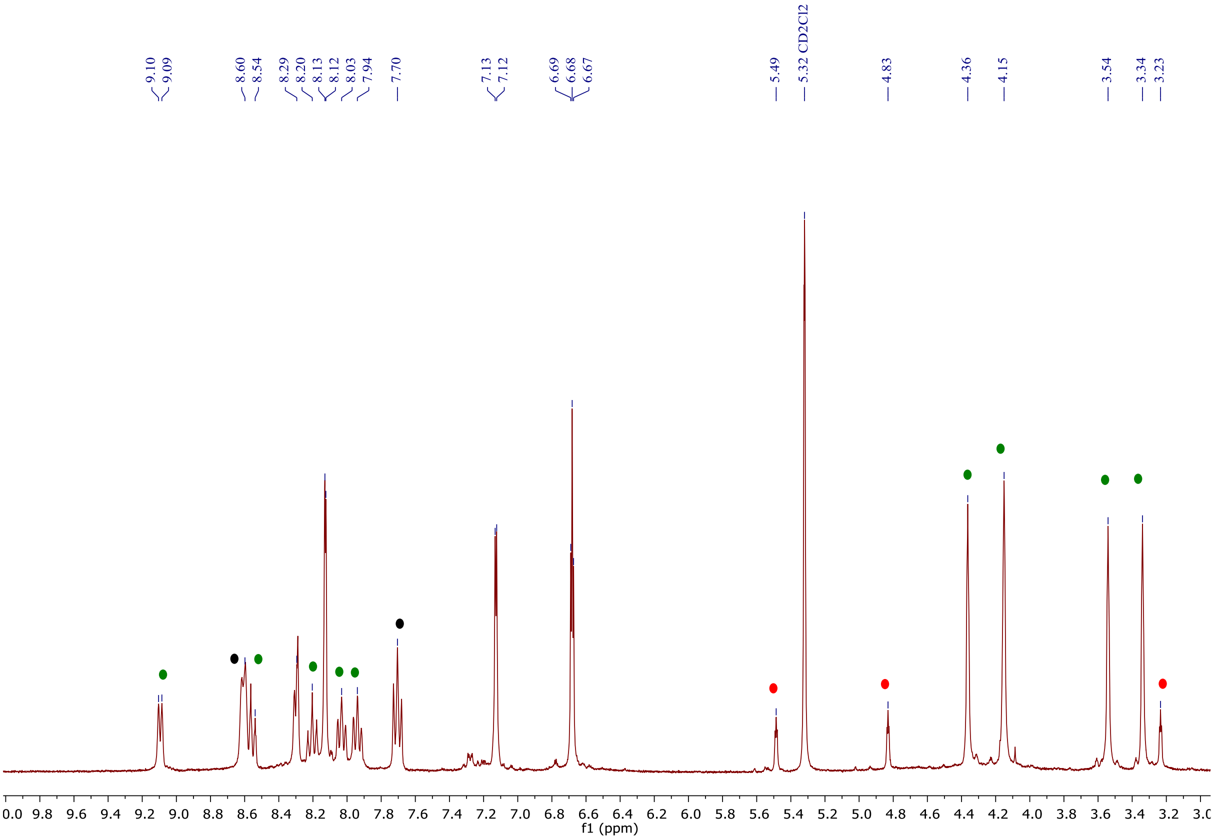

Figure S45: Competition experiment between $B(C_6F_5)_3 \cdot py$ and free [**2**][$B(C_6F_5)_4$]. ^1H NMR spectrum (CD_2Cl_2, 300.0 MHz) of an equimolar mixture of $B(C_6F_5)_3 \cdot py$ and [**2**][$B(C_6F_5)_4$] recorded 6 h after sample preparation (the sample was always kept at room temperature). Selected characteristic signals of the observable compounds are marked in the following way: 🟢: [**2**·py][$B(C_6F_5)_4$]; ●: $B(C_6F_5)_3 \cdot py$; 🔴: [**2**][$B(C_6F_5)_4$].

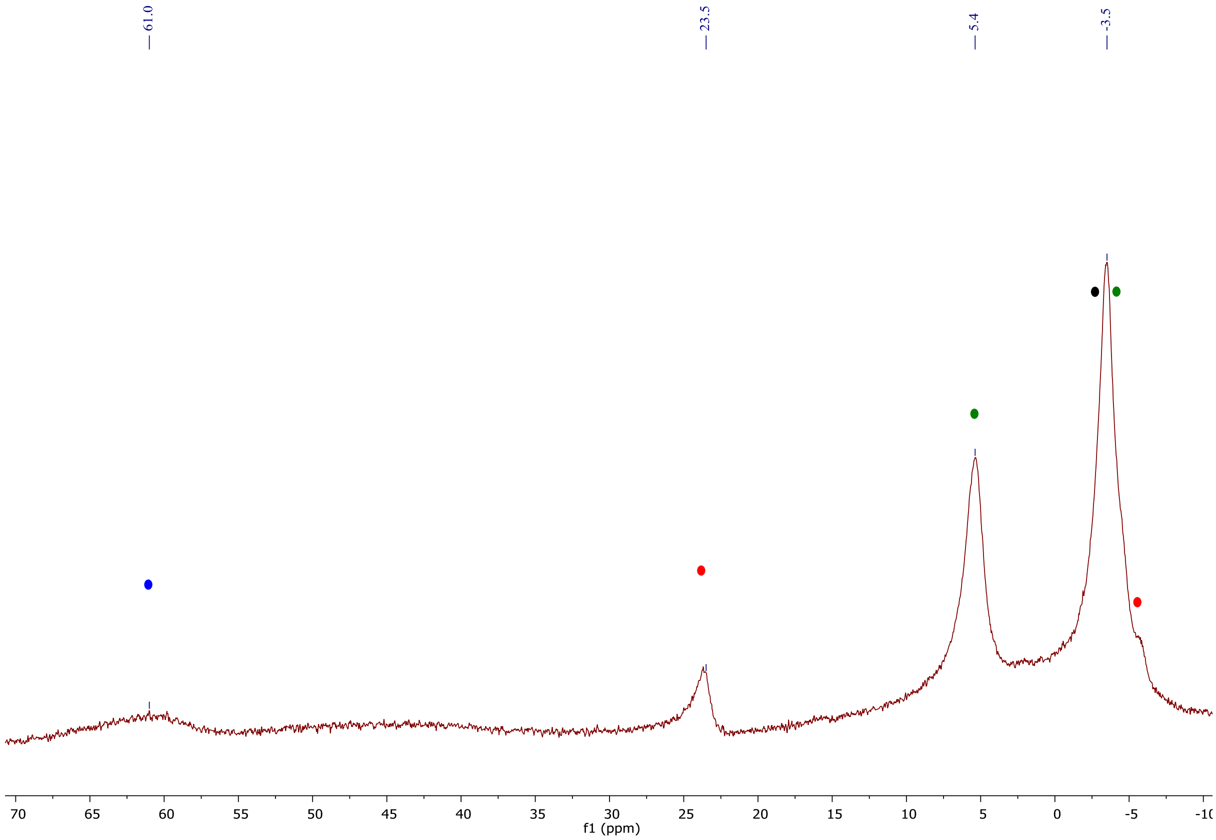

Figure S46: Competition experiment between $B(C_6F_5)_3{\cdot}py$ and free [**2**][$B(C_6F_5)_4$]. ^{11}B NMR spectrum (CD_2Cl_2, 96.3 MHz) of an equimolar mixture of $B(C_6F_5)_3{\cdot}py$ and [**2**][$B(C_6F_5)_4$] recorded 6 h after sample preparation (the sample was always kept at room temperature). ●: $B(C_6F_5)_3$; ●: [**2**][$B(C_6F_5)_4$]; ●: [**2**·py][$B(C_6F_5)_4$]; ●: $B(C_6F_5)_3{\cdot}py$.

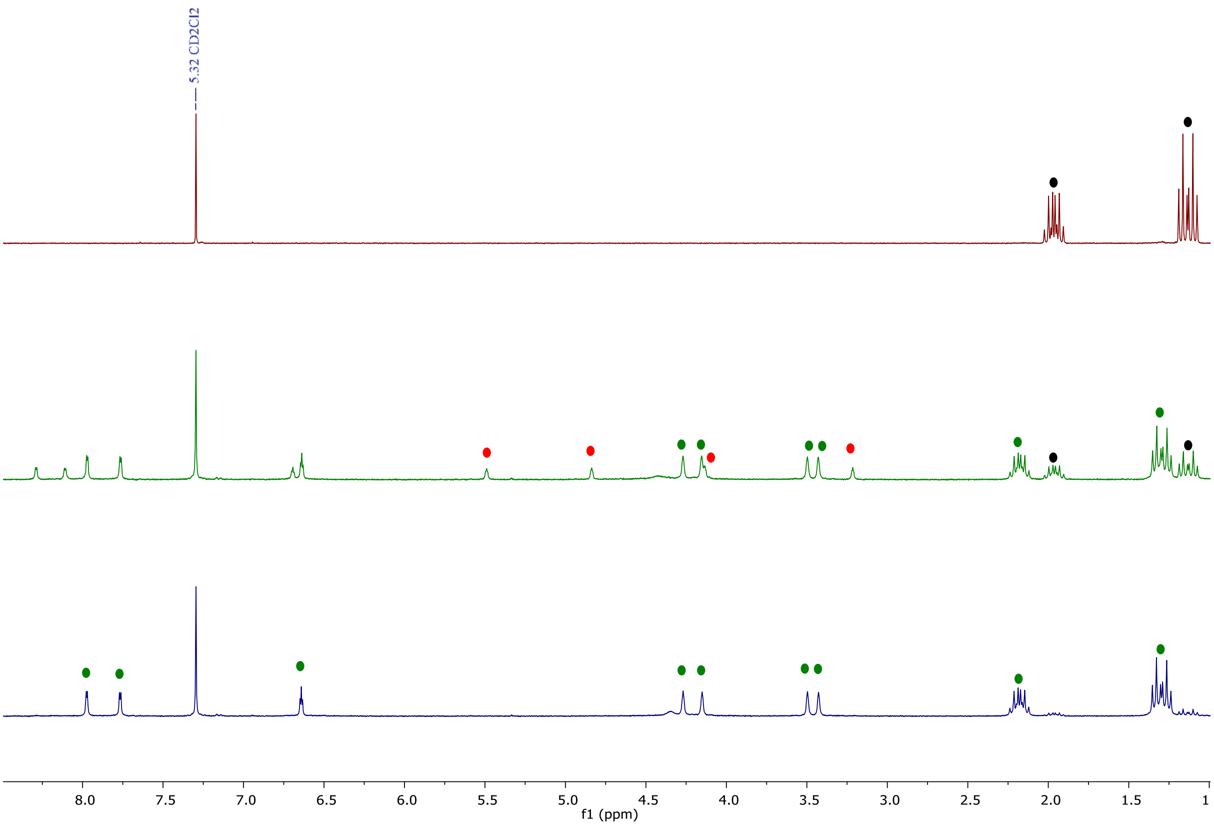

Figure S47: Competition experiment between $B(C_6F_5)_3{\cdot}OPEt_3$ and free [**2**][$B(C_6F_5)_4$]. Top: ^1H NMR spectrum (CD_2Cl_2, 300.2 MHz) of pure $B(C_6F_5)_3{\cdot}OPEt_3$. Middle/bottom: ^1H NMR spectrum (CD_2Cl_2, 300.2 MHz) of the same sample 30 min/16 h after the addition of [**2**][$B(C_6F_5)_4$] (1 eq; room temperature). Selected characteristic signals of the observable compounds are marked in the following way: ●: [**2**$\cdot$OPEt$_3$][$B(C_6F_5)_4$]; ●: $B(C_6F_5)_3{\cdot}OPEt_3$; ●: [**2**][$B(C_6F_5)_4$].

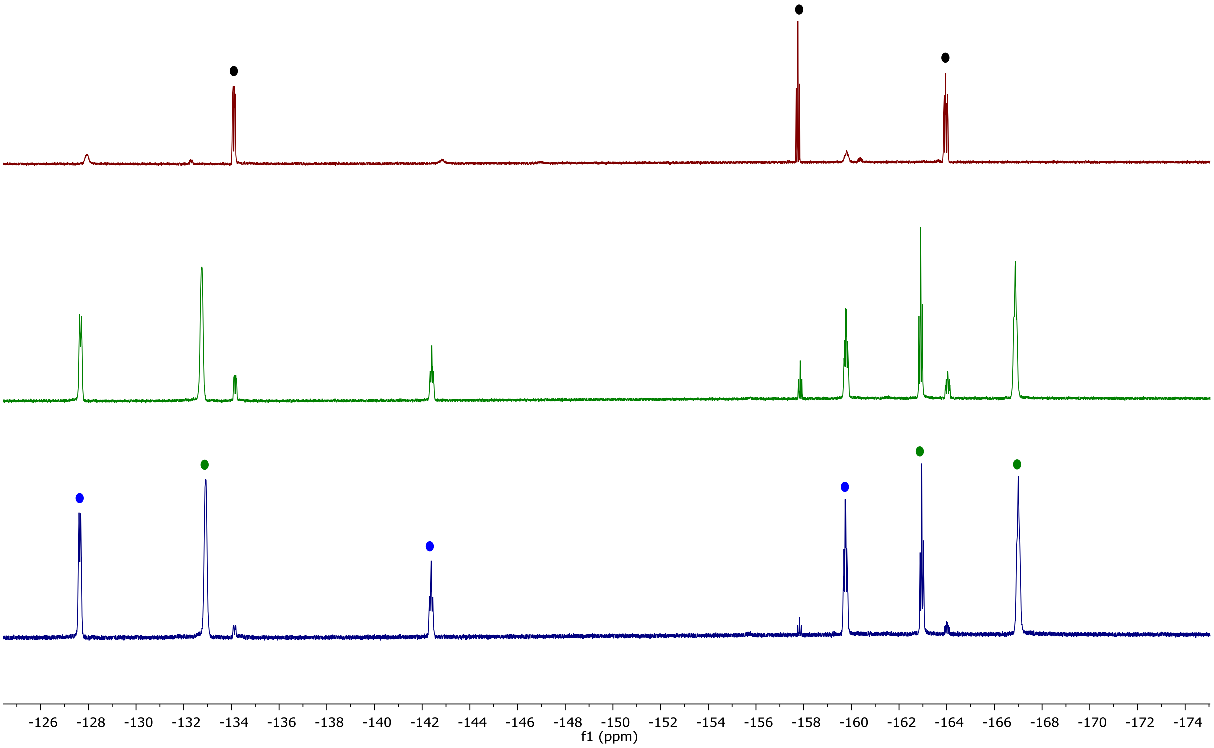

Figure S48: Competition experiment between $B(C_6F_5)_3 \cdot OPEt_3$ and free [**2**][$B(C_6F_5)_4$]. Top: ^{19}F NMR spectrum (CD_2Cl_2, 282.3 MHz) of pure $B(C_6F_5)_3 \cdot OPEt_3$. Middle/bottom: ^{19}F NMR spectrum (CD_2Cl_2, 282.3 MHz) of the same sample 30 min/16 h after the addition of [**2**][$B(C_6F_5)_4$] (1 eq; room temperature). ●: $B(C_6F_5)_3 \cdot OPEt_3$; ●: $[B(C_6F_5)_4]^-$; ●: $B(C_6F_5)_3$.

4. Cyclic voltammograms of compounds 1 and 1Me

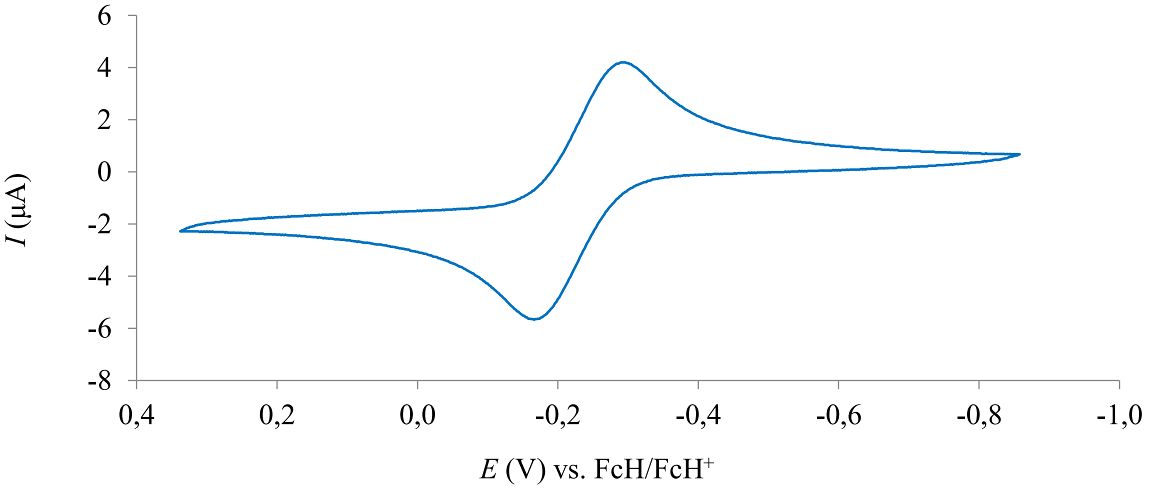

Figure S49: Cyclic voltammogram of **1** in CH_2Cl_2 (room temperature, supporting electrolyte: $[n\mathrm{Bu}_4\mathrm{N}][\mathrm{PF}_6]$ (0.1 M), scan rate: 200 mV s^{-1}).

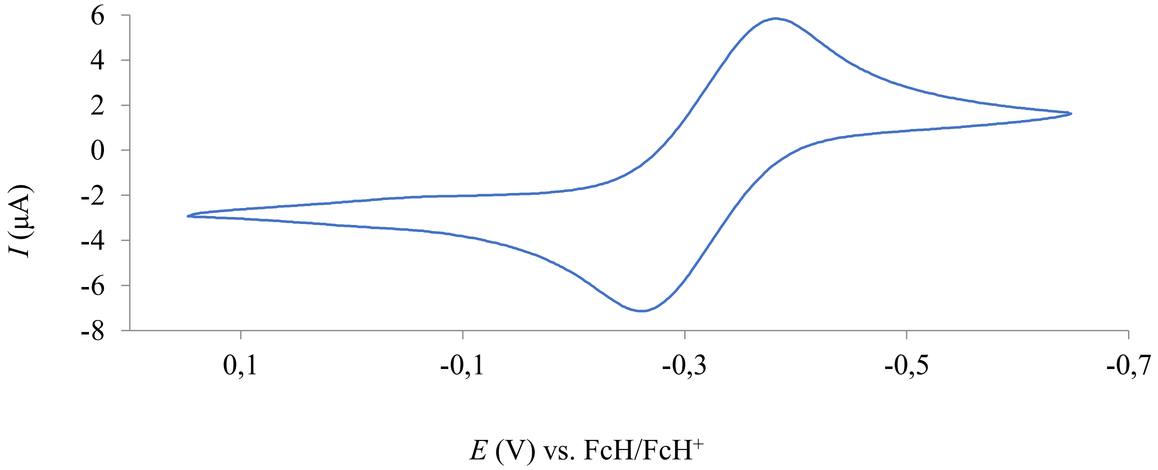

Figure S50: Cyclic voltammogram of **1Me** in CH_2Cl_2 (room temperature, supporting electrolyte: $[n\mathrm{Bu}_4\mathrm{N}][\mathrm{PF}_6]$ (0.1 M), scan rate: 200 mV s^{-1}).

5. ^{57}Fe Mößbauer spectra of 1 and [2][B(C_6F_5)$_4$]

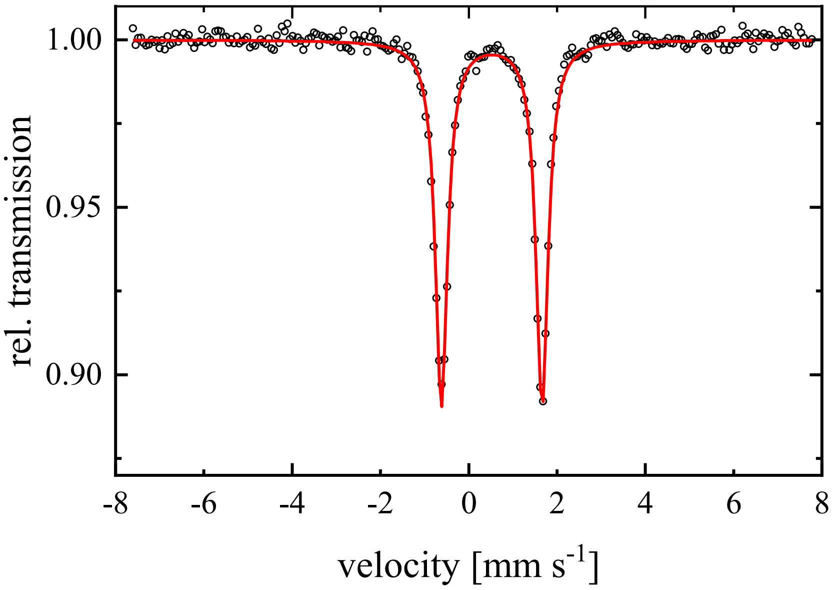

Figure S51: ^{57}Fe Mößbauer spectrum of **1** at 77 K. The red line was fitted through a least square analysis with the parameters given in Table S1.

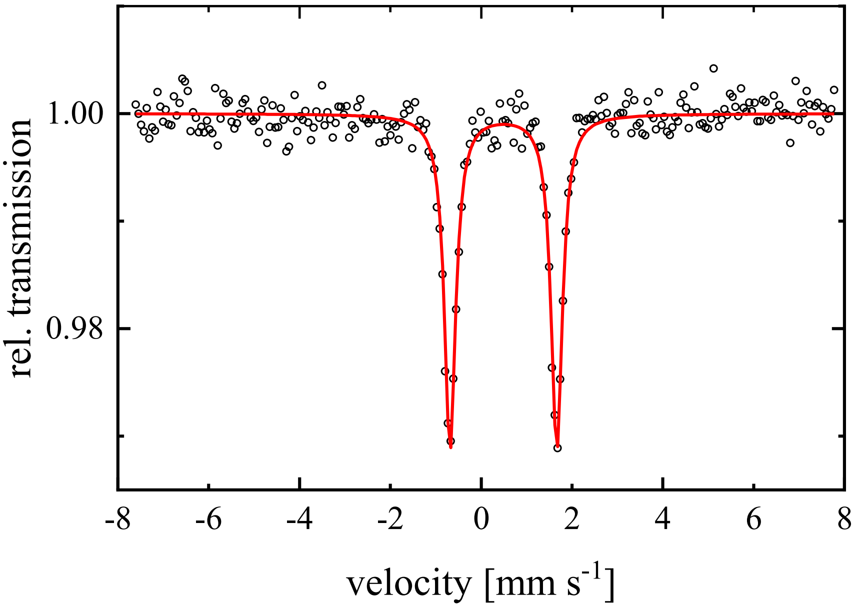

Figure S52: ^{57}Fe Mößbauer spectrum of [**2**][B(C_6F_5)$_4$] at 77 K. The red line was fitted through a least square analysis with the parameters given in Table S1.

Table S1: Parameters of measured ^{57}Fe Mössbauer spectra at 77K.

sample	δ (mm s^{-1})	ΔE_Q (mm s^{-1})	Γ (mm s^{-1})
1	0.52(1)	2.28(2)	0.33(1)
[**2**][B(C_6F_5)$_4$]	0.49(1)	2.35(2)	0.30(1)

6. UV-vis spectra of 1, [2][B(C_6F_5)$_4$], 1Me, and [2Me][B(C_6F_5)$_4$]

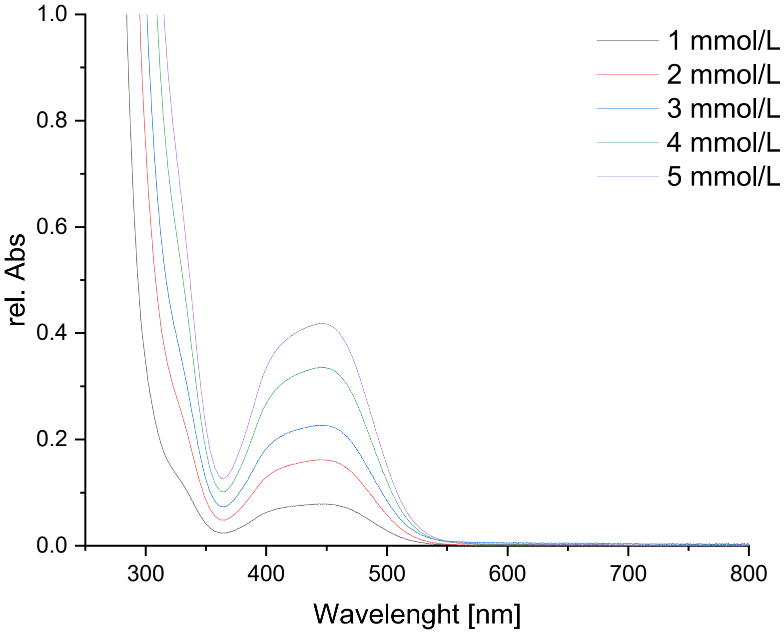

Figure S53: UV-vis absorption spectra of **1** at different concentrations (CH_2Cl_2). The calculated extinction coefficient is $\varepsilon_{(\lambda=444nm)} = 8$ m² mol⁻¹.

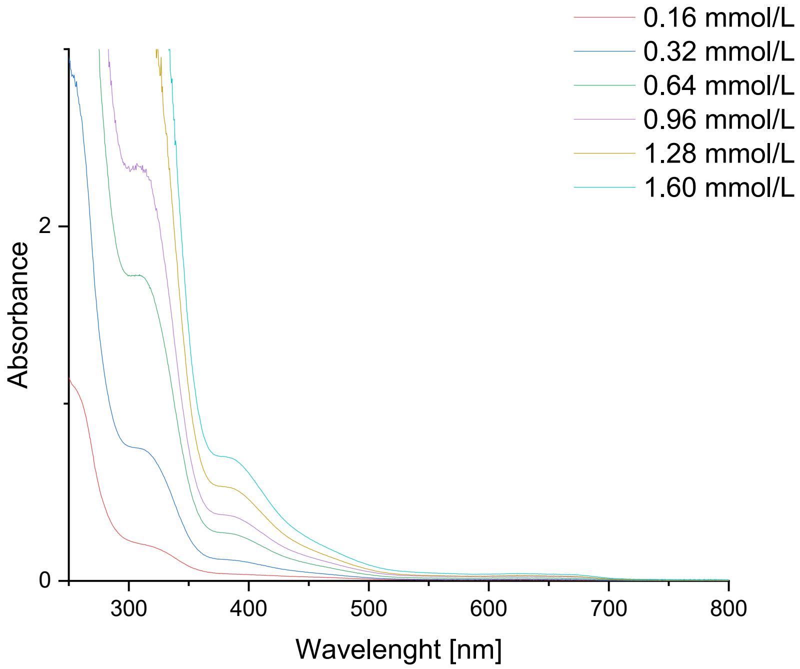

Figure S54: UV-vis absorption spectra of [**2**][B(C_6F_5)$_4$] at different concentrations (CH_2Cl_2). The calculated extinction coefficients are $\varepsilon_{(\lambda=378nm)} = 38$ m² mol⁻¹ and $\varepsilon_{(\lambda=309nm)} = 232$ m² mol⁻¹.

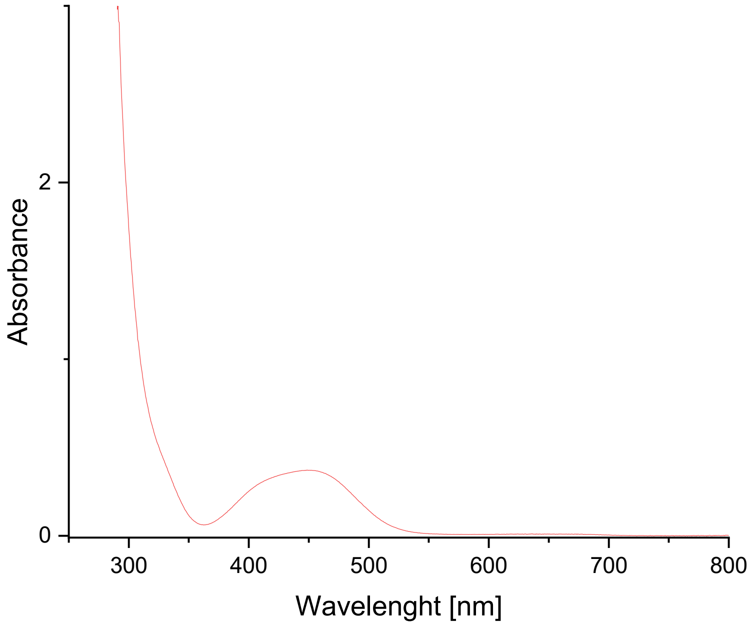

Figure S55: UV-vis absorption spectrum of **1Me** (CH_2Cl_2).

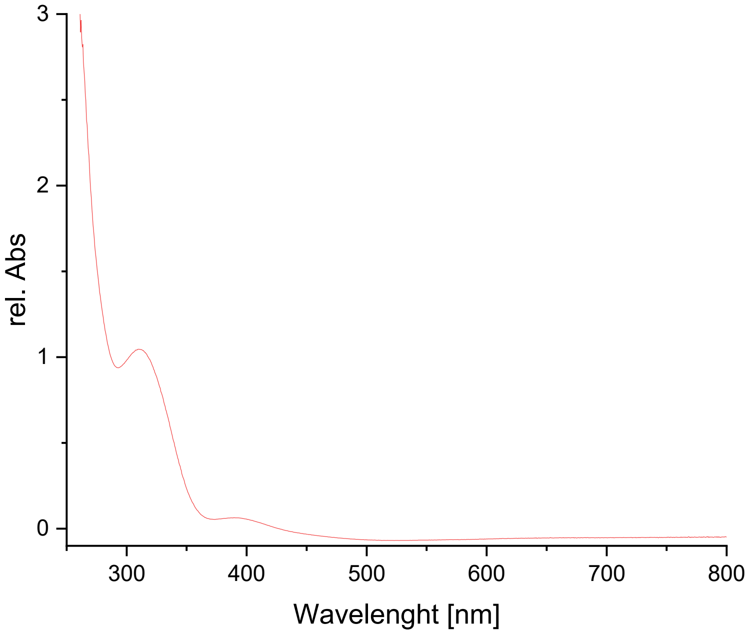

Figure S56: UV-vis absorption spectrum of [**2Me**][$B(C_6F_5)_4$ (CH_2Cl_2).

7. X-ray crystal structure determinations

Data for all structures were collected on a STOE IPDS II two-circle diffractometer with a Genix Microfocus tube with mirror optics using MoK$_\alpha$ radiation (λ = 0.71073 Å). The data were scaled using the frame-scaling procedure in the *X-AREA* program system.[ES7]The structures were solved by direct methods using the program *SHELXS* and refined against F^2 with full-matrix least-squares techniques using the program *SHELXL*.[ES8]

Structure	Internal code	CCDC reference number
1	wa2798	2120063
1Me	wa2957	2120064
[**2**][B(C_6F_5)$_4$)]	wa2927	2120065
[**2Me**][B(C_6F_5)$_4$)]	wa3022	2120066
[**2**·py][B(C_6F_5)$_4$)]	wa2924	2120067

Specific comments regarding the individual crystal structure analyses:

Compound **1**: The H atoms bonded to B were isotropically refined.

Compound **1Me**: The H atoms bonded to B were isotropically refined.

Compound [**2**][B(C_6F_5)$_4$)]: The compound crystallizes with three molecules in the asymmetric unit. The crystal was a racemic twin with a fractional contribution of 0.55(2) for the major domain. The H atoms bonded to B were isotropically refined.

Compound [**2Me**][B(C_6F_5)$_4$)]: The contribution of the solvent was suppressed by using the *SQUEEZE* routine in *PLATON*.[ES9] The H atom bonded to B was isotropically refined.

Compound [**2**·py][B(C_6F_5)$_4$)]: The H atom bonded to B was isotropically refined.

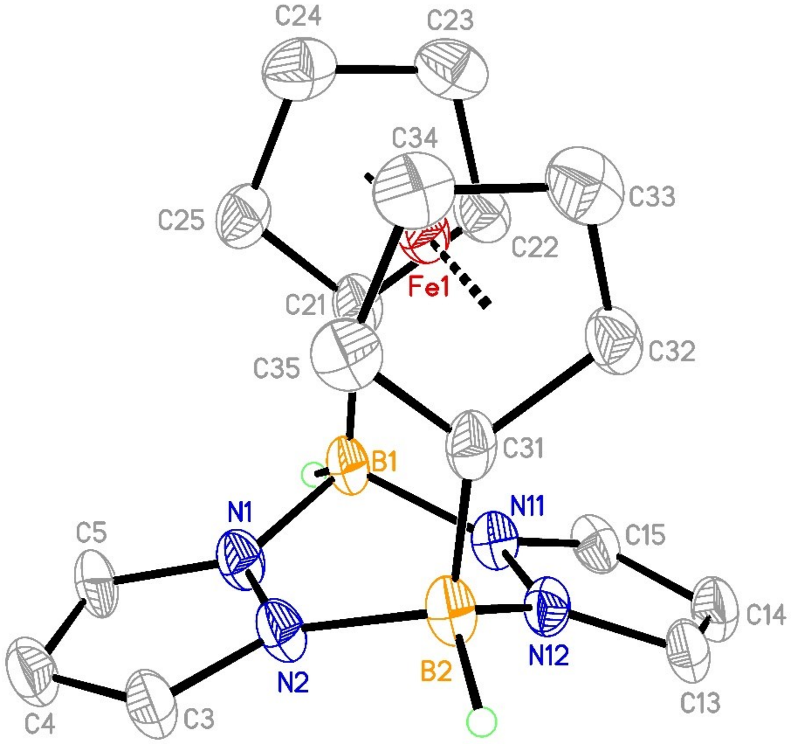

Figure S57: Molecular structure of **1** in the solid state; H atoms bonded to C atoms are omitted for clarity. Displacement ellipsoids are drawn at the 50% probability level. Selected bond lengths [Å], bond angles [°], and dihedral angles [°]: B(1)–N(1) = 1.566(6), B(1)–N(11) = 1.562(6), B(1)–C(21) = 1.584(7), B(2)–N(2) = 1.564(6), B(2)–N(12) = 1.570(6), B(2)–C(31) = 1.578(7); N(1)–B(1)–N(11) = 105.0(3), N(1)–B(1)–C(21) = 110.7(4), N(11)–B(1)–C(21) = 110.2(3), N(2)–B(2)–N(12) = 104.4(3), N(2)–B(2)–C(31) = 110.9(4), N(12)–B(2)–C(31) = 110.4(4), B(1)N(1)N(11)// N(1)N(2)N(11)N(12) = 31.0(3), B(2)N(2)N(12)//N(1)N(2)N(11)N(12) = 31.5(3), Cp(C(21))// Cp(C(31)) = 3.3(3), pz(N(1))//pz(N(11)) = 148.77(14). Cp(C(X))/pz(N(X)): cyclopentadienyl/pyrazolyl ring containing C(X)/N(X).

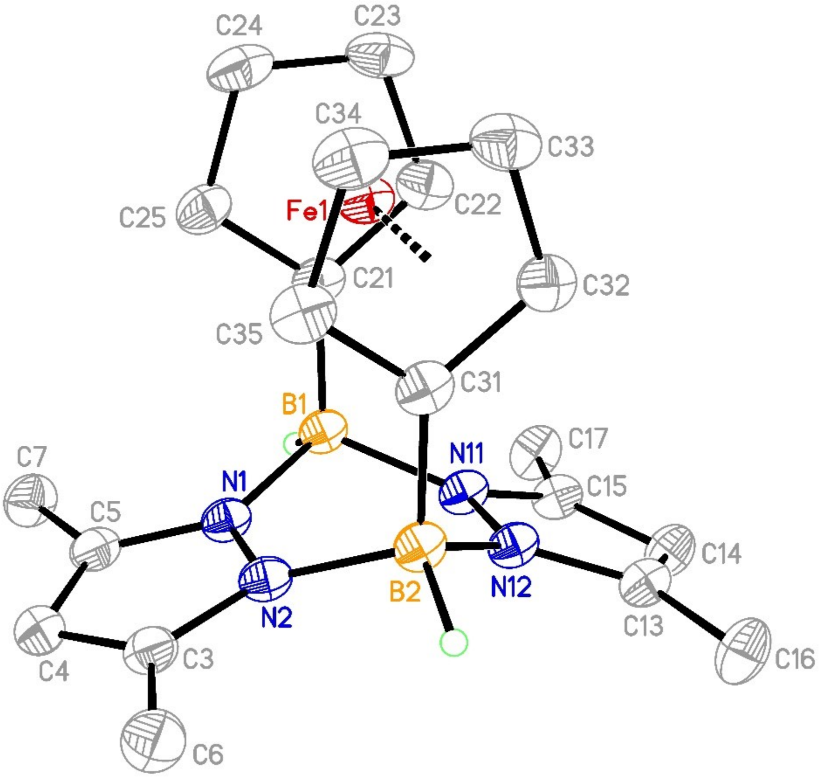

Figure S58: Molecular structure of **1Me** in the solid state; H atoms bonded to C atoms are omitted for clarity. Displacement ellipsoids are drawn at the 50% probability level. Selected bond lengths [Å], bond angles [°], and dihedral angles [°]: B(1)–N(1) = 1.568(2), B(1)–N(11) = 1.565(2), B(1)–C(21) = 1.593(3), B(2)–N(2) = 1.570(2), B(2)–N(12) = 1.562(2), B(2)–C(31) = 1.598(3); N(1)–B(1)–N(11) = 105.82(13), N(1)–B(1)–C(21) = 109.66(14), N(11)–B(1)–C(21) = 111.37(15), N(2)–B(2)–N(12) = 105.68(14), N(2)–B(2)–C(31) = 110.30(14), N(12)–B(2)–C(31) = 110.80(14), COG–Cp(C(21))–B(1) = 178.4; B(1)N(1)N(11)//N(1)N(2)N(11)N(12) = 30.87(12), B(2)N(2)N(12)//N(1)N(2)N(11)N(12) = 32.63(14), Cp(C(21))//Cp(C(31)) = 5.15(13), pz(N(1))//pz(N(11)) = 146.80(9). Cp(C(X))/pz(N(X)): cyclopentadienyl/pyrazolyl ring containing C(X)/N(X); COG: cyclopentadienyl-ring centroid

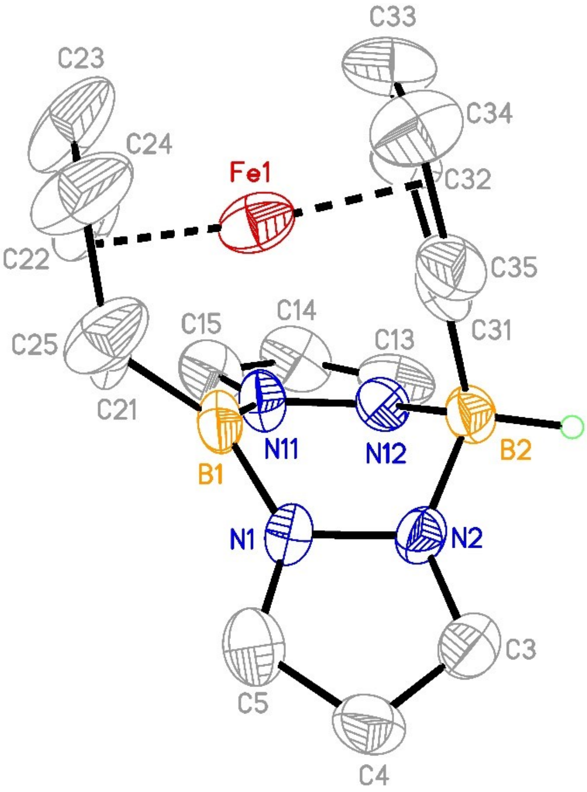

Figure S59: Molecular structure of [**2**][B(C_6F_5)$_4$)] in the solid state; the [B(C_6F_5)$_4$)]$^-$ anion and H atoms bonded to C atoms are omitted for clarity. Displacement ellipsoids are drawn at the 50% probability level. The crystal lattice contains three crystallographically independent ion pairs in the asymmetric unit. Selected bond lengths [Å], bond angles [°], and dihedral angles [°]: Fe(1)–B(1) = 2.372(13) [2.391(13), 2.367(13)], B(1)–N(1) = 1.481(15) [1.482(15), 1.537(16)], B(1)–N(11) = 1.492(15) [1.527(16), 1.470(16)], B(1)–C(21) = 1.487(17) [1.445(17), 1.465(17)], B(2)–N(2) = 1.557(14) [1.552(15), 1.532(15)], B(2)–N(12) = 1.551(15) [1.544(15), 1.547(16)], B(2)–C(31) = 1.600(17) [1.636(18), 1.625(16)]; N(1)–B(1)–N(11) = 111.5(9) [108.8(10), 110.2(10)], N(1)–B(1)–C(21) = 123.3(11) [126.9(11), 124.4(11)], N(11)–B(1)–C(21) = 125.0(11) [124.1(11), 125.1(11)], N(2)–B(2)–N(12) = 104.0(8) [105.3(9), 104.0(9)], N(2)–B(2)–C(31) = 107.1(9) [105.5(9), 105.9(9)], N(12)–B(2) – C(31) = 106.0(9) [106.9(9), 106.9(9)], COG–C(21)–B(1) = 138.7 [141.9, 138.7]; Cp(C(21))//Cp(C(31)) = 6.1(9) [5.0(5), 4.7(7)], pz(N(1))//pz(N(11)) = 135.7(4) [140.1(4), 137.0(5)]. Cp(C(X))/pz(N(X)): cyclopentadienyl/pyrazolyl ring containing C(X)/N(X); COG: cyclopentadienyl-ring centroid.

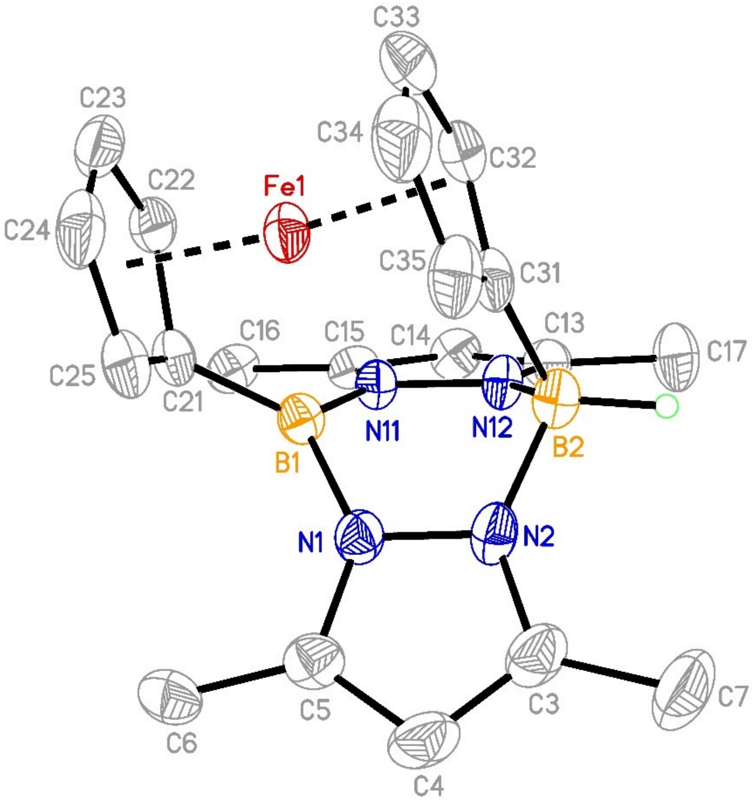

Figure S60: Molecular structure of [**2Me**][B(C_6F_5)$_4$)] in the solid state; the [B(C_6F_5)$_4$)]$^-$ anion and H atoms bonded to C atoms are omitted for clarity. Displacement ellipsoids are drawn at the 50% probability level. Selected bond lengths [Å], bond angles [°], torsion angles [°], and dihedral angles [°]: Fe(1)–B(1) = 2.365(4), B(1)–N(1) = 1.506(5), B(1)–N(11) = 1.505(5), B(1)–C(21) = 1.497(6), B(2)–N(2) = 1.569(6), B(2)–N(12) = 1.566(6), B(2) –C(31) = 1.613(6); N(1)–B(1)–N(11) = 110.4(3), N(1)–B(1)–C(21) = 123.9(4), N(11)–B(1)–C(21) = 125.4(4), N(2)–B(2)–N(12) = 102.8(3), N(2)–B(2)–C(31) = 108.3(3), N(12)–B(2)–C(31) = 106.9(3), COG–C(21)–B(1) = 139.4; B(1)N(1)N(11)//N(1)N(2)N(11)N(12) = 40.7(3), B(2)N(2)N(12)// N(1)N(2)N(11)N(12) = 49.1(2), Cp(C(21))//Cp(C(31)) = 5.35(11), pz(N(1))//pz(N(11)) = 118.65(18). Cp(C(X))/pz(N(X)): cyclopentadienyl/pyrazolyl ring containing C(X)/N(X); COG: cyclopentadienyl-ring centroid.

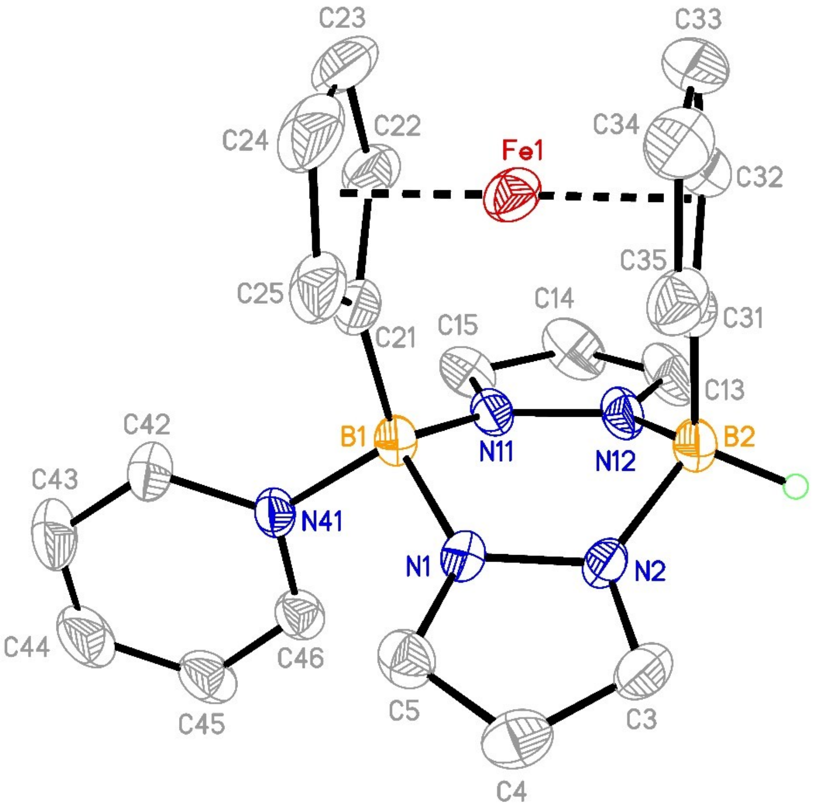

Figure S61: Molecular structure of [**2**·py][B(C_6F_5)$_4$)] in the solid state; the [B(C_6F_5)$_4$)]$^-$ anion and H atoms bonded to C atoms are omitted for clarity. Displacement ellipsoids are drawn at the 50% probability level. Selected bond lengths [Å], bond angles [°], and dihedral angles [°]: B(1)–N(1) = 1.562(3), B(1)–N(11) = 1.553(4), B(1)–N(41) = 1.603(3), B(1)–C(21) = 1.567(4), B(2)–N(2) = 1.557(4), B(2)–N(12) = 1.571(4), B(2)–C(31) = 1.597(4); N(1)–B(1)-N(11) = 106.8(2), N(1)–B(1)–N(41) = 104.18(19), N(11)–B(1)–N(41) = 105.0(2), N(1)–B(1)–C(21) = 112.9(2), N(11)–B(1)–C(21) = 112.2(2), N(41)–B(1)–C(21) = 115.0(2), N(2)–B(2)–N(12) = 104.1(2), N(2)–B(2)–C(31) = 108.3(2), N(12)–B(2)–C(31) = 110.8(2); B(1)N(1)N(11)//N(1)N(2)N(11)N(12) = 29.19(17), B(2)N(2)N(12)//N(1)N(2)N(11)N(12) = 33.9(2), Cp(C(21))//Cp(C(31)) = 1.8(2), pz(N(1))//pz(N(11)) = 27.10(12). Cp(C(X))/pz(N(X)): cyclopentadienyl/pyrazolyl ring containing C(X)/N(X).

Table S2. Selected crystallographic data for **1** and **1Me**.

Compound	**1**	**1Me**
identification code	wa2798	wa2957
formula	$C_{16}H_{16}B_2FeN_4$	$C_{20}H_{24}B_2FeN_4$
fw	341.80	397.90
T [K]	173(2)	173(2)
radiation (MoK$_\alpha$), λ [Å]	0.71073	0.71073
crystal system	triclinic	triclinic
space group	*P*-1	*P*-1
a [Å]	7.5278(8)	8.7000(5)
b [Å]	8.0007(9)	9.4404(5)
c [Å]	12.8810(14)	13.0630(7)
α [°]	98.677(9)	99.602(4)
β [°]	90.081(8)	102.526(4)
γ [°]	106.197(8)	112.399(4)
V [Å^3]	735.70(14)	930.61(9)
Z	2	2
D_{calcd}(g cm^{-3})	1.543	1.420
μ [mm^{-1}]	1.026	0.822
F(000)	352	416
crystal size [mm]	0.290×0.220×0.140	0.270×0.250×0.240
crystal form, color	light brown block	brown block
reflections collected	5235	16925
indep. reflns.	2688	3790
R_{int}	0.0680	0.0269
data/restraints/param.	2688/0/216	3790/0/256
$R1$, $wR2$ ($I > 2\sigma(I)$)	0.0793, 0.2082	0.0338, 0.0872
$R1$, $wR2$ (all data)	0.0853, 0.2155	0.0348, 0.0879
Goodness-of-fit on F^2	1.060	1.151
largest diff peak and hole (e Å^{-3})	2.377, −1.101	0.336, -0.288

Table S3. Selected crystallographic data for [**2**][B(C_6F_5)$_4$)], [**2Me**][B(C_6F_5)$_4$)], and [**2**·py][B(C_6F_5)$_4$)].

Compound	[**2**][B(C_6F_5)$_4$)]	[**2Me**][B(C_6F_5)$_4$)]	[**2**·py][B(C_6F_5)$_4$)]
Identification code	wa2927	wa3022	wa2924
formula	$C_{40}H_{15}B_3F_{20}FeN_4$	$C_{44}H_{23}B_3F_{20}FeN_4$	$C_{45}H_{20}B_3F_{20}FeN_5$
fw	1019.84	1075.94	1098.94
T [K]	173(2)	173(2)	173(2)
radiation (MoK_α), λ [Å]	0.71073	0.71073	0.71073
crystal system	monoclinic	triclinic	monoclinic
space group	*Cc*	*P*-1	$P2_1/n$
a [Å]	46.3281(16)	10.5639(4)	12.5255(4)
b [Å]	18.1515(6)	14.7558(6)	19.1507(9)
c [Å]	14.1178(5)	16.3919(7)	18.4469(6)
α [°]	90	78.271(3)	90
β [°]	105.884(3)	89.479(3)	106.913(3)
γ [°]	90	85.808(3)	90
V [Å^3]	11418.7(7)	2495.06(18)	4233.5(3)
Z	12	2	4
D_{calcd}(g cm^{-3})	1.780	1.432	1.724
μ (mm$^{-1)}$	0.535	0.412	0.488
F(000)	6048	1072	2184
crystal size [mm]	0.180×0.130×0.070	0.240×0.190×0.180	0.160×0.090×0.030
crystal form, color	orange plate	yellow block	orange plate
reflections collected	63766	25787	39589
indep. reflns.	20126	9306	7948
R_{int}	0.0533	0.0308	0.0431
data/restraints/param.	20126/2/1850	9306/0/657	7948/0/671
$R1$, $wR2$ ($I > 2\sigma(I)$)	0.0619, 0.1371	0.0699, 0.1734	0.0473, 0.0904
$R1$, $wR2$ (all data)	0.0988, 0.1589	0.0828, 0.1840	0.0640, 0.0956
Goodness-of-fit on F^2	1.039	1.189	1.145
largest diff peak and hole (e Å^{-3})	0.763, –0.460	1.619, –0.409	0.306, -0.315

8. References (experiment)

[ES1] M. Scheibitz, H. Li, J. Schnorr, A. Sánchez Perucha, M. Bolte, H.-W. Lerner, F. Jäkle and M. Wagner, *J. Am. Chem. Soc.*, 2009, **131**, 16319–16329.

[ES2] S. Budavari, M. J. O'Neil, A. Smith and P. E. Heckelman (eds.), *The Merck Index: an Encyclopedia of Chemicals, Drugs, and Biologicals* – 11th ed, Merck Co., Inc. Rathway, NJ, 1989.

[ES3] G. R. Fulmer, A. J. M. Miller, N. H. Sherden, H. E. Gottlieb, A. Nudelman, B. M. Stoltz, J. E. Bercaw and K. I. Goldberg, *Organometallics*, 2010, **29**, 2176–2179.

[ES4] H. P. Gunnlaugsson, *Hyperfine Interact.*, 2016, 237:79.

[ES5] M. Lehmann, A. Schulz and A. Villinger, *Angew. Chem. Int. Ed.*, 2009, **48**, 7444–7447.

[ES6] I. B. Sivaev and V. I. Bregadze, *Coord. Chem. Rev.*, 2014, **270-271**, 75–88.

[ES7] *Stoe & Cie., X-AREA. Diffractometer control program system*, Stoe & Cie, Darmstadt, Germany, 2002.

[ES8] G. M. Sheldrick, *Acta Crystallogr. A.*, 2008, **64**, 112–122.

[ES9] A. L. Spek, *Acta Crystallogr. Sect. D*, 2009, **65**, 148−155.

9. Computational details

The ground-state structures of all systems under investigation were optimized with the Turbomole program[S1] using the GGA-based PBE functional,[S2] augmented by Grimme's D3 dispersion corrections with Becke-Johnson damping together with an approximation of the Coulomb term by density fitting (RI-PBE/D3(BJ)).[S3,S4] Standard Turbomole all-electron def2-TZVPP basis sets were used for all atoms.[S5] For heavier atoms ($Z > 36$; Ru, Os, I), a quasirelativistic energy-consistent small-core pseudopotential (effective-core potential, ECP)[S6,S7] with 28 core electrons was employed. Where applicable, a crystal structure was used as the starting point for full optimization. The optimized structures were characterized as true minima on the potential energy hypersurface by harmonic vibrational frequency analyses.

The two-component relativistic all-electron DFT calculations of the NMR nuclear shieldings[S8] were performed using the Amsterdam Density Functional (ADF) program suite,[S9] employing the PBE0 exchange-correlation functional[S2,S10] in conjunction with Slater-type orbital basis sets of triple-ζ doubly polarized (TZ2P) quality and an integration accuracy of 5.0. The ZORA calculations of NMR shieldings were done by using gauge-including atomic orbitals (GIAOs)[S11] and including the terms from the exchange–correlation (XC) response kernel.[S12] Bulk solvent effects were simulated by means of the conductor-like screening solvation model (COSMO).[S13] The computed ^{11}B and ^{31}P NMR shieldings (σ in ppm) were converted to chemical shifts (δ in ppm) with respect to $BF_3 \cdot Et_2O$ ($\delta(^{11}B) = 0.0$ ppm) and 85% H_3PO_4 ($\delta(^{31}P) = 0.0$ ppm), respectively, considering the shieldings of sp^3-hybridized boron in [**2Me**]$^+$ and phosphorus atom in Et_3PO as secondary standards, with the following NMR shifts: $\delta(^{11}B)$ of the B(sp^3) nucleus in [**2Me**]$^+$ = –9.0 ppm (this work) and $\delta(^{31}P)$ in Et_3PO = 41 ppm in *n*-hexane.[S14]

^{57}Fe Mössbauer parameters (nuclear quadrupole coupling tensors, NQC, and isomer shifts) were computed at the PBE level[S2] with an extensive QZ4P basis set for all atoms, using the ADF program.[S9] While the NQCs were directly computed as expectation values, a commonly used calibration was used to convert computed total densities at the nuclear position into isomer shifts. For this purpose, we employed Neese's training set of 15 molecules,[S15] which were computed at the samel level (PBE/QZ4P//PBE-D3(BJ/def2-TZVPP) as the studied systems ([**1**], [**2**]$^+$, $FeCp_2$, and $FeCp_2^+$).

Reaction energies (Et_3PO and F$^-$-ion affinities) were evaluated at the RI-PBE0-D3(BJ)/def2-TZVPPD level, where the direct COSMO-RS model for real solvents[S16] (considering CH_2Cl_2 as the solvent) was used for energy calculations in condensed-phase.

Natural population analysis (NPA), natural bond orbital (NBO), natural localized molecular orbital (NLMO) analyses,[S17] and evaluation of Mayer bond orders[S18] were performed at the PBE/def2-TZVP level by means of NBO 6.0 code[S19] in conjuction with the Gaussian 16 program.[S20] The Kohn-Sham (KS) wave functions were also analyzed in the DGrid program[S21] by means of the electron localizability indicator (ELI-D),[S22] using a grid 10 points per Bohr.

Bader's QTAIM (quantum theory of atoms-in molecules) analyses[S23] of the KS wave functions, generated in Gaussian 16 at the PBE/def2-TZVP level and stored as .wfx files, were performed using the Multiwfn program.[S24] In the QTAIM analyses, we focused particularly on the delocalization indices (DI) as a measure of the donor-acceptor bond covalency. The DI integrates the electron density in the bonding region between two atoms in question and is closely related to the covalent bond order, reduced by bond polarity (i.e., DI = 1.0 for a “pure” covalent single bond, but DI = 0.0 for a “pure” ionic bond).[S25]

Excitation energies were computed by means of time-dependent DFT at the PBE0-10HF/def2-TZVP level in Gaussian 16[S20] by employing a user-customized PBE0 hybrid functional with 10% exact-exchange admiture and IEF-PCM solvation model.

Structures, molecular orbitals, spin-densities and the results of ELI-D analyses were visualized by CylView,[S26] Chemcraft[S27] and ParaView[S28] program, respectively.

Table S4. Comparison of DFT optimized and experimentally determined short M···B contacts and dip angles α^* in [**2**]$^+$, [**2Me**]$^+$, and structurally related metallocene-BR$_2$ systems (1,1’-fc/rc/oc: 1,1’-ferrocenylene/ruthenocenylene/osmocenylene; PMAFc: 1′,2′,3′,4′,5′-pentamethylazaferrocene; Fc: ferrocenyl)

	DFT [a]				X-ray		
System	*d*(M··B) [Å]	dip angle, α^* [degrees]	DI(M···B)[b]	MBO(M···B)[c]	*d*(M···B) [Å]	dip angle, α^* [degrees]	ref.
1,1’-fc[B(μ-pzMe)$_2$BH]$^+$ ([**2Me**]$^+$)	2.384	40.0	0.181	0.401	2.365	40.6	[e]
1,1’-fc[B(μ-pz)$_2$BH]$^+$ ([**2**]$^+$)	2.342	41.9	0.209	0.425	2.367	41.4	[e]
	2.349[d]	41.5[d]	0.207[d]	0.422[d]			
1,1’-rc[B(μ-pz)$_2$BH]$^+$ ([**2-Ru**]$^+$)	2.337	43.4	0.289	0.504	–	–	
1,1’-oc[B(μ-pz)$_2$BH]$^+$ ([**2-Os**]$^+$)	2.319	45.1	0.343	0.613	–	–	
PMAFc-BCl$_2^+$	2.958	9.9	0.044	0.118	2.905	9.7	[S29]
PMAFc-BH$_2^+$	2.524	30.1	0.136	0.309	–	–	
Fc-py(BPh)$^+$	2.873	26.2	0.072	0.237	2.925	24.7	[S30]
FcBC$_4$Ph$_4$	2.696	28.0	0.099	0.275	2.664	29.4	[S31]
9-Fc-9-borafluorene	2.792	23.7	0.076	0.283	2.746	25.5	[S32]
FcBMe$_2$	2.901	18.7	0.057	0.201	–	–	
FcBH$_2$	2.642	30.2	0.111	0.277	–	–	
FcBBr$_2$	2.904	17.3	0.078	0.221	2.840	18.9	[S33]
FcB(C$_6$F$_5$)$_2$	2.967	15.2	0.077	0.297	2.924	16.0	[S34]

[a] PBE-D3(BJ)/def2-TZVPP results (see Computational details); [b] Delocalization index as a measure of the bond covalency. [c] Mayer bond order.
[d] PBE/def2-TZVPP results without correction for dispersion forces. [e] This work

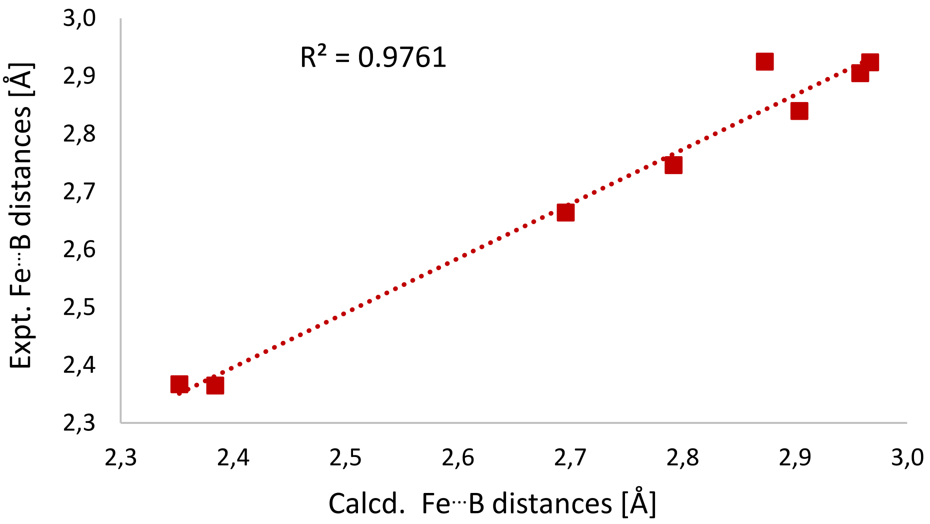

Figure S62. Comparison of DFT (PBE-D3(BJ)/def2-TZVPP) computed and X-ray determined short Fe···B contacts in ferrocene-BR_2 species (cf. Table S4 for numerical data).

Fully optimized structures

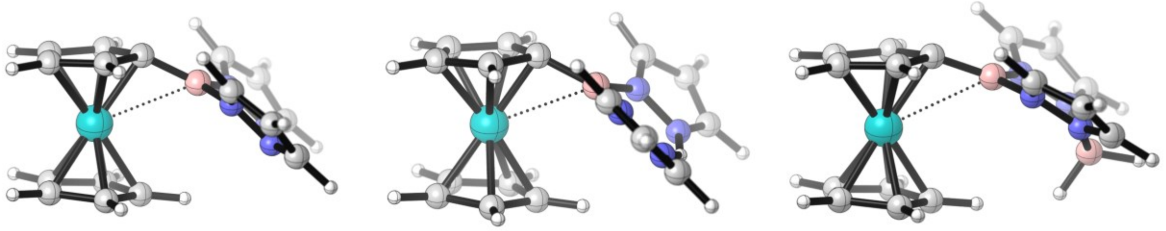

FcBpz$_2$
d(Fe···B$_{sp2}$) = 2.702 Å
α* = 28.0°
ΔE_{stab} = 5.0 kJ/mol

[FcBpz$_2$H]$^+$
d(Fe···B$_{sp2}$) = 2.689 Å
α* = 27.7°
ΔE_{stab} = 16.0 kJ/mol

[FcBpz$_2$(BH$_2$)]$^+$
d(Fe···B$_{sp2}$) = 2.814 Å
α* = 22.0°
ΔE_{stab} = 12.6 kJ/mol

Partially optimized structures with a fixed dip angle α* = 0.0°

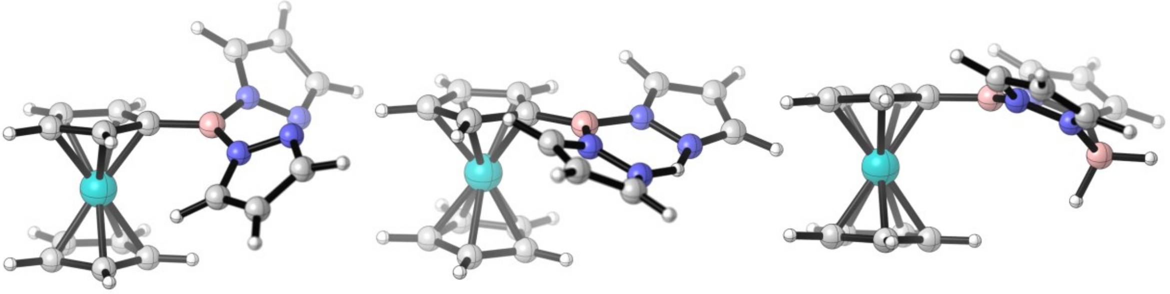

FcBpz$_2$*
d(Fe···B$_{sp2}$) = 3.209 Å

[FcBpz$_2$H]$^{+*}$
d(Fe···B$_{sp2}$) = 3.146 Å

[FcBpz$_2$(BH$_2$)]$^{+*}$
d(Fe···B$_{sp2}$) = 3.120 Å

Figure S63. Fully and partially optimized structures for hypothetical analogs of [**2**]$^+$ with missing BH tether to the second Cp ring. Longer Fe···B contacts along with relatively small stabilization energies, ΔE_{stab} (calculated as the difference between energies of the fully optimized structures (top) and corresponding structures optimized with a fixed dip angle α* = 0.0° (starred molecules, bottom)) validate the essential role of structural strain in the unprecedentedly short Fe···B contact observed in [**2**]$^+$ (cf. Figure S64). PBE-D3(BJ)/def2-TZVPP results.

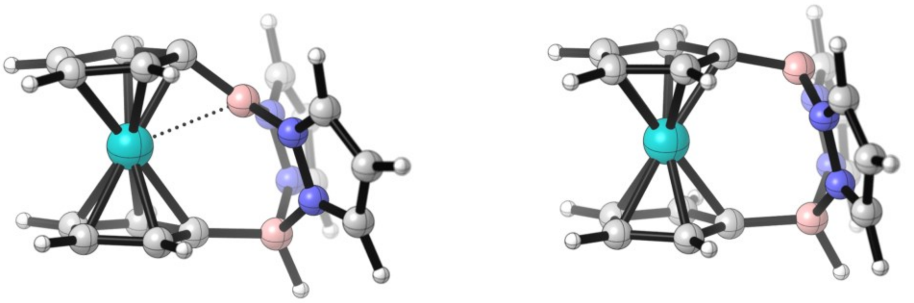

d(Fe···B$_{sp2}$) = 2.342 Å
α^* = 41.9°

ΔE_r = 0.0 kJ/mol

d(Fe···B$_{sp2}$) = 2.923 Å
α^* = 15.4°

ΔE_r = 117.2 kJ/mol

Figure S64. Selected structural parameters and relative energies for the fully optimized structure of [**2**]$^+$ (left) and the partially optimized structure of [**2**$^{\text{pyram}}$]$^+$ with pyramidalized B(sp^2) center (right) possessing the torsional angle θ(N-B-N-C$_{\text{ipso}}$) = 119.8° identical to that in **1**. PBE-D3(BJ)/def2-TZVPP results.

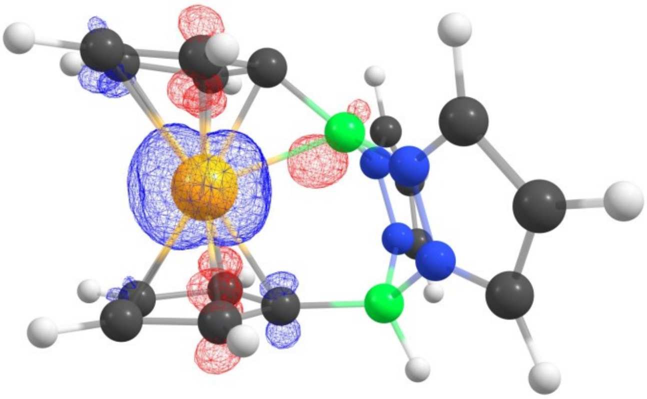

^{3}[**2**]$^+$

d(Fe···B) = 2.272 Å

ΔE$_{S-T}$ = 147 kJ/mol

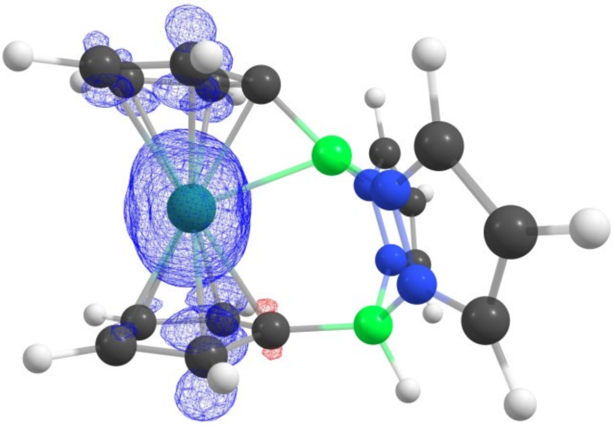

^{3}[**2-Ru**]$^+$

d(Ru···B) = 2.303 Å

ΔE$_{S-T}$ = 280 kJ/mol

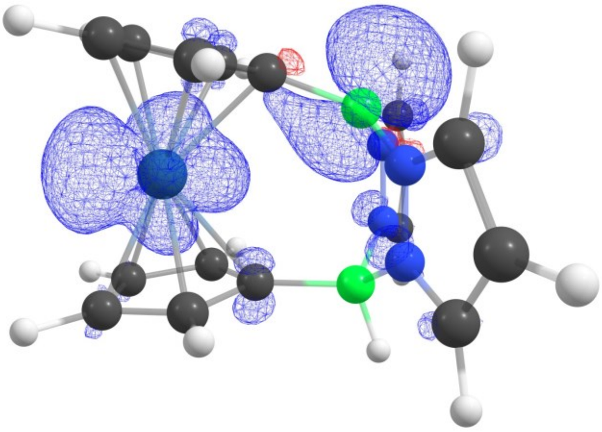

^{3}[**2-Os**]$^+$

d(Os···B) = 3.239 Å

ΔE$_{S-T}$ = 238 kJ/mol

Figure S65. Electron-spin densities (isosurface plots, +/– 0.005 a.u.; positive in blue, negative in red) and M···B distances (M = Fe, Ru, Os) in the lowest-lying triplet states of [**2**]$^+$, [**2-Ru**]$^+$, and [**2-Os**]$^+$ along with their relative energies with respect to the singlet ground-states.

Table S5. Comparison of computed and experimentally determined ^{11}B NMR shifts and boron atomic charges, q(B), within a series of selected boron-based Lewis acids (1,1'-fc/rc/oc: 1,1'-ferrocenylene/ruthenocenylene/osmocenylene; PMAFc: 1′,2′,3′,4′,5′-pentamethylazaferrocene; Fc: ferrocenyl)

System		q(B)	$\sigma(^{11}\mathrm{B})_{\mathrm{calcd}}$ [ppm]	$\delta(^{11}\mathrm{B})_{\mathrm{calcd}}$ [ppm]	$\delta(^{11}\mathrm{B})_{\mathrm{expt}}$ [ppm]	solvent	ref.
1,1'-fc[B(μ-pzMe)$_2$BH]$^+$ ([**2Me**]$^+$)	sp^2	0.95	80.7	25.9	23.4	CD_2Cl_2	[b]
	sp^3	0.33	115.5	–9.0	–9.0		
1,1'-fc[B(μ-pz)$_2$BH]$^+$ ([**2**]$^+$)	sp^2	0.90	80.7	25.8	23.5	CD_2Cl_2	[b]
	sp^3	0.34	112.2	–5.7	–5.2		
1,1'-rc[B(μ-pz)$_2$BH]$^+$ ([**2-Ru**]$^+$)	sp^2	0.84	86.5	20.0	-		
	sp^3	0.33	112.4	–5.9	-		
1,1'-oc[B(μ-pz)$_2$BH]$^+$ ([**2-Os**]$^+$)	sp^2	0.74	93.6	12.9	-		
	sp^3	0.33	112.7	–6.2	-		
PMAFc-BH$_2^+$		0.45	66.2	40.3	40	CD_2Cl_2	[S29]
Fc-py(BPh)$^+$		0.93	60.2	46.3	45.4	CD_2Cl_2	[S30]
9-BBN-NEt$_3^+$		1.59	15.7	90.9	85.1	CD_2Cl_2	[S35]
CatB$^+$		1.54	78.6	27.9	21.6	C_6D_6	[S36]
Mes$_2$B-C$_6$H$_4$-PPh$_3^+$ ([**A**]$^+$)		1.07	31.1	75.4	75.0	$CDCl_3$	[S37]
(C$_6$F$_5$)B(CH$_2$)(C$_6$F$_4$)P*t*Bu$_2^+$ ([**B**]$^+$)		0.85	38.4	68.1	65.4	CD_2Cl_2	[S38]
Oxazaborolidinium$^+$ ([**C**]$^+$)		1.13	66.3	40.2	-		
Borabenzylic-NMe$_2^+$		0.76	55.8	50.7	38.7	CD_2Cl_2	[S39]
Boratriptycene-PH$^+$ ([**E**]$^+$)		0.89	19.7	86.8	-		
E–NTf$_2$		0.46	101.5	5.0			
[**E**]$^+$ + NTf$_2^-$ ↔ **E**–NTf$_2$		0.68	60.6	45.9	-		
FcBC$_4$Ph$_4$		0.78	62.0	44.6	47.4	CD_2Cl_2	[S31]
9-Fc-9-borafluorene		0.75	57.4	49.1	53.0	C_6D_6	[S32]
FcB(C$_6$F$_5$)$_2$		0.82	48.9	57.6	53.7	C_6D_6	[S34]
FcBMe$_2$		0.82	37.5	69.0	71.6	CS_2	[S35]
FcBBr$_2$		0.36	56.2	50.3	46.7	CS_2	[S31]
BF$_3$		1.45	89.6	16.9	10.0	$CD_3C_6D_{11}$	[S40]
BCl$_3$		0.26	56.4	50.2	46.5	$CD_3C_6D_{11}$	[S40]
BBr$_3$		0.01	67.1	39.5	38.7	$CD_3C_6D_{11}$	[S40]
BI$_3$		0.00	120.0	-13.5	-7.9	$CD_3C_6D_{11}$	[S40]
BPh$_3$		0.81	40.8	65.8	67	C_6D_6	[S41]
B(OMe)$_3$		1.24	86.8	19.7	19	$CDCl_3$	[S42]
B(OC$_6$F$_5$)$_3$		1.29	86.2	20.4	14.8	C_6D_6	[S43]
B(C$_6$F$_5$)$_3$		0.80	49.4	57.1	59	C_6D_6	[S43]
Boraadamantane		0.84	19.7	86.8	82.6	$CDCl_3$	[S44]
Boratriptycene (**D**)		0.85	21.2	85.3			
Boratriptycene–NTf$_2^-$ [**D**–NTf$_2$]$^-$		0.38	96.2	10.3			
D + NTf$_2^-$ ↔ [**D**–NTf$_2$]$^-$		0.62	58.7	47.8	60.9	CD_2Cl_2	[S45]

[a] PBE0-XC/TZ2P/COSMO(DCM) results for PBE-D3(BJ)/def2-TZVPP geometries (cf. Computational details); [b] This work.

Notes to Table S5:

$\sigma(^{11}B)_{calcd}$ corresponds to the computed chemical shielding, while $\delta(^{11}B)_{calcd}$ corresponds to the chemical shift (in ppm with respect to $BF_3{\bullet}OEt_2$). The two quantities are related as follows:

$$\delta(^{11}B)_{calcd} = \sigma(^{11}B)_{ref} - \sigma(^{11}B)_{calcd} + \delta(^{11}B)_{ref}$$

where we considered the computed shielding of the sp^3-hybridized B atom in [**2Me**]$^+$ as a secondary standard: $\sigma(^{11}B)_{ref} = 115.5$ ppm; $\delta(^{11}B)_{ref} = -9.0$ ppm.

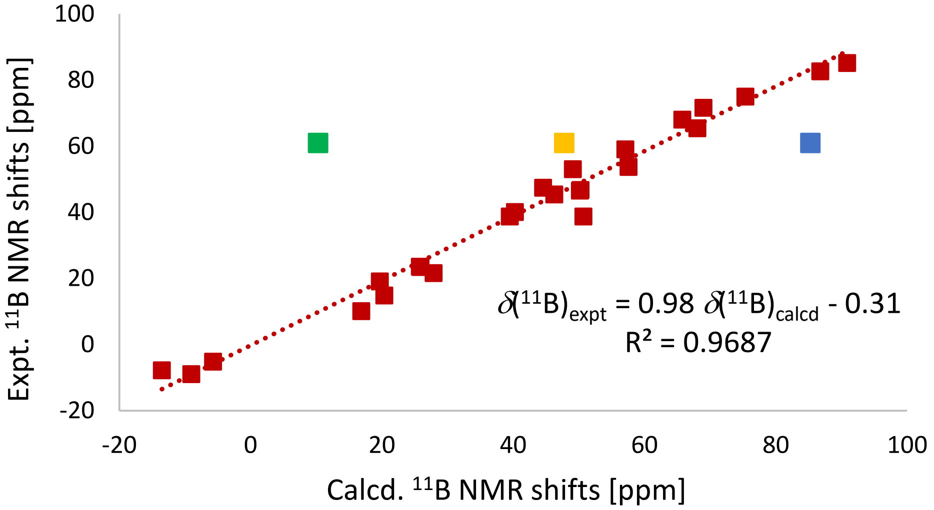

Figure S66. Comparison of DFT (PBE0-XC/TZ2P) computed and experimentally determined ^{11}B NMR shifts within a set of selected boron-based Lewis acids (cf. Table S5 for numerical data). The blue point corresponds to free (naked) boratriptycene **D**, the green one to the NTf_2^--coordinated species [**D**–NTf_2]$^-$, the pale yellow point to an averaged value between the free and coordinated species.

Table S6. Computed and experimental ^{57}Fe Moessbauer spectral parameters for **1**, [**2**]$^+$, FeCp$_2$, and [FeCp$_2$]$^+$ (1,1'-fc: 1,1'-ferrocenylene)

System	DFT [a] δ (mm s^{-1})	DFT [a] ΔE_Q (mm s^{-1})	Expt. δ (mm s^{-1})	Expt. ΔE_Q (mm s^{-1})	ref.
1,1'-fc[B(H)(μ-pz)]$_2$ (**1**)	0.41	2.246	0.52	2.28	[b]
1,1'-fc[B(μ-pz)$_2$BH]$^+$ ([**2**]$^+$)	0.39	2.521	0.49	2.35	[b]
FeCp$_2$	0.43	3.003	0.52	2.34	
[FeCp$_2$]$^+$	0.51	0.348	0.54	0.76	

[a] PBE/TZ2P results (see Computational details); [b] This work (Table S1).

Table S7. Lewis acidities of selected boron-based acids assessed by the ^{31}P NMR chemical shifts of their Et$_3$PO adducts, δ(^{31}P), and Gutmann-Beckett acceptor numbers, AN (theory vs. experiment)^{a,b}; 1,1’-fc/rc/oc: 1,1’-ferrocenylene/ruthenocenylene/osmocenylene; PMAFc: 1′,2′,3′,4′,5′-pentamethylazaferrocene; Fc: ferrocenyl.

LA	σ(^{31}P)$_{\mathrm{calcd}}$ [ppm]	δ(^{31}P)$_{\mathrm{calcd}}$ [ppm]	AN$_{\mathrm{calcd}}$	δ(^{31}P)$_{\mathrm{expt}}$ [ppm]	solvent	AN$_{\mathrm{expt}}$	ref.
1,1’-fc[B(μ-pzMe)$_2$BH]$^+$ ([**2Me**]$^+$)	249.0	89.1	106.3	-	-	-	
1,1’-fc[B(μ-pz)$_2$BH]$^+$ ([**2**]$^+$)	247.2	90.9	110.3	91.0	CD$_2$Cl$_2$	110.5	[c]
1,1’-rc[B(μ-pz)$_2$BH]$^+$ ([**2-Ru**]$^+$)	248.1	90.0	108.3	-	-	-	
1,1’-rc[B(μ-pz)$_2$BH]$^+$ ([**2-Os**]$^+$)	249.5	88.6	105.2	-	-	-	
PMAFc-BH$_2^+$	252.7	85.4	98.2	82.8	CD$_2$Cl$_2$	92.4	[S29]
Fc-py(BPh)$^+$	253.5	84.6	96.4	83.0	CD$_2$Cl$_2$	92.8	[S30]
9-BBN-NEt$_3^+$	263.6	74.5	74.0	-	-	-	
CatB$^+$	227.4	110.7	154.0	106.9	CD$_2$Cl$_2$	145.6	[S36]
Mes$_2$B-C$_6$H$_4$-PPh$_3^+$ ([**A**]$^+$)	264.5	73.6	72.0	-	-	-	
(C$_6$F$_5$)B(CH$_2$)(C$_6$F$_4$)P^{t}Bu$_2^+$ ([**B**]$^+$)	255.7	82.4	91.4	80.4	CD$_2$Cl$_2$	87.1	[S38]
Oxazaborolidinium$^+$ ([**C**]$^+$)	250.5	87.6	103.0	-	-	-	
Borabenzylic-NMe$_2^+$	251.2	86.9	101.4	85.7	CD$_2$Cl$_2$	98.8	[S39]
Boratriptycene-PH$^+$ ([**E**]$^+$)	259.6	78.5	82.8	79.3	CD$_2$Cl$_2$	84.6	[S46]
FcBC$_4$Ph$_4$	260.2	77.9	81.6	-	-	-	
9-Fc-9-borafluorene	264.5	73.6	72.0	-	-	-	
FcB(C$_6$F$_5$)$_2$	266.9	71.2	66.7	68.3*	THF	60.3	[S34]
FcBMe$_2$	271.4	66.7	56.8	-	-	-	
FcBBr$_2$	259.3	78.8	83.6	-	-	-	
BF$_3$	265.0	73.1	70.9	80.9	CD$_2$Cl$_2$	88.2	[S14]
BCl$_3$	257.7	80.4	87.2	88.7	CD$_2$Cl$_2$	105.4	[S14]
BBr$_3$	254.3	83.8	94.6	90.3	CD$_2$Cl$_2$	109.0	[S14]
BI$_3$	251.0	87.2	102.0	92.9	CD$_2$Cl$_2$	114.7	[S14]
BPh$_3$	269.2	68.9	61.7	65.9	C$_6$D$_6$	55.0	[S14]
B(OMe)$_3$	286.0	52.1	24.5	48.1	C$_6$D$_6$	15.7	[S14]
B(OC$_6$F$_5$)$_3$	256.3	81.8	90.1	80.9	C$_6$D$_6$	88.2	[S14]
B(C$_6$F$_5$)$_3$	260.0	78.1	81.9	76.6	C$_6$D$_6$	78.7	[S36]
Boraadamantane	266.5	71.6	67.6	-	-	-	
Boratriptycene (**D**)	262.7	75.4	76.0	75.0	CD$_2$Cl$_2$	75.1	[S45]

---

[a] PBE0/def2-TZVP/PCM(DCM) results for PBE-D3(BJ)/def2-TZVPP geometries (cf. Computational details); [b] Acceptor number, AN = 2.21 × [δ(^{31}P, LA·Et$_3$PO) – 41]; [c] This work.

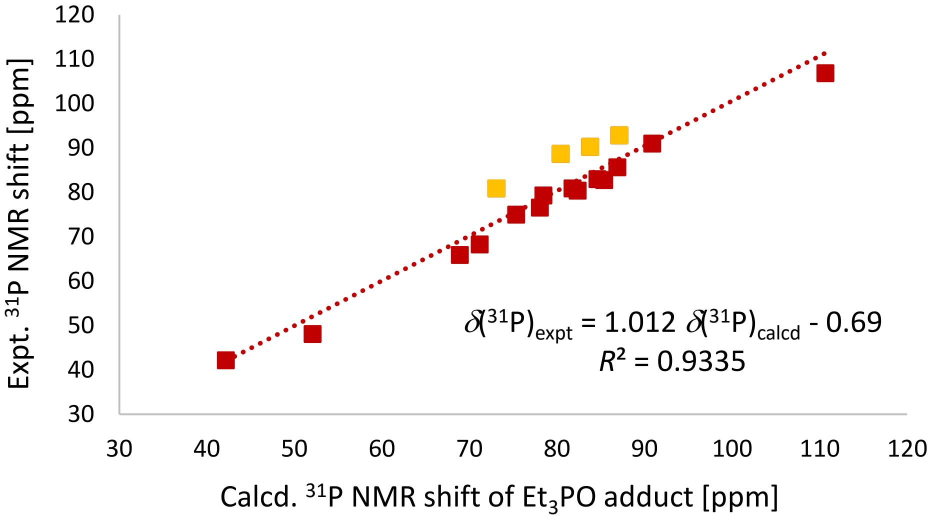

Figure S67. Comparison of DFT (PBE0-XC/TZ2P) computed and experimentally determined ^{31}P NMR shifts within a set of Et_3PO adducts with selected boron-based Lewis acids (cf. Table S7 for numerical data). An excellent linear fit ($R^2 = 0.991$) is obtained upon omitting data for $BX_3 \cdot OPEt_3$ adducts (X = F, Cl, Br, I; pale orange data points).

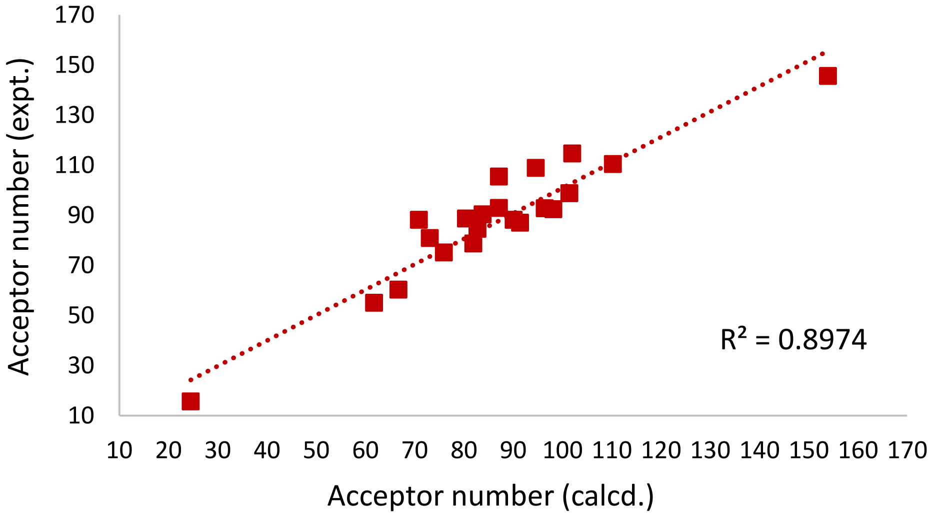

Figure S68. Correlation of DFT computed and experimentally determined Gutmann-Beckett acceptor numbers (cf. Table S7 for numerical data).

Table S8. Lewis acidities assessed by F$^-$-ion affinities (gas-phase results)[a]; 1,1’-fc/rc/oc: 1,1’-ferrocenylene/ruthenocenylene/osmocenylene; PMAFc: 1′,2′,3′,4′,5′-pentamethylazaferrocene; Fc: ferrocenyl

LA	LA^q [a.u.]	CF$_3$O$^-$ [a.u.]	LA-F^{q-1} [a.u.]	CF$_2$O [a.u.]	FIA [kJ/mol]
1,1’-fc[B(μ-pzMe)$_2$BH]$^+$ ([**2Me**]$^+$)	-2307.36707	-412.73069	-2407.43096	-312.85190	695
1,1’-fc[B(μ-pz)$_2$BH]$^+$ ([**2**]$^+$)	-2150.19808	-412.73069	-2250.27471	-312.85190	728
1,1’-rc[B(μ-pz)$_2$BH]$^+$ ([**2-Ru**]$^+$)	-981.65830	-412.73069	-1081.72158	-312.85190	693
1,1’-oc[B(μ-pz)$_2$BH]$^+$ ([**2-Os**]$^+$)	-977.44582	-412.73069	-1077.50308	-312.85190	678
PMAFc-BH$_2^+$	-1888.59476	-412.73069	-1988.66040	-312.85190	700
Fc-py(BPh)$^+$	-2231.32962	-412.73069	-2331.38301	-312.85190	667
9-BBN-NEt$_3^+$	-629.86222	-412.73069	-729.91492	-312.85190	666
CatB$^+$	-405.73739	-412.73069	-505.99863	-312.85190	1213
CatB(CH$_2$Cl$_2$)$^+$	-1365.25099	-412.73069	-1465.40032	-312.85190	919
Mes$_2$B-C$_6$H$_4$-PPh$_3^+$ ([**A**]$^+$)	-1989.81581	-412.73069	-2089.80585	-312.85190	501
(C$_6$F$_5$)B(CH$_2$)(C$_6$F$_4$)P*t*Bu$_2^+$([**B**]$^+$)	-2075.64272	-412.73069	-2175.71090	-312.85190	706
Oxazaborolidinium$^+$ ([**C**]$^+$)	-1044.19209	-412.73069	-1144.25388	-312.85190	689
Borabenzylic-NMe$_2^+$	-429.82501	-412.73069	-529.91174	-312.85190	755
Boratriptycene-PH$^+$ ([**E**]$^+$)	-1059.02245	-412.73069	-1159.12787	-312.85190	804
[**E**(CH$_2$Cl$_2$)]$^+$	-2018.46313	-412.73069	-2118.52955	-312.85190	702
E–NTf$_2$	-2885.78205	-412.73069	-2985.70908	-312.85190	336
FcBC$_4$Ph$_4$	-2752.72846	-412.73069	-2852.65144	-312.85190	325
9-Fc-9-borafluorene	-2136.30646	-412.73069	-2236.21923	-312.85190	298
FcB(C$_6$F$_5$)$_2$	-3129.37060	-412.73069	-3229.30293	-312.85190	350
FcBMe$_2$	-1754.31962	-412.73069	-1854.21158	-312.85190	244
FcBBr$_2$	-6822.35340	-412.73069	-6922.29218	-312.85190	366
BF$_3$	-324.39163	-412.73069	-424.31818	-312.85190	334
BCl$_3$	-1405.14128	-412.73069	-1505.08927	-312.85190	391
BBr$_3$	-7746.51002	-412.73069	-7846.46847	-312.85190	418
BI$_3$	-918.07371	-412.73069	-1018.03947	-312.85190	437
BPh$_3$	-719.24242	-412.73069	-819.15455	-312.85190	296
B(OMe)$_3$	-370.12103	-412.73069	-469.99405	-312.85190	194
B(OC$_6$F$_5$)$_3$	-2432.67420	-412.73069	-2532.62462	-312.85190	397
B(C$_6$F$_5$)$_3$	-2207.04617	-412.73069	-2307.00467	-312.85190	418
Boraadamantane	-376.55637	-412.73069	-476.46335	-312.85190	283
Boratriptycene ([**D**])	-756.08669	-412.73069	-856.05456	-312.85190	443
D(CH$_2$Cl$_2$)	-1715.51578	-412.73069	-1815.45625	-312.85190	371
[**D**–NTf$_2$]$^-$	-2582.73200	-412.73069	-2682.63578	-312.85190	275
[Fc–SiMe$_2$]$^+$	-2018.65903	-412.73069	-2118.76236	-312.85190	798

[a] PBE0-D3(BJ)/def2-TZVPPD results (see Computational details).

Table S9. Lewis acidities assessed by F$^-$-ion affinities (results using DCOSMO-RS solvation model)[a]; 1,1'-fc/rc/oc: 1,1'-ferrocenylene/ruthenocenylene/osmocenylene; PMAFc: 1′,2′,3′,4′,5′-pentamethylazaferrocene; Fc: ferrocenyl

LA	LA^q [a.u.]	CF_3O^- [a.u.]	LA-F^{q-1} [a.u.]	CF_2O [a.u.]	FIA [kJ/mol]
1,1'-fc[B(μ-pzMe)$_2$BH]$^+$ ([**2Me**]$^+$)	-2307.42836	-412.81482	-2407.45105	-312.85480	374
1,1'-fc[B(μ-pz)$_2$BH]$^+$ ([**2**]$^+$)	-2150.26237	-412.81482	-2250.29355	-312.85480	396
1,1'-rc[B(μ-pz)$_2$BH]$^+$ ([**2-Ru**]$^+$)	-981.72561	-412.81482	-1081.74562	-312.85480	367
1,1'-oc[B(μ-pz)$_2$BH]$^+$ ([**2-Os**]$^+$)	-977.51291	-412.81482	-1077.52734	-312.85480	352
PMAFc-BH$_2^+$	-1888.66005	-412.81192	-1988.68494	-312.85480	387
Fc-py(BPh)$^+$	-2231.39383	-412.81482	-2331.40817	-312.85480	352
9-BBN-NEt$_3^+$	-629.92923	-412.81482	-729.93044	-312.85480	317
CatB$^+$	-405.81475	-412.81482	-506.00739	-312.85480	820
CatB(CH$_2$Cl$_2$)$^+$	-1365.32759	-412.81482	-1465.41813	-312.85480	552
Mes$_2$B-C$_6$H$_4$-PPh$_3^+$ ([**A**]$^+$)	-1989.88534	-412.81482	-2089.86381	-312.85480	257
(C$_6$F$_5$)B(CH$_2$)(C$_6$F$_4$)P^{t}Bu$_2^+$ ([**B**]$^+$)	-2075.70820	-412.81482	-2175.73290	-312.85480	379
Oxazaborolidinium$^+$ ([**C**]$^+$)	-1044.26831	-412.81482	-1144.28451	-312.85480	356
Borabenzylic-NMe$_2^+$	-429.89661	-412.81482	-529.92597	-312.85480	392
Boratriptycene-PH$^+$ ([**E**]$^+$)	-1059.09439	-412.81482	-1159.15537	-312.85480	474
[**E**(CH$_2$Cl$_2$)]$^+$	-2018.53587	-412.81482	-2118.56610	-312.85480	393
E–NTf$_2$	-2885.81584	-412.81482	-2985.80274	-312.85480	280
FcBC$_4$Ph$_4$	-2752.66128	-412.81482	-2852.63385	-312.85480	242
9-Fc-9-borafluorene	-2136.32804	-412.81482	-2236.29377	-312.85480	224
FcB(C$_6$F$_5$)$_2$	-3129.39659	-412.81482	-3229.37214	-312.85480	250
FcBMe$_2$	-1754.33124	-412.81482	-1854.28643	-312.85480	196
FcBBr$_2$	-6822.36848	-412.81482	-6922.36390	-312.85480	302
BF$_3$	-324.39510	-412.81482	-424.40090	-312.85480	329
BCl$_3$	-1405.14926	-412.81482	-1505.16171	-312.85480	347
BBr$_3$	-7746.52086	-412.81482	-7846.53912	-312.85480	362
BI$_3$	-918.08916	-412.81482	-1018.10898	-312.85480	366
BPh$_3$	-719.25857	-412.81482	-819.22636	-312.85480	229
B(OMe)$_3$	-370.13536	-412.81482	-470.08093	-312.85480	171
B(OC$_6$F$_5$)$_3$	-2432.68287	-412.81482	-2532.67443	-312.85480	292
B(C$_6$F$_5$)$_3$	-2207.05302	-412.81482	-2307.05323	-312.85480	315
Boraadamantane	-376.56443	-412.81482	-476.53679	-312.85480	241
Boratriptycene (**D**)	-756.10791	-412.81482	-856.12943	-312.85480	370
D(CH$_2$Cl$_2$)	-1715.54280	-412.81482	-1815.54017	-312.85480	307
[**D**–NTf$_2$]$^-$	-2582.78689	-412.81482	-2682.77681	-312.85480	287
[Fc–SiMe$_2$]$^+$	-2018.72673	-412.81482	-2118.77604	-312.85480	443

[a] PBE0-D3(BJ)/def2-TZVPPD/D-COSMO-RS results considering CH$_2$Cl$_2$ as the solvent (see Computational details).

Table S10. Calculated Et_3PO affinities and pertinent contacts in Et_3PO adducts with selected boron-based Lewis acids (results using DCOSMO-RS solvation)[a]; 1,1'-fc/rc/oc: 1,1'-ferrocenylene/ruthenocenylene/osmocenylene; PMAFc: 1′,2′,3′,4′,5′-pentamethylazaferrocene; Fc: ferrocenyl

LA	Et_3PO affinities [kJ/mol]	$d(B\text{-}O_{Et3PO})$ [Å]	$d(P\text{-}O_{Et3PO})$ [Å]
1,1'-fc[B(μ-pzMe)$_2$BH]$^+$([**2Me**]$^+$)	112	1.489	1.556
1,1'-fc[B(μ-pz)$_2$BH]$^+$ ([**2**]$^+$)	155	1.478	1.551
1,1'-rc[B(μ-pz)$_2$BH]$^+$ ([**2-Ru**]$^+$)	114	1.480	1.550
1,1'-oc[B(μ-pz)$_2$BH]$^+$ ([**2-Os**]$^+$)	100	1.481	1.550
PMAFc-BH_2^+	152	1.518	1.546
Fc-py(BPh)$^+$	129	1.509	1.547
9-BBN-NEt_3^+	44	1.547	1.521
CatB$^+$	551	1.367	1.585
CatB(CH_2Cl_2)$^+$	286		
Mes_2B-C_6H_4-PPh_3^+ ([**A**]$^+$)	25	1.582	1.530
(C_6F_5)B(CH_2)(C_6F_4)P*t*Bu_2^+ ([**B**]$^+$)	146	1.520	1.537
Oxazaborolidinium$^+$ ([**C**]$^+$)	122	1.506	1.549
Borabenzylic-NMe_2^+	163	1.487	1.546
Boratriptycene-PH$^+$ ([**E**]$^+$)	234	1.493	1.528
[**E**(CH_2Cl_2)]$^+$	152		
E–NTf_2	35		
$FcBC_4Ph_4$	77	1.566	1.535
9-Fc-9-borafluorene	94	1.572	1.533
FcB(C_6F_5)$_2$	71	1.546	1.523
$FcBMe_2$	38	1.624	1.524
$FcBBr_2$	105	1.477	1.550
BF_3	118	1.501	1.541
BCl_3	131	1.454	1.552
BBr_3	144	1.438	1.554
BI_3	147	1.428	1.554
BPh_3	62	1.568	1.526
B(OMe)$_3$	2	1.595	1.550
B(OC_6F_5)$_3$	97	1.483	1.546
B(C_6F_5)$_3$	109	1.519	1.513
Boraadamantane	76	1.587	1.525
Boratriptycene (**D**)	184	1.512	1.525
D(CH_2Cl_2)	119		
[**D**–NTf_2]$^-$	97		
[Fc–$SiMe_2$]$^+$	167		

[a] PBE0-D3(BJ)/def2-TZVPPD/D-COSMO-RS results considering CH_2Cl_2 as the solvent (see Computational details).

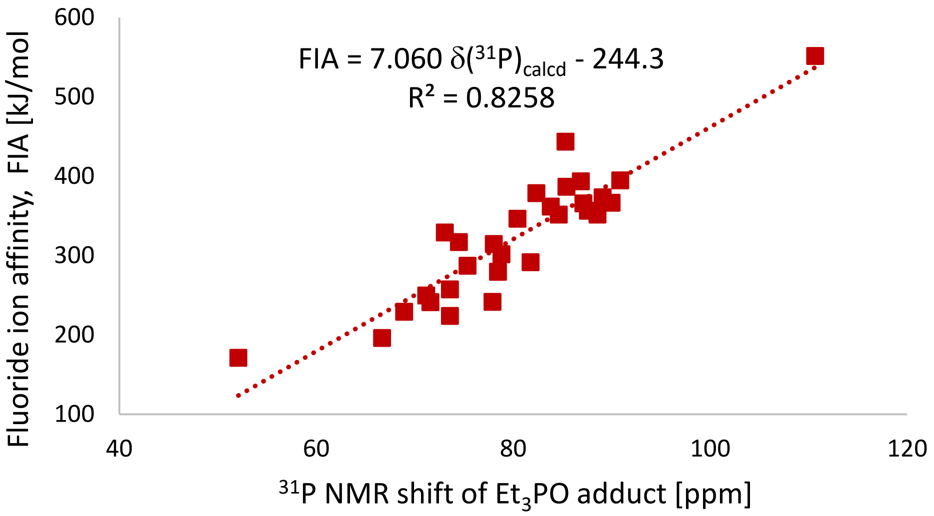

Figure S69. Correlation between computed F⁻-ion affinities and ^{31}P NMR shifts of Et_3PO adducts with selected boron-based Lewis acids (cf. Tables S7 and S9 for numerical data).

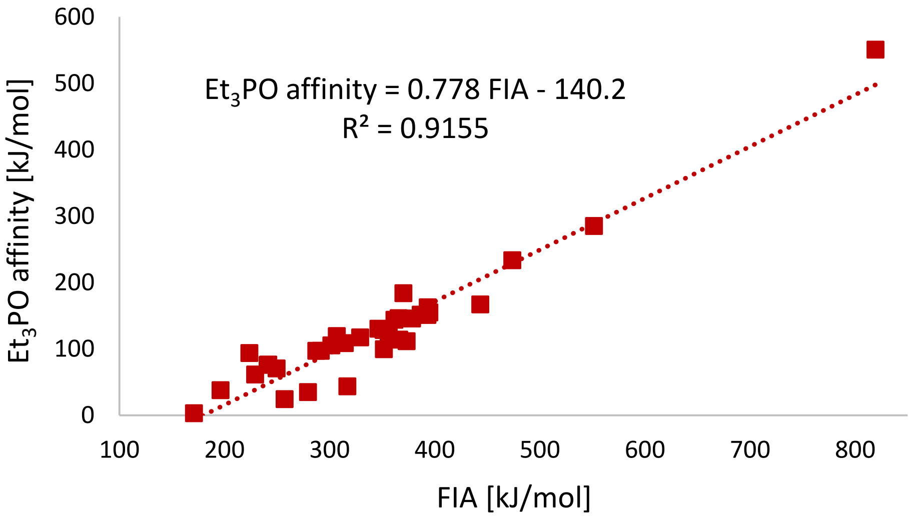

Figure S70. Correlation of computed F⁻-ion affinities with Et_3PO affinities for selected boron-based Lewis acids (cf. Tables S9 and S10 for numerical data).

Table S11. TD-DFT computed singlet excitation energies in 1,1'-fc[B(H)(μ-pz)]$_2$ ([**1**]) and NPA charge changes upon photoexcitation [a]

	energy [eV]	λ_{max} [nm]	f_{osc}	dominant MO transitions		NPA charge changes for given fragments				assignment
						Fe	2 × Cp	2 × BH	2 × pz	
S_1	2.76	449	0.0000	99%	HOMO → LUMO	0.34	0.45	-0.02	-0.77	$FeCp_2$ → pz_2
S_2	**2.77**	**447**	**0.0010**	**95%**	**HOMO-1 → LUMO**	**0.33**	**0.44**	**-0.01**	**-0.76**	**$FeCp_2$ → pz_2**
S_3	2.95	419	0.0000	85% 12%	HOMO → LUMO+1 HOMO-1 → LUMO+2	0.33	0.15	0.00	-0.48	$FeCp_2$ → pz_2

[a] PBE0-10HF/def2-TZVP/PCM(DCM) results; the most intense absorptions are given in bold (see Figure S71 for relevant frontier MOs).

Table S12. TD-DFT computed singlet-singlet excitation energies in 1,1'-fc[B(μ-pz)$_2$BH]$^+$ ([**2**]$^+$) and NPA charge changes upon photoexcitation [a]

	energy [eV]	λ_{max} [nm]	f_{osc}	dominant MO transitions		NPA charge changes for given fragments					assignment
						Fe	2 × Cp	B(sp^2)	BH	2 × pz	
S_1	2.75	451	0.0005	44%	HOMO → LUMO+2	0.34	-0.30	-0.02	0.00	-0.02	Fe → Cp$_2$
				40%	HOMO-1 → LUMO+1						
				16%	HOMO-1 → LUMO						
S_2	2.77	448	0.0001	46%	HOMO-1 → LUMO+2	0.34	-0.23	-0.04	0.00	-0.07	Fe → Cp$_2$
				38%	HOMO → LUMO						
				12%	HOMO → LUMO+1						
S_3	2.90	428	0.0001	79%	HOMO-1 → LUMO+2	0.32	-0.31	-0.01	0.00	-0.01	Fe → Cp$_2$
				10%	HOMO-2 → LUMO+2						
S_4	3.09	401	0.0005	53%	HOMO → LUMO	0.34	0.09	-0.09	0.00	-0.34	Fe → pz$_2$
				41%	HOMO → LUMO+1						
S_5	3.20	387	0.0009	75%	HOMO-1 → LUMO	0.32	0.17	-0.09	0.00	-0.39	Fe → pz$_2$
				12%	HOMO → LUMO+2						
S_6	**3.23**	**383**	**0.0040**	**72%**	**HOMO-2 → LUMO+1**	**0.29**	**-0.29**	**0.03**	**0.00**	**-0.03**	**Fe → Cp$_2$**
				18%	**HOMO-2 → LUMO**						
S_7	3.58	346	0.0013	55%	HOMO-1 → LUMO+1	0.31	-0.26	-0.01	0.00	-0.04	Fe → Cp$_2$
				45%	HOMO → LUMO+2						
S_8	**3.91**	**317**	**0.0815**	**68%**	**HOMO-2 → LUMO**	**0.25**	**0.18**	**0.01**	**0.01**	**-0.44**	**FeCp$_2$ → pz$_2$**
				20%	**HOMO-2 → LUMO+1**						
				10%	**HOMO → LUMO+3**						

[a] PBE0-10HF/def2-TZVP/PCM(DCM) results; the most intense absorptions given in bold (see Figure S72 for relevant frontier MOs).

Table S13. TD-DFT computed singlet-singlet excitation energies in 1,1'-rc[B(μ-pz)$_2$BH]$^+$ ([**2-Ru**]$^+$) and charge changes upon photoexcitation [a]

	energy [eV]	λ_{max} [nm]	f_{osc}	dominant MO transitions		NPA charge changes for given fragments					assignment
						Ru	2 × Cp	B(sp^2)	BH	2 × pz	
S_1	**3.59**	**346**	**0.0191**	**98%**	**HOMO → LUMO**	**0.38**	**0.22**	**-0.06**	**0.00**	**-0.53**	**RuCp$_2$ → pz$_2$**
S_2	3.66	338	0.0044	99%	HOMO-1 → LUMO	0.37	0.23	-0.08	0.00	-0.51	RuCp$_2$ → pz$_2$
S_3	3.98	311	0.0016	77%	HOMO → LUMO+1	0.34	-0.32	-0.01	0.00	-0.01	Ru → Cp$_2$
				14%	HOMO-1 → LUMO+3						
S_4	4.00	310	0.0003	55%	HOMO → LUMO+3	0.34	-0.34	0.00	0.00	0.00	Ru → Cp$_2$
				45%	HOMO → LUMO+2						
S_5	4.18	296	0.0000	94%	HOMO-1 → LUMO+1	0.33	-0.31	-0.02	-0.01	0.01	Ru → Cp$_2$

[a] PBE0-10HF/def2-TZVP/PCM(DCM) results; the most intense absorptions given in bold

Table S14. TD-DFT computed singlet-singlet excitation energies in 1,1'-oc[B(μ-pz)$_2$BH]$^+$ ([**2-Os**]$^+$) and charge changes upon photoexcitation [a]

	energy [eV]	λ_{max} [nm]	f_{osc}	dominant MO transitions		NPA charge changes for given fragments					assignment
						Os	2 × Cp	B(sp^2)	BH	2 × pz	
S_1	**3.67**	**338**	**0.0198**	**99%**	**HOMO → LUMO**	**0.41**	**0.22**	**-0.05**	**0.00**	**-0.58**	**OsCp$_2$ → pz$_2$**
S_2	3.76	329	0.0064	99%	HOMO-1 → LUMO	0.37	0.24	-0.05	0.00	-0.56	OsCp$_2$ → pz$_2$
S_3	4.44	280	0.0061	84%	HOMO → LUMO+1	0.40	0.11	0.04	-0.01	-0.54	OsCp$_2$ → pz$_2$
				15%	HOMO-1 → LUMO+3						
S_4	4.49	276	0.0012	72%	HOMO → LUMO+3	0.35	-0.28	-0.01	0.00	-0.06	Os → Cp$_2$
				13%	HOMO-1 → LUMO+1						
S_5	4.56	272	0.0071	60%	HOMO-1 → LUMO+1	0.32	0.18	0.04	-0.01	-0.54	OsCp$_2$ → pz$_2$
				28%	HOMO-2 → LUMO						

[a] PBE0-10HF/def2-TZVP/PCM(DCM) results; the most intense absorptions given in bold

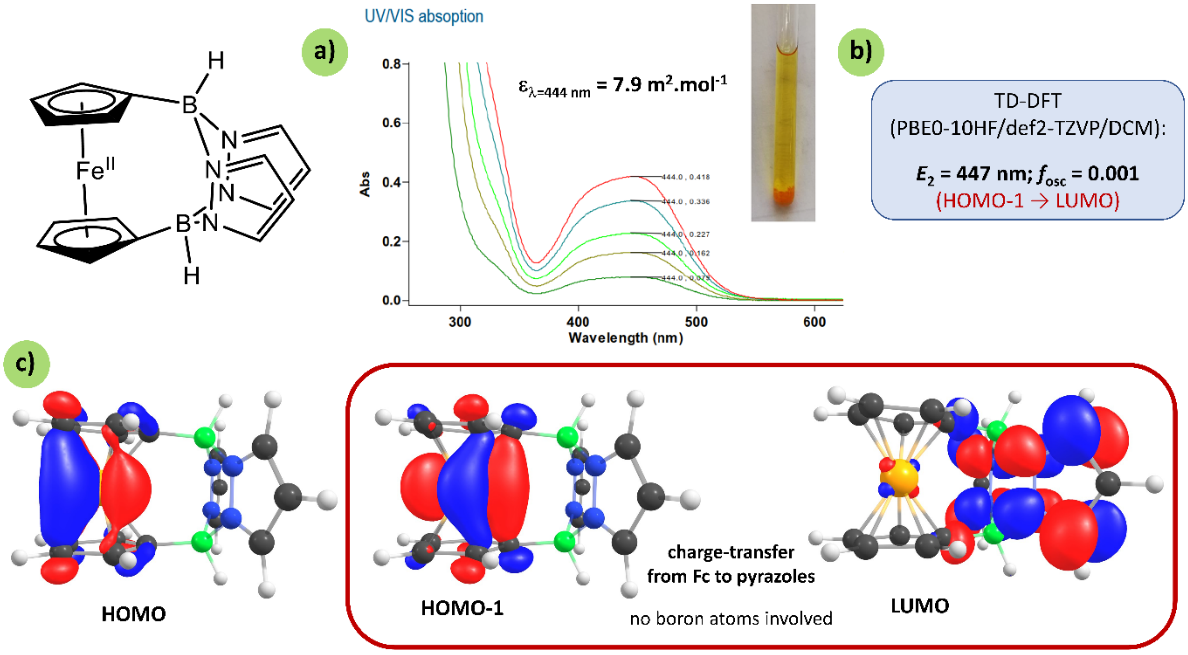

Figure S71. (a) Experimental UV-vis spectrum of **1** in comparison with TD-DFT calculated parameters (b). (c) Relevant frontier MOs of **1** participating in UV-vis absorption. See Table S11 for computed spectral parameters.

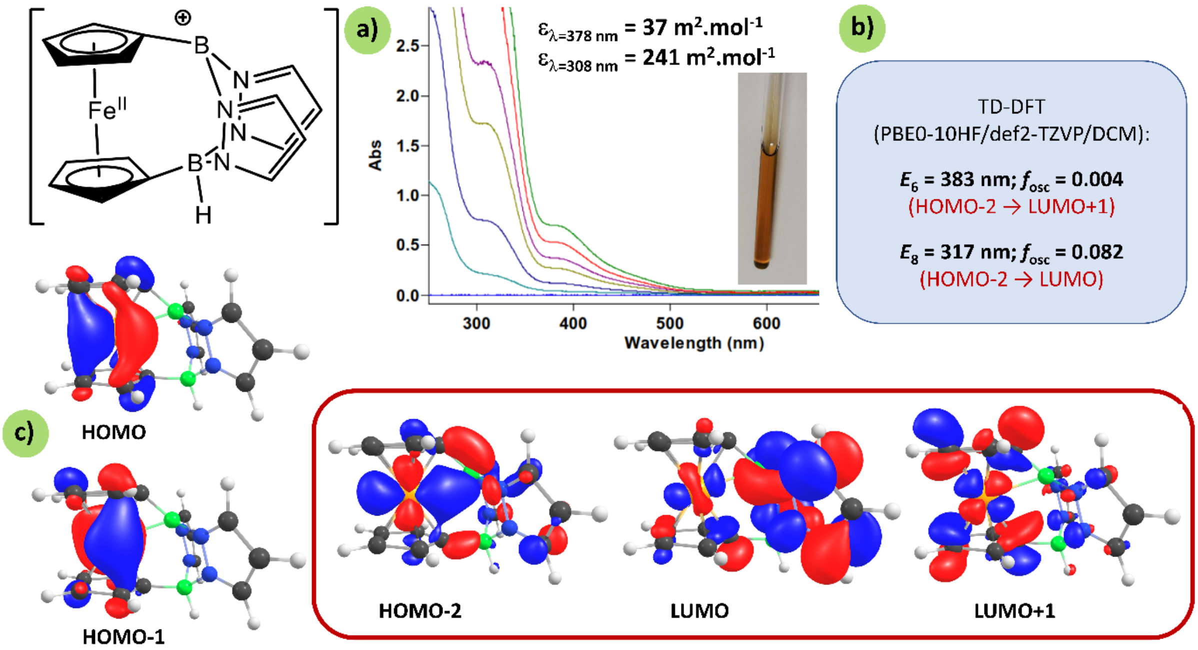

Figure S72. (a) Experimental UV-vis spectrum of **[2]**$^+$ in comparison with TD-DFT calculated parameters (b). (c) Relevant frontier MOs of **[2]**$^+$ participating in UV-vis absorption. See Table S12 for computed spectral parameters.

10. References (theory)

[S1] TURBOMOLE, version 7.5; TURBOMOLE GmBH, a development of the University of Karlsruhe and Forschungszentrum Karlsruhe, 2020; available from: http://www.turbomole.com.

[S2] Perdew, J. P.; Burke, K.; Ernzerhof, M., Generalized Gradient Approximation Made Simple. *Phys. Rev. Lett.* **1996**, *77*, 3865–3868.

[S3] Grimme, S.; Antony, J.; Ehrlich, S.; Krieg, H., A consistent and accurate ab initio parametrization of density functional dispersion correction (DFT-D) for the 94 elements H-Pu. *J. Chem. Phys.* **2010**, *132*, 154104.

[S4] Grimme, S.; Ehrlich, S.; Goerigk, L., Effect of the Damping Function in Dispersion Corrected Density Functional Theory. *J. Comput. Chem.* **2011**, *32*, 1456–1465.

[S5] Weigend, F.; Ahlrichs, R., Balanced basis sets of split valence, triple zeta valence and quadruple zeta valence quality for H to Rn: Design and assessment of accuracy. *Phys. Chem. Chem. Phys.* **2005**, *7*, 3297–3305.

[S6] Andrae, D.; U. Häußermann, U.; Dolg, M.; Stoll, H.; Preuß, H. Energy-adjusted *ab initio* pseudopotentials for the second and third row transition elements. *Theor. Chim. Acta* **1990**, *77*, 123–141.

[S7] Bergner, A.; Dolg, M.; Kuchle, W.; Stoll, H.; Preuss, H. Ab-initio Energy-Adjusted Pseudopotentials for Elements of Groups 13−17. *Mol. Phys.* **1993**, *80*, 1431−1441.

[S8] Wolff, S. K.; Ziegler, T., Calculation of DFT-GIAO NMR shifts with the inclusion of spin-orbit coupling. *J. Chem. Phys.* **1998**, *109*, 895–905.

[S9] Amsterdam Density Functional (ADF), version 2017.112, SCM, Theoretical Chemistry, Vrije Univeriteit, Amsterdam, Netherlands, 2018; available from: http://www.scm.com.

[S10] Adamo, C.; Barone, V., Toward Chemical Accuracy in the Computation of NMR Shieldings: the PBE0 Model. *Chem. Phys. Lett.* **1998**, *298*, 113–119.

[S11] Hansen, A. E.; Bouman, T. D., Localized orbital/local origin method for calculation and analysis of NMR shieldings. Applications to ^{13}C shielding tensors. *J. Chem. Phys.* **1985**, *82*, 5035–5047.

[S12] a) Autschbach, J., The role of the exchange-correlation response kernel and scaling corrections in relativistic density functional nuclear magnetic shielding calculations with the zeroth-order regular approximation. *Mol. Phys.* **2013**, *111*, 2544–2554; b) Greif, A. H.; Hrobarik, P.; Hrobarikova, V.; Arbuznikov, A. V.; Autschbach, J.; Kaupp, M., A relativistic quantum-chemical analysis of the trans influence on ^{1}H NMR hydride shifts in square-planar platinum(II) complexes. *Inorg. Chem.* **2015**, *54*, 7199–7208.

[S13] Klamt, A.; Schüürmann, G. COSMO: a new approach to dielectric screening in solvents with explicit expressions for the screening energy and its gradient. *J. Chem. Soc., Perkin Trans. 2* **1993**, 799–805.

[S14] Sivaev, I. B.; Bregadze, V. I., Lewis acidity of boron compounds. *Coord. Chem. Rev.* **2014**, 75, 75–88.

[S15] Neese, F. Prediction and interpretation of the ^{57}Fe isomer shift in Mössbauer spectra by density functional theory. *Inorg. Chim. Acta* **2002**, *337*, 181–192.

[S16] a) Sinnecker, S.; Rajendran, A.; Klamt, A.; Diedenhofen, M.; Neese, F., Calculation of solvent shifts on electronic g-tensors with the conductor-like screening model (COSMO) and its self-consistent generalization to real solvents (direct COSMO-RS). *J. Phys. Chem. A* **2006**, *110*, 2235–2245; b) Klamt, A.; Jonas, V.; Bürger, T.; Lohrenz, J. C., Refinement and parametrization of COSMO-RS. *J. Phys. Chem. A* **1998**, *102*, 5074–5085.

[S17] Reed, A. E.; Curtiss, L. A.; Weinhold, F. Intermolecular Interactions from a Natural Bond Orbital, Donor-Acceptor Viewpoint. *Chem. Rev.* **1988**, *88*, 899−926.

[S18] Mayer, I. Bond orders and valences from ab initio wave functions. *Int. J. Quantum. Chem.* **1986**, *29*, 477–483.

[S19] Glendening, E. D.; Badenhoop, J. K.; Reed, A. E.; Carpenter, J. E.; Bohmann, J. A.; Morales, C. M.; Landis, C. R.; Weinhold, F. NBO 6.0; Theoretical Chemistry Institute, University of Wisconsin: Madison, WI, 2013; available from: http://nbo6.chem.wisc.edu.

[S20] Gaussian 16, Revision C.01, Frisch, M. J.; Trucks, G. W.; Schlegel, H. B.; Scuseria, G. E.; Robb, M. A.; Cheeseman, J. R.; Scalmani, G.; Barone, V.; Petersson, G. A.; Nakatsuji, H.; Li, X.; Caricato, M.; Marenich, A. V.; Bloino, J.; Janesko, B. G.; Gomperts, R.; Mennucci, B.; Hratchian, H. P.; Ortiz, J. V.; Izmaylov, A. F.; Sonnenberg, J. L.; Williams-Young, D.; Ding, F.; Lipparini, F.; Egidi, F.; Goings, J.; Peng, B.; Petrone, A.; Henderson, T.; Ranasinghe, D.; Zakrzewski, V. G.; Gao, J.; Rega, N.; Zheng, G.; Liang, W.; Hada, M.; Ehara, M.; Toyota, K.; Fukuda, R.; Hasegawa, J.; Ishida, M.; Nakajima, T.; Honda, Y.; Kitao, O.; Nakai, H.; Vreven, T.; Throssell, K.; Montgomery, J. A., Jr.; Peralta, J. E.; Ogliaro, F.;

Bearpark, M. J.; Heyd, J. J.; Brothers, E. N.; Kudin, K. N.; Staroverov, V. N.; Keith, T. A.; Kobayashi, R.; Normand, J.; Raghavachari, K.; Rendell, A. P.; Burant, J. C.; Iyengar, S. S.; Tomasi, J.; Cossi, M.; Millam, J. M.; Klene, M.; Adamo, C.; Cammi, R.; Ochterski, J. W.; Martin, R. L.; Morokuma, K.; Farkas, O.; Foresman, J. B.; Fox, D. J. Gaussian, Inc., Wallingford CT, 2016.

[S21] Kohout, M. DGrid, version 5.2, Dresden, 2021; available from: http://www2.cpfs.mpg.de/~kohout/dgrid.html.

[S22] a) Becke, A. D.; Edgecombe, K. E. A simple measure of electron localization in atomic and molecular systems. *J. Chem. Phys.* **1990**, *92*, 5397–5403; b) Kohout, M.; Savin, A. Atomic shell structure and electron numbers. *Int. J. Quantum Chem.* **1996**, *60*, 875–882.

[S23] a) Bader, R. W. B. Atoms in Molecules: A Quantum Theory; Oxford University Press: Oxford, U.K., 1990. (b) Matta, C. F.; Boyd, R. J. The Quantum Theory of Atoms in Molecules; Wiley-VCH: Weinheim, Germany, 2007.

[S24] a) Lu, T. Multiwfn: A Multifunctional Wave Function Analyzer, version 3.8; Beijing Kein Research Center for Natural Sciences, 2021; available from: http://sobereva.com/multiwfn; b) Lu, T.; Chen, F. W. J., Multiwfn: A multifunctional wavefunction analyzer. *J. Comput. Chem.* **2012**, *33*, 580–592.

[S25] Smiles, D. E.; Wu, G.; Hrobárik, P.; Hayton, T. W. Use of ^{77}Se and ^{125}Te NMR Spectroscopy to Probe Covalency of the Actinide-Chalcogen Bonding in $[Th(E_n)\{N(SiMe_3)_2\}_3]^-$ (E = Se, Te; n = 1, 2) and Their Oxo-Uranium(VI) Congeners. *J. Am. Chem. Soc.* **2016**, 138, 814–825.

[S26] CYLview20; Legault, C. Y., Université de Sherbrooke, 2020; available from: http://www.cylview.org.

[S27] Chemcraft - graphical software for visualization of quantum chemistry computations; available from: https://www.chemcraftprog.com.

[S28] Paraview, version 5.2, Kitware Inc., Clifton Park, New York, USA, 2016; available from: http://www.paraview.org.

[S29] BriAnne Bentivegna, B.A.; Mariani, C. I.; Smith, J. R.; Ma, S.; Rheingold, A. L.; Brunker, T. J., Formation, Stability, and Structures of Borenium and Boronium Cations Derived from Pentamethylazaferrocene−Boranes by Hydride or Chloride Abstraction Reactions. *Organometallics* **2014**, *33*, 2820−2830.

[S30] Chen, J.; Roger A. Lalancette, R. A.; Jäkle, F., Synthesis and Lewis acid properties of a ferrocene-based planar-chiral borenium cation. *Chem. Commun.* **2013**, *49*, 4893−4895.

[S31] Braunschweig, H.; Fernandez, I.; Frenking, G.; Kupfer, T., Structural Evidence for Antiaromaticity in Free Boroles. *Angew. Chem. Int. Ed.* **2008**, *47*, 1951–1954.

[S32] Kaufmann, L.; Vitze, H.; Bolte, M.; Lerner, H.-W.; Wagner, M., 9-Ferrocenyl-9-borafluorenes: A Redox-Switchable Main Group Lewis Acid. *Organometallics* **2008**, *27*, 6215–6221.

[S33] Appel, A.; Jäkle, F.; Priermeier, T.; Schmid, R.; Wagner, M., Fe-B Bonding in (Dibromoboryl)ferrocene: A Structural and Theoretical Investigation. *Organometallics* **1996**, *15*, 1188–1194.

[S34] Carpenter, B. E.; Piers, W. E.; Parvez, M.; Yap, G. P. A.; Rettig, S. J., Synthesis, characterization and chemistry of bis-(pentafluorophenyl)boryl ferrocene. *Can. J. Chem.* **2001**, *79*, 857–867.

[S35] Prokofjevs, A.; Kampf, J. W.; Vedejs, E., A Boronium Ion with Exceptional Electrophilicity. *Angew. Chem. Int. Ed.* **2011**, *50*, 2098 –2101.

[S36] Del Grosso, A.; Pritchard, R. G.; Muryn, C. A.; Ingleson, M. J., Chelate Restrained Boron Cations for Intermolecular Electrophilic Arene Borylation. *Organometallics* **2010**, *29*, 241–249.

[S37] Kim, Y.; Gabbai, F. P. , Cationic Boranes for the Complexation of Fluoride Ions in Water below the 4 ppm Maximum Contaminant Level. *J. Am. Chem. Soc.* **2009**, *131*, 3363–3369.

[S38] Schnurr, A.; Bolte, M.; Lerner, H. W.; Wagner, M., Cyclic Phosphonium Bis(fluoroaryl)boranes – Trends in Lewis Acidities and Application in Diels–Alder Catalysis. *Eur. J. Inorg. Chem.* **2012**, 112–120.

[S39] De Vries, T. S.; Prokofjevs, A.; Vedejs, E., Cationic Tricoordinate Boron Intermediates: Borenium Chemistry from the Organic Perspective. *Chem. Rev.* **2012**, *112*, 4246–4282.

[S40] Lappert, M. F.; Litzow, M. R.; Pedley, J. B.; Tweedale, A., Bonding studies of compounds of boron and the Group IV elements. Part V. Boron-11 nuclear magnetic resonance data for the boron trihalides and mixed trihalides. *J. Chem. Soc. A* **1971**, 2426–2428.

[S41] Brown, H. C.; Racherla, U. S., Organoboranes. A convenient, highly efficient synthesis of triorganylboranes via a modified organometallic route. *J. Org. Chem.* **1986**, *51*, 427–432.

[S42] Rzepa, H. S.; Arkhipenko, S.; Wan, E.; Sabatini, M. T.; Karaluka, V.; Whiting, A.; Sheppard, T. D., An Accessible Method for DFT Calculation of ^{11}B NMR Shifts of Organoboron Compounds. *J. Org. Chem.* **2018**, *83*, 8020–8025.

[S43] Britovsek, G. J. P.; Ugolotti, J.; White, A. J. P. From $B(C_6F_5)_3$ to $B(OC_6F_5)_3$: Synthesis of $(C_6F_5)_2BOC_6F_5$ and $C_6F_5B(OC_6F_5)_2$ and Their Relative Lewis Acidity. *Organometallics* **2005**, *24*, 1685-1691.

[S44] Wrackmeyer, B. in Annual Reports on NMR Spectroscopy (G. A. Webb ed.), Academic Press, Vol. 20, 1988, pp. 61 – 203.

[S45] Chardon, A.; Osi, A.; Mahaut, D.; Doan, T. H.; Tumanov, N.; Wouters, J.; Fusaro, L.; Champagne, B.; Berionni, G., Controlled Generation of 9-Boratriptycene by Lewis Adduct Dissociation: Accessing a Non-Planar Triarylborane. *Angew. Chem. Int. Ed.* **2020**, *59*, 12402–12406.

[S46] Saida, A. B.; Chardon, A., Osi, A.; Tumanov, N.; Wouters, J.; Adjieufack, A. I.; Champagne, B.; Berionni, G., Pushing the Lewis Acidity Boundaries of Boron Compounds With Non-Planar Triarylboranes Derived from Triptycenes. *Angew. Chem. Int. Ed.* **2019**, *58*, 16889–16893.